Laser Frequency Stabilization for the Sub-SQL Interferometer

Von der Fakultät für Mathematik und Physik
der Gottfried Wilhelm Leibniz Universität Hannover
zur Erlangung des akademischen Grades

Doktor der Naturwissenschaften
Dr. rer. nat.

genehmigte Dissertation von

Dipl.-Phys.
Manuela Melanie Hanke

2018

Referent: Prof. Dr. Karsten Danzmann
Korreferentin: Prof. Dr. Michèle Heurs

Tag der Promotion: 05. Oktober 2018

Diese Arbeit wurde angefertigt am Max-Planck-Institut für
Gravitationsphysik (Albert-Einstein-Institut)
und
Institut für Gravitationsphysik,
Leibniz Universität Hannover,
Callinstraße 38, 30167 Hannover

Kurzfassung

Ein Jahrhundert nachdem die Existenz von Gravitationswellen von Albert Einstein in seiner allgemeinen Relativitätstheorie vorausgesagt wurde [Ein16], erfolgte der erste direkte Nachweis am 14. September 2015 [Abb16]. Kontinuierliche Weiterentwicklungen und Verbesserungen der Advanced LIGO (aLIGO) Gravitationswellenobservatorien haben deren Empfindlichkeit erhöht und diese Detektion ermöglicht.

In der finalen Konfiguration ist die Sensitivität der Detektoren durch Quantenrauschen begrenzt. Prototypen sind erforderlich, um weitere Entwicklungen zur Reduzierung des Rauschpegels unter das Quantenrauschen zu ermöglichen. Um das Standardquantenlimit (SQL) der Interferometrie zu erreichen und anschließend zu unterschreiten, ist der AEI 10 m Prototyp am Albert-Einstein-Institut (AEI) in Hannover entwickelt und aufgebaut worden.

Für das Sub-SQL-Interferometer ist eine extreme Frequenzstabilität der Laserquelle erforderlich. Zu diesem Zweck wurde ein 21 m langer, vollständig aufgehängter dreieckiger Ringresonator installiert. Dieser liefert eine stabile Längenreferenz, auf die die Laserfrequenz stabilisiert wird.

Um das Frequenzrauschen des freilaufenden Lasers zu reduzieren, wurde im Rahmen dieser Arbeit der Aufbau und die Inbetriebnahme dieses Frequenzreferenzresonators realisiert. Das ursprüngliche Design wurde verbessert, um diejenigen Geräuschquellen zu unterdrücken, die die Resonatorlänge beeinflussen. Um eine kontinuierliche Stabilisierung des Systems zu gewährleisten, wurde ein automatisches Strahllage-Kontrollsystem für das Eingangslicht in den Resonator entwickelt und implementiert.

Die Resonatoroptiken sind als Dreifachpendel zur Isolierung gegen seismisches Rauschen aufgehängt. Bei den Pendelresonanzfrequenzen von 0.5 Hz bis 10 Hz wird die Spiegelaufhängung über einen Regelkreis aktiv gesteuert. Dies wurde durch den Einsatz neuer digitaler Filter für eine Dämpfung in allen Freiheitsgraden verbessert. Die Spiegelbewegungen wurden bei der fundamentalen longitudinalen Resonanz auf $2 \times 10^{-2}\,\mu\mathrm{m}/\sqrt{\mathrm{Hz}}$ reduziert.

Eine weitere Unterdrückung der Resonatorspiegelbewegung wurde durch ein neues Konzept zur aktiven Resonatorlängenstabilisierung erreicht. Diese Technik verwendet das Rückkopplungssignal des Modenreiniger-Resonators, um die Länge des Frequenzreferenzresonators unterhalb von 2 Hz durch Einwirkung auf die longitudinale Bewegung des gekrümmten Resonatorspiegels zu steuern. Diese Verbesserung der Dämpfung reduzierte die Spiegelbewegung auf $2 \times 10^{-3}\,\mu\mathrm{m}/\sqrt{\mathrm{Hz}}$.

Die Dreifach-Pendel-Aufhängungen wurden in Betrieb genommen und die Stabilisierung der mechanischen Resonanzen war erfolgreich. Darüber hinaus wurde ein neues Konzept der niederfrequenten Resonatorlängenregelung implementiert. Für den Betrieb des Sub-SQL-Interferometers wurden die Grundlagen für die Leistungsfähigkeit der Laserfrequenzstabilisierung geschaffen.

Abstract

A century after the existence of gravitational waves was predicted by Albert Einstein in his general theory of relativity [Ein16], the first direct detection was made on September 14 in 2015 [Abb16]. Continuous upgrades and improvements of the Advanced LIGO (aLIGO) gravitational wave observatories have increased their sensitivity and made this detection possible.

In the final sensitivity configuration, the detectors are limited by quantum noise. Prototypes are required to carry out further developments to reduce the noise level below quantum noise. In order to reach and subsequently surpass the Standard Quantum Limit (SQL) of interferometry, the AEI 10 m Prototype facility was developed at the Albert Einstein Institute (AEI) in Hanover.

The achievement of extreme stability in frequency of the laser source for the sub-SQL interferometer is required. For this purpose, a 21 m long, fully suspended triangular ring cavity was established to provide a stable length reference on which the laser frequency is stabilized.

To reduce the frequency noise of the free-running laser, the scope of this thesis was the assembly and commissioning of the frequency reference cavity. The initial design has been improved to suppress the noise sources affecting the cavity length. To ensure continuous stabilization of the system, an automatic alignment of the input beam to the cavity was developed and implemented.

The cavity optics are suspended as triple pendulums for isolation from seismic noise. Around the pendulum resonance frequencies from 0.5 Hz to 10 Hz, the cavity optics are actively controlled by means of a feedback control loop. This has been improved by the use of new digital filters for a degree of freedom dependent damping and reduced the mirror motion at the fundamental longitudinal resonance frequency to $2 \times 10^{-2}\,\mu\mathrm{m}/\sqrt{\mathrm{Hz}}$. A further suppression of cavity mirror motion was achieved by implementing a new concept for active cavity length stabilization. This technique uses the mode cleaner feedback signal to control the length of the frequency reference cavity below 2 Hz by acting on the longitudinal motion of curved cavity mirrors. This damping improvement reduced the mirror motion to $2 \times 10^{-3}\,\mu\mathrm{m}/\sqrt{\mathrm{Hz}}$.

The triple suspensions are commissioned and the stabilization of the mechanical resonances is successful. In addition, a new concept of low-frequency cavity length control has been implemented. The foundations for achieving the performance of laser frequency stabilization have been established to enable the operation of the sub-SQL interferometer.

Key words: Ground-based Gravitational Wave Detectors, AEI 10 m Prototype, Laser Frequency Stabilization, Frequency Reference Cavity

Contents

List of Abbreviations

Notation	Description
ADC	Analog-to-Digital Converter
AEI	Albert-Einstein-Institute
aLIGO	Advanced Laser Interferometer Gravitational-Wave Observatory
AOM	Acousto-optic Modulator
ASD	Amplitude Spectral Density
BOSEM	Birmingham Optical Sensor and Electro-Magnetic Actuator
CDS	Control and Data System
DAC	Digital-to-Analog Converter
DOF	Degree of Freedom
DTT	Diagnostic Test Tool
DWS	Differential Wavefront Sensing
eLIGO	Enhanced Laser Interferometer Gravitational-Wave Observatory
EOM	Electro-optic Modulator
EPICS	Experimental Physics and Industrial Control System
FSR	Free Spectral Range
FWHM	Full Width at Half Maximum
GAS	Geometric Anti Spring
GUI	Graphical User Interface
GWINC	Gravitational Wave Interferometer Noise Calculator
HV	High Voltage
IP	Inverted Pendulum
ISS	Intensity Stabilization System

Notation	Description
JAMMT	Just Another Mode Matching Tool
LED	Light Emitting Diode
LVDT	Linear Variable Differential Transformer
LZH	Laser Zentrum Hannover
MEDM	Motif Editor and Display Manager
MIMO	Multiple-Input Multiple-Output
ND	Neutral Density
NPRO	Non-Planar Ring Oscillator
PBS	Polarizing Beam Splitter
PD	Photodiode
PDH	Pound-Drever-Hall
PEEK	Polyether Ether Ketone
QPD	Quadrant Photodiode
RCCM	Reference Cavity Curved Mirror
RCIM	Reference Cavity Input Mirror
RCOM	Reference Cavity Output Mirror
RF	Radio Frequency
RMS	Rout Mean Square
SAS	Seismic Attenuation System
SM	Steering Mirror
SPI	Suspension Platform Interferometer
SQL	Standard Quantum Limit
TEM	Transverse Electromagnetic Mode

Notation	Description
TTFSS	Table-Top Frequency Stabilization Servo
UHV	Ultra-High Vacuum
WFS	Wavefront Sensor

CHAPTER 1

Introduction

Routine detection of gravitational waves has been made possible with the recent development and commissioning of gravitational wave detectors. These detections have revolutionized modern astronomy by opening new path ways to understand the universe [Har10]. A first indirect detection of gravitational waves was made years ago by the observation of pulse arrival times of a binary pulsar [Tay82]. Years of research and continuous optimization of gravitational wave detectors have increased their sensitivity that led to the first direct detection in September 2015 [Abb16], [Aas15]. Future improvements of the detector sensitivity will increase the detection rate of astronomical events.

Before new technologies are implemented in gravitational wave observatories, they are developed and tested in smaller scale prototype facilities. Several groups all over the world work on prototype facilities. The German-British observatory GEO 600 close to Hanover in Germany was designed based on the experience and knowledge gained at the 10 m prototype in Glasgow [Rob95] and the 30 m prototype in Garching [Sho88]. The LIGO observatories operate a 40 m prototype at Caltech [War08] where new techniques are tested before being built into the main facilities. At the LIGO Advanced System Test Interferometer (LASTI) components and systems for Advanced LIGO (aLIGO) can be tested before installation in the detectors. This avoids long delays and down times of the detector and also allows experience and knowledge to be gained about the installation and commissioning process [Zuc02].

The AEI 10 m Prototype serves as a testbed for new techniques to improve the sensitivity of the next generation of gravitational wave observatories [Goß10]. A major objective is the observation of fundamental noise limits such as the Standard Quantum Limit (SQL) of interferometry. A sub-SQL Michelson interferometer is currently being commissioned in the AEI 10 m Prototype facility with the major goal to perform measurements at the SQL and find ways to surpass this fundamental noise limit. The required suppression of classical noise contributions is addressed by subsystems of the AEI 10 m Prototype such as the AEI Seismic Attenuation System (SAS) [Wan13], [Ber17], [Ber18], the Suspension-Platform-Interferometer (SPI) [Dah12], [Dah13], [Koe18] and suspension systems for cavity optics. Laser intensity noise is minimized by the implementation of an Intensity Stabilization System (ISS) [Jun16], [Jun17] and [Opp17].

For the operation of the sub-SQL interferometer a laser frequency noise suppression of the

free running laser of seven orders of magnitude from $10^{-4}\,\mathrm{Hz}/\sqrt{\mathrm{Hz}}$ at $20\,\mathrm{Hz}$ decreasing to below $10^{-6}\,\mathrm{Hz}/\sqrt{\mathrm{Hz}}$ at $1\,\mathrm{kHz}$ is required [Kaw10]. To achieve this, a triangular suspended cavity was assembled in the vacuum environment of the AEI 10 m Prototype across two seismically isolated optical benches. The cavity length forms a highly stable reference to which the laser frequency is stabilized. A Pound-Drever-Hall (PDH) sensing scheme [Bla01] in reflection of the cavity is implemented to lock the laser frequency to the length of the frequency reference cavity. To provide and maintain a stable cavity length reference, the mirror motion needs to be minimized. This is achieved by passive isolation of the mirrors using a triple pendulum suspension design and by using feedback control loops to actively damp the suspension motion. In this thesis the active damping control loops of the reference cavity were optimized by designing and implementing new damping filters and a new global longitudinal cavity control scheme. The noise performance of the frequency reference cavity could be optimized such that it provides a highly stable laser source in terms of frequency noise that is not limiting the performance of the sub-SQL interferometer at the AEI 10 m Prototype.

1.1 Thesis Outline

The frequency stabilization of the laser source for the sub-SQL interferometer at the AEI 10 m Prototype facility is the main focus of this thesis. An overview about the individual parts of this thesis is given in the following.

Chapter 2 starts with an introduction about the fundamental noise source in gravitational wave detectors and the AEI 10 m Prototype, quantum radiation pressure noise and quantum shot noise. The line of intersection of these two noise contributions is called the Standard Quantum Limit. An introduction to the AEI 10 m Prototype facility with its different subsystems which are designed to suppress classical noise contributions is provided in the same chapter.

The assembly and commissioning of the frequency reference cavity is focus of chapter 3. The requirements of frequency noise suppression are discussed and the optical layout of the cavity is presented. Schemes for cavity length stabilization along with the realization of an auto-alignment system for the cavity input beam is discussed in this chapter.

Chapter 4 introduces the various damping approaches tested at the frequency reference cavity suspensions. A new concept, global longitudinal cavity length control which showed promising results, is also presented in this chapter.

Possible improvements to the frequency reference cavity and the current results are summarized in chapter 5.

CHAPTER 2

Towards the Standard Quantum Limit

Quantum noise is a limiting noise source for ground-based interferometric gravitational wave detectors. It is formed at low frequencies by quantum radiation pressure noise and at higher frequencies by photon shot noise. Both effects are based on the quantum nature of light [Sau94], [Dan12].

Quantum photon shot noise is caused by light incident on a photo detector in quantized energy packages. As a statistical effect it follows a Poisson distribution. Quantum radiation pressure noise arises from the impact of photons on objects such as suspended mirrors, which leads to a momentum transfer. Shot noise is frequency independent on the photodiode, while the shot noise limited sensitivity is frequency dependent. Radiation pressure noise scales with $1/f^2$ at high frequencies.

Both contributions are dependent on the optical power in an interferometer. Equation 2.1 shows that increasing the light power P would result in lower shot noise. In this equation h_{sn} is the strain equivalent shot noise contribution to the interferometer's noise budget, f the Fourier frequency, L the length of the interferometer arms, $\hbar$ the reduced Planck constant, c the speed of light and λ the wavelength of the laser light [Sau94].

$$h_{sn}(f) = \frac{1}{L}\sqrt{\frac{\hbar c \lambda}{2\pi P}} \tag{2.1}$$

In contrast to quantum shot noise, the radiation pressure noise is enhanced with increasing power as shown in equation 2.2 [Sau94]. The equation also shows the dependence on the mirror mass m of the interferometer which sets requirements on mirror dimensions.

$$h_{rp}(f) = \frac{1}{mf^2 L}\sqrt{\frac{\hbar P}{2\pi^3 c \lambda}} \tag{2.2}$$

The crossover of quantum photon shot noise and quantum radiation pressure noise changes depending on the optical power in an interferometer, but does not exceed a line with a gradient of $1/f$. This line is the SQL displayed by the black line in figure 2.2.

2.1 The AEI 10 m Prototype

The knowledge and experience required for the development and improvement of gravitational wave observatories is often gained in smaller scale facilities. These prototype facilities are more accessible to perform new experiments and are suited for testing different techniques before they are built into gravitational wave detectors. Compared to km-scale observatories they have the advantage that their vacuum systems can be pumped and vented on shorter time scales.

The AEI 10 m Prototype facility is currently being commissioned at the AEI in Hanover. It is planned to be a testbed to develop new techniques and gain knowledge and experience for future gravitational wave detectors [Goß10]. Its primary goal is to perform measurements at the SQL and surpass it at a frequency of 200 Hz.

The main experiment of the AEI 10 m Prototype is a Michelson interferometer with Fabry-Perot arm cavities placed in a vacuum envelope. The arm length of the interferometer is planned to be 11.65 m. The vacuum system is designed for rapid venting and pump down; it therefore allows easy access to the experiment.

The goal of reaching and surpassing the SQL sets high requirements for prototype facilities. The AEI 10 m Prototype consists of several subsystems, all aiming for a suppression of classical noise contributions. Three seismically isolated optical benches are installed inside the vacuum system to provide a low seismic noise environment. An image of the vacuum system with the optical tables installed inside the tanks is shown in figure 2.1. All in-vacuum experiments are placed on these benches. The main interferometer optics are suspended as triple pendulums. Ancillary interferometers like the suspension platform interferometer (SPI) are used to control the inter table motion such that the three tables behave as a single rigid platform at low frequencies. The light source is a pre-stabilized 35 W laser which was developed in a cooperation between the AEI and the Laser Zentrum Hanover (LZH) as used in Enhanced LIGO (eLIGO).

Quantum noise contributions set a limit to the noise level that can be tolerated from technical noise sources. The requirements for the AEI 10 m Prototype Interferometer are defined by the SQL. Measuring the SQL at 200 Hz is a requirement to fulfill the AEI 10 m Prototype's aim of becoming a test facility for techniques to perform measurements below the SQL.

Figure 2.2 shows a simulated noise budget of the AEI 10 m Prototype, calculated with the Gravitational Wave Interferometer Noise Calculator (GWINC). This plot assumes an input laser power of 5 W and includes the experimental subsystems required to minimize different noise contributions that would disturb the interferometer sensitivity. Quantum noise is illustrated by the magenta line in this figure. In the frequency region around 200 Hz all classical noise sources need to be sufficiently suppressed in order to reach and surpass the SQL, depicted by the black line. The interferometer is limited by quantum

noise in a frequency range from 30 Hz to 1 kHz. Other noise contributions like seismic noise (green line), Brownian thermal noise of substrates (orange line) and coatings (brown line), coating thermo-optic noise (light blue line) and laser frequency noise (red line) are below the quantum noise line including a safety margin in the frequency range of interest. The suppression of frequency noise and the stabilization of the laser is the main focus of this thesis.

The sub-SQL interferometer, the AEI 10 m Prototype facility and the required subsystems are described in the next sections.

2.1.1 Sub-SQL Interferometer

As already mentioned, the main objective of the AEI 10 m Prototype is to perform measurements at and below the SQL in a frequency range around 200 Hz with macroscopic optics. To be able to detect radiation pressure noise light-weight 100 g mirrors are used in the interferometer.

The sub-SQL interferometer is located in an L-shaped vacuum system. Figure 2.3 shows a preliminary layout of the sub-SQL interferometer. The laser light is coupled to the central optical bench in the vacuum system via a photonic crystal fibre. After passing through a mode cleaner cavity, the light is transmitted to the south optical bench where it hits a curved collimator mirror and is reflected back to the central optical table. Two steering mirrors suspended as single pendulums guarantee alignment into the interferometer. The

Figure 2.1: Rendered image of the vacuum system of the AEI 10 m Prototype. The vacuum system is L-shaped and consists of three vacuum tanks. They are connected via vacuum tubes and separated by 10 m. Three seismically isolated optical tables are placed inside the tanks. Picture courtesy of G. Bergmann
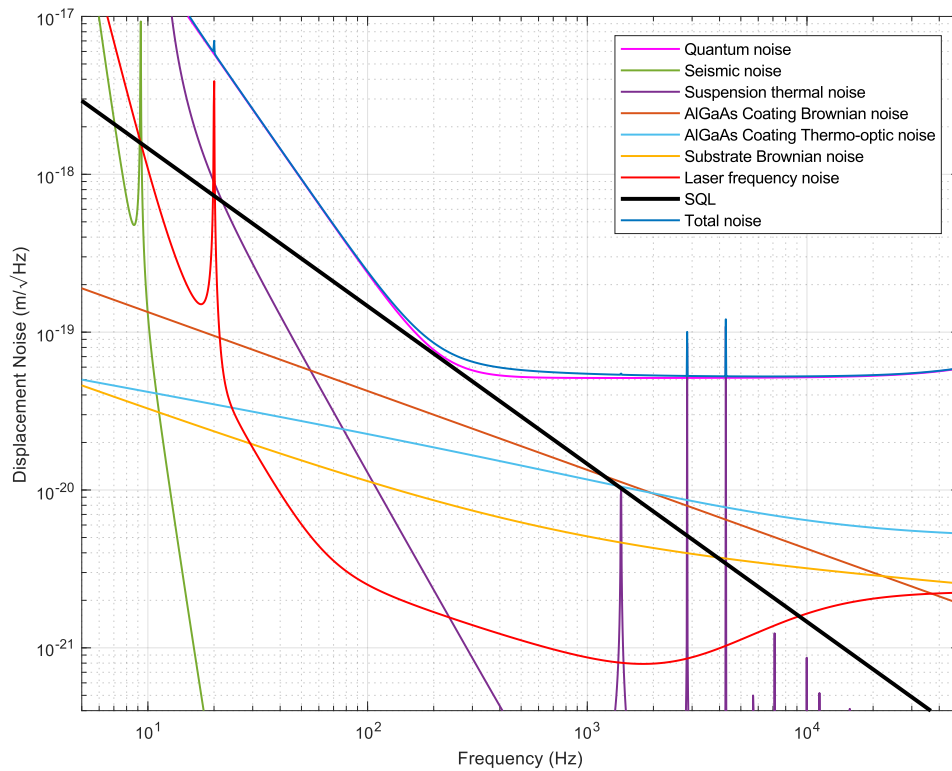
Figure 2.2: Simulated noise budget for the AEI 10 m Prototype Interferometer made by D. Wu with the Gravitational Wave Interferometer Noise Calculator (GWINC). The assumed input power is 5 W. The classical noise sources such as seismic noise (green), coating Brownian noise (brown) and substrate Brownian noise (orange), coating thermo-optic noise (light blue) and laser frequency noise (red) are suppressed in order to lie below the quantum noise (magenta), consisting of quantum radiation pressure noise at lower frequencies and photon shot noise at higher frequencies. The SQL is delineated by the black line. In a frequency range from 30 Hz to 1 kHz all classical noise contributions are well suppressed and the interferometer will be limited by quantum noise.

beam splitter, located in the center of the central table, as well as the cavity mirrors are suspended in triple pendulum stages, as described in 2.3.3. The input test masses of the arm cavities are located on the central optical table while the end mirrors are located each on the south and west optical bench.

As preparation for the sub-SQL interferometer, one arm cavity was set up and commissioned first which will be introduced in the following.

Single-Arm-Test

The Single-Arm-Test (SAT) is an impedance matched cavity set up in one arm of the interferometer. Since the high quality main optics for the sub-SQL interferometer have long lead times for polishing and delivery, they are replaced by pilot optics for the SAT. In order to minimize coating thermal noise, large spot sizes are required on the cavity mirrors. These large laser beams lead to arm cavities that are close to instability. For a linear cavity, a configuration with relatively large laser beams on the cavity mirrors can be achieved either by selecting a concentric resonator design or a planar cavity design with two plane-parallel mirrors. Both resonator configurations are close to being unstable; see [Kog66] for more details. The SAT uses curved mirrors, starting with a distance of 10.8 m between the mirrors corresponding to a stable cavity configuration. In this configuration, the beam spot sizes on the mirrors are relatively small and susceptible to coating thermal noise. By shifting the end mirror the cavity length can be increased and the beam size on the coatings gets larger. With this approach the coating thermal noise gets improved while the cavity is moved stepwise closer to a concentric configuration and closer to instability. The final cavity length is planned to be 11.395 m, resulting in a cavity g-factor of 0.995 an a spot size of 9.7 mm [Grä13]. In comparison, the arm cavity g-factor of aLIGO is 0.832 [Wan18], [Muz12].

In addition, the SAT set-up allows testing of a new Electro-Static Drive (ESD), which is needed for the length stabilization of the interferometer arms [Koe18], [Wit15].

Another advantage of this approach is that during the installation and commissioning of the SAT only two seismic isolation tables were available in the vacuum system while the third table was still under construction.

The preliminary optics used for the SAT are fused silica substrates with amorphous Silica/ Tantala coatings. The main optics in the final version of the interferometer will be fused silica substrates with AlGaAs:GaAs coatings.

More information about the proposed design of the SAT can be found in [Grä13]. The implementation and measurement results are discussed in [Koe18].

2.1.2 Vacuum System

To avoid acoustic coupling into sensitive experiments as well as refractive index fluctuations the sub-SQL interferometer is placed in a vacuum environment. In addition a clean surrounding is required to avoid dust particles on the optics. In operation high laser power
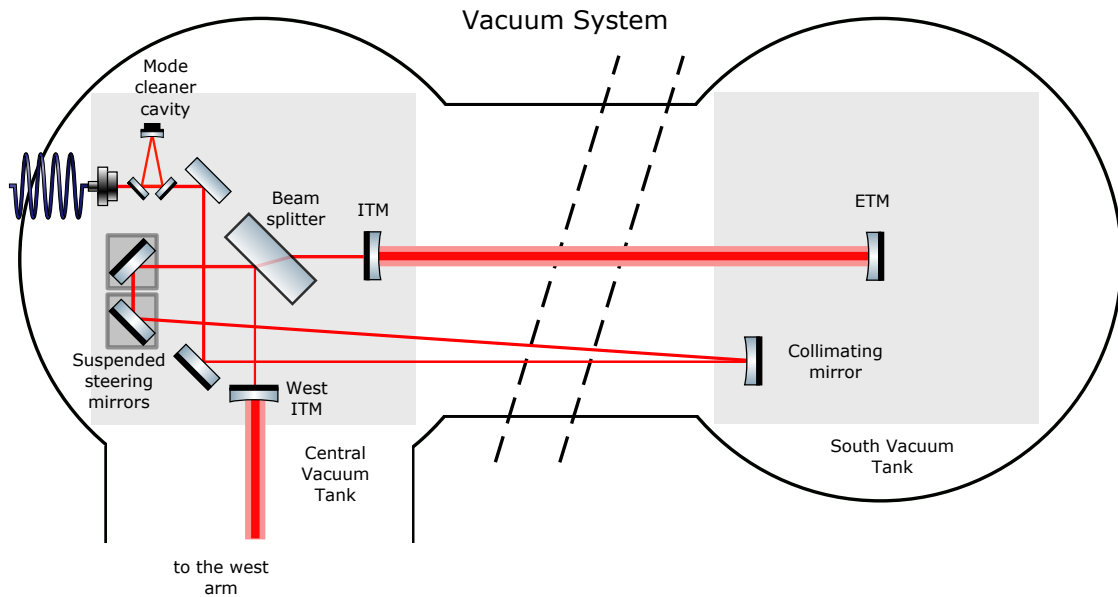
Figure 2.3: Initial planned optical layout of the sub-SQL interferometer. The laser beam is coupled into the central tank of the vacuum system via a photonic crystal fiber. After passing the mode cleaner the light is sent to the south table to a curved collimating mirror and reflected back to the central optical table. Two suspended steering mirrors ensure the alignment of the beam to the suspended beam splitter and into the interferometer. The arm cavities of the Michelson interferometer are formed by the input test mass (ITM) on the central optical table and the end test mass (ETM) on the south optical bench respectively on the west optical table (not shown here). The cavity mirrors and the beam splitter are suspended as triple pendulums.

will be built up in the cavities and dust could be burned onto the optics which would reduce their surface quality and decrease the interferometer sensitivity. Also scattering of the laser light by particles would negatively influence all measurements.

The vacuum system is L-shaped and contains a volume of ca. $100 \, \mathrm{m}^3$. Three tanks are connected via 1.5 m diameter tubes, separated by 11.65 m from center to center. The design of the vacuum system was optimized for easy access to allow commissioning and alignment work inside the system. Every tank is equipped with a 1 m sized door. With a height of 3.4 m and a diameter of 3 m, they allow in-vacuum work.

Several pumps in the system allow for a rapid pump down and low pressure maintenance. After closing the vacuum system a rough pump down is realized with a screw pump. Further evacuation is done by two turbo-molecular pumps. Within 12 h of operation a pressure of $10^{-6} \, \mathrm{ha \, Pa}$ can be reached. After one week of pumping the pressure can be reduced to $10^{-7} \, \mathrm{ha \, Pa}$ [Goß10].

The design of the vacuum system and the rather short time scales for evacuating allow fast

changes between commissioning work inside the system and experimental operation.

2.1.3 Digital Control and Data System

The signals from different experiments and subsystems are processed with a real-time control system. All core experiments and subsystems of the AEI 10 m Prototype are controlled via this Control and Data System (CDS). It was developed at the California Institute of Technology for the LIGO detectors and adapted for the AEI 10 m Prototype facility. Experiment data can be digitized, processed and stored for later evaluation. The important advantage is the real time capability of CDS data.

Numerous channels from experiment sensors and actuators can be used in multiple-input multiple-output control loops. Signals from the subsystems are sent to analog-to-digital converters (ADCs). The digitized signals are processed with the front end computers. Five different front ends are used for the AEI 10 m Prototype. Digital-to-analog converters (DACs) are used to transform the data into analog signals going to the actuators of the experiments.

Experiment control screens can be designed and implemented by a Motif Editor and Display Manager (MEDM). It is used as a Graphical User Interface (GUI) and allows remote control of experiment parts such as actuators at the tables or suspensions. MEDM is an extension of the Experimental Physics and Industrial Control System (EPICS) which allows access to the CDS channels from the experiments.

Figure 2.4: Vacuum system for the AEI 10 m Prototype Interferometer consisting of three tanks connected via steel tubes. The system encloses a volume of $100 \, \text{m}^3$. Each tank has a diameter of 3 m and a height of 3.4 m and hence allows in-vacuum installation and commissioning work. Inside each vacuum tank three seismic isolated tables are placed to isolate the components such as optics from ground motion. The table centers are separated by 11.65 m. Several pumps allow a fast pump down of the system. A pressure of $10^{-6} \, \text{ha Pa}$ can be reached within some hours while further pumping leads to a pressure of $10^{-7} \, \text{ha Pa}$ after one week. Picture courtesy of P. Oppermann.

2.2 Coordinate system

For the description and operation of a complex experiment like the AEI 10 m Prototype, a well-defined coordinate system is required. The naming convention used throughout this thesis is shown in figure 2.5. On the left side the global coordinate system is shown for the vacuum system of the AEI 10 m Prototype. The origin is set to the central vacuum tank. Naming of the other two vacuum tanks is based on the cardinal directions. The translational degrees of freedom are x,y and z. In the drawing plane, x points from the central tank towards the west tank and y from the central tank towards the south tank. The direction perpendicular to the drawing plane pointing upwards is z. Rotational degrees of freedom are r_x, r_y and r_z.

For the description of individual mass motion the different degrees of freedom are called longitudinal, vertical and transversal for translational degrees of freedom and pitch, yaw and roll as rotational degrees of freedom. They are shown in the picture on the right for an example of a suspended mirror.
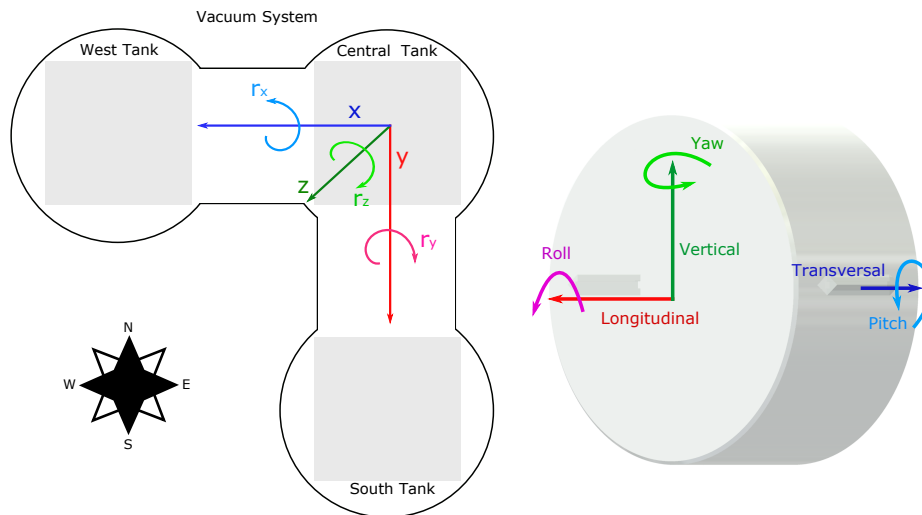
Figure 2.5: Naming convention for the different degrees of freedom for the AEI 10 m Prototype (left side) and for a suspended mirror (right side). The origin for the global coordinate system of the AEI 10 m Prototype is defined to be in the central vacuum tank shown at the upper right side. The translational degrees of freedom towards the west and the south vacuum tanks are called x and y. The translational degree of freedom pointing upwards perpendicular to the drawing plane is z. Rotational degrees of freedom are depicted as r_x, r_y and r_z. The degrees of freedom of an individual mass like a suspended mirror is shown on the right side. The translational degrees of freedom are longitudinal, vertical and transversal, rotational degrees of freedom are pitch, yaw and roll.

2.3 Seismic Isolation

Ground motion originates from natural or anthropogenic sources and is the dominant disturbance for ground-based experiments in a frequency range from 0.1 Hz to 100 Hz. Since the laboratory of the AEI is located in Hanover surrounded by traffic and tram ways anthropogenic noise is a major contribution to seismic noise. Disturbances introduced by ground motion would couple into the interferometer resulting in measurements with limited sensitivity.

Isolation against ground motion is provided at the AEI 10 m Prototype by seismically isolated optical tables and by interferometric stabilization of the benches. Furthermore, key optics are suspended as multiple pendulums. These subsystems are presented in the following sections.

2.3.1 Seismic Attenuation System

A passive mechanical isolation system was implemented at the AEI 10 m Prototype which provides a first stage of isolation from ground motion starting from 0.2 Hz [Wan12]. Three square-shaped 1.75 m x 1.75 m seismically isolated optical benches are placed in the three vacuum tanks of the AEI Prototype facility. All in-vacuum experiments including main optics and ancillary components are placed on these platforms.

A photograph of the Seismic Attenuation System (SAS) installed in the vacuum system of the AEI 10 m Prototype is shown in figure 2.6. The table design is based on the LIGO Seismic Attenuation System developed by the California Institute of Technology for aLIGO [Sto09].

For weight optimization and providing stiffness at the same time the table is made of stainless steel supported by an internal honey comb structure at the table top. Each table weighs 950 kg and is equipped with ballast rods with a total weight of 220 kg. These rods allow balanced weight distribution and can be replaced with payload on the tables such as optics and mounts, suspension structures and other components.

The table rests on three Geometric Anti-Spring (GAS) filters consisting of flat blade springs which are bent and radially compressed. This radial stress on the blades induces an anti-spring effect which results in a low vertical effective stiffness. On their tips the blades are connected via a keystone. They can be tuned by changing their compression and by applying positive feedback for lower resonance frequencies. The vertical resonance frequency could be pushed down to 0.3 Hz. Picture 2.7 shows a photograph of a GAS filter. The GAS filters are placed in between two stiff plates forming the spring box. This is supported by three Inverted Pendulum (IP) legs for horizontal isolation. They are equipped with a flexure at the bottom to prevent them from tipping over and a flexure at the top that connects the IP legs and the spring box. The IP legs provide a horizontal resonance frequency of 0.1 Hz.

To actively damp the table resonance frequencies, additional co-located sensors and

actuators are implemented in the system.

The sensors installed in the AEI-SAS cover different frequency ranges. Linear Variable Differential Transformers (LVDTs) measure the table position in horizontal and vertical degrees of freedom relative to the ground. They are sensitive in a frequency range from DC to above 100 Hz with a dynamic range of tens of millimeters and a nanometer scale resolution [Wan12].

Three accelerometers measure the inertial movement of the spring box in horizontal degrees of freedom. Their measurement frequency band ranges from 0.3 Hz to 50 Hz. Vertical motion of the optical table is monitored by three geophones. The active control of the tables is limited to a few Hertz bandwidth.

More information about the seismic isolation system can be found in [Wan13], [Ber17] and [Ber18].

2.3.2 Suspension Platform Interferometer

A first stage of seismic isolation is provided by the AEI-SAS as described in the previous section. In the low frequency range below the passive isolation of the optical tables additional active control is required. An interferometric interconnection between the three optical tables in the vacuum system of the AEI 10 m Prototype is realized with
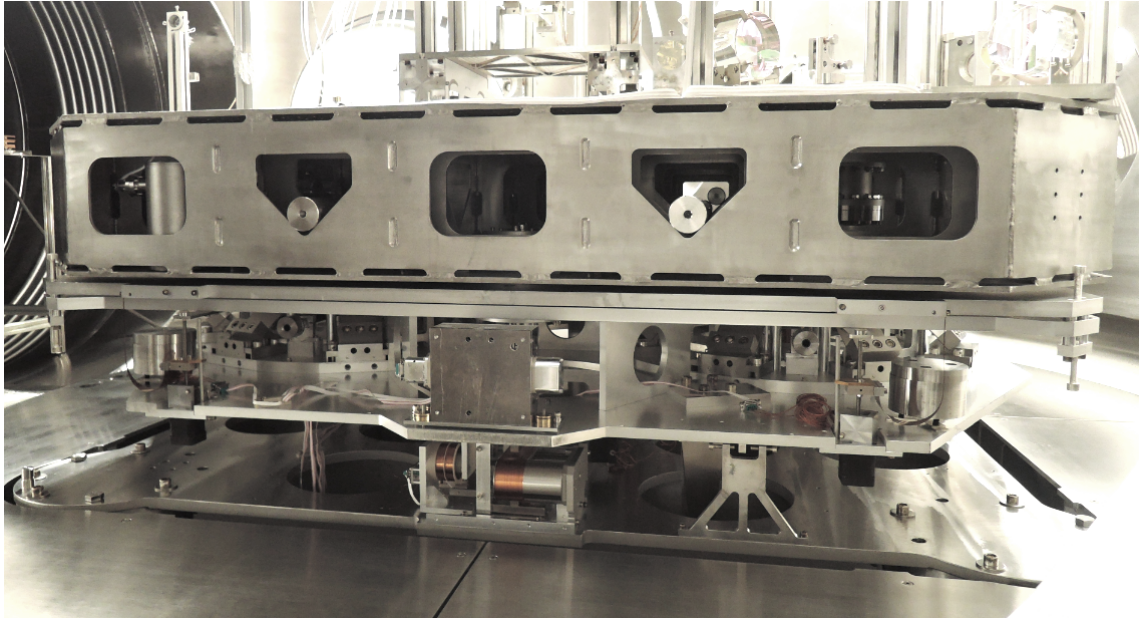
Figure 2.6: Photograph of the central AEI-SAS inside the vacuum system of the AEI 10 m Prototype facility. The optical bench is supported by three inverted pendulum legs providing horizontal isolation, not visible in the photograph. Vertical isolation is provided by three Geometric Anti-Springs on each table.
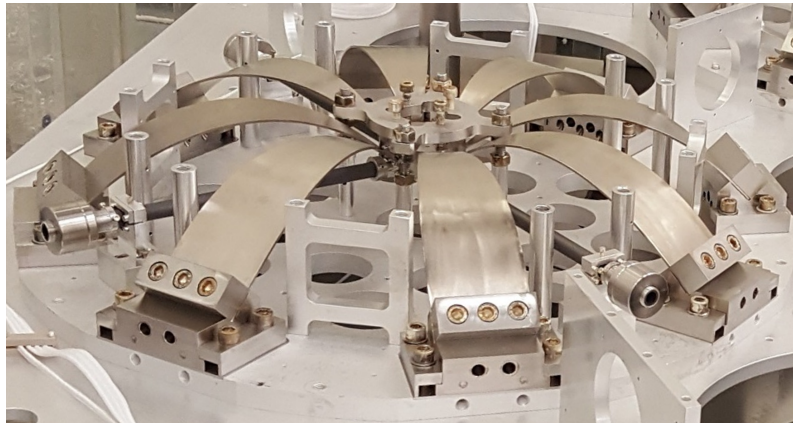
Figure 2.7: Photograph of a GAS filter for the AEI-SAS. It consists of maraging steel spring blades that are bent and connected at their tips by the key stone. Picture courtesy of G. Bergmann.

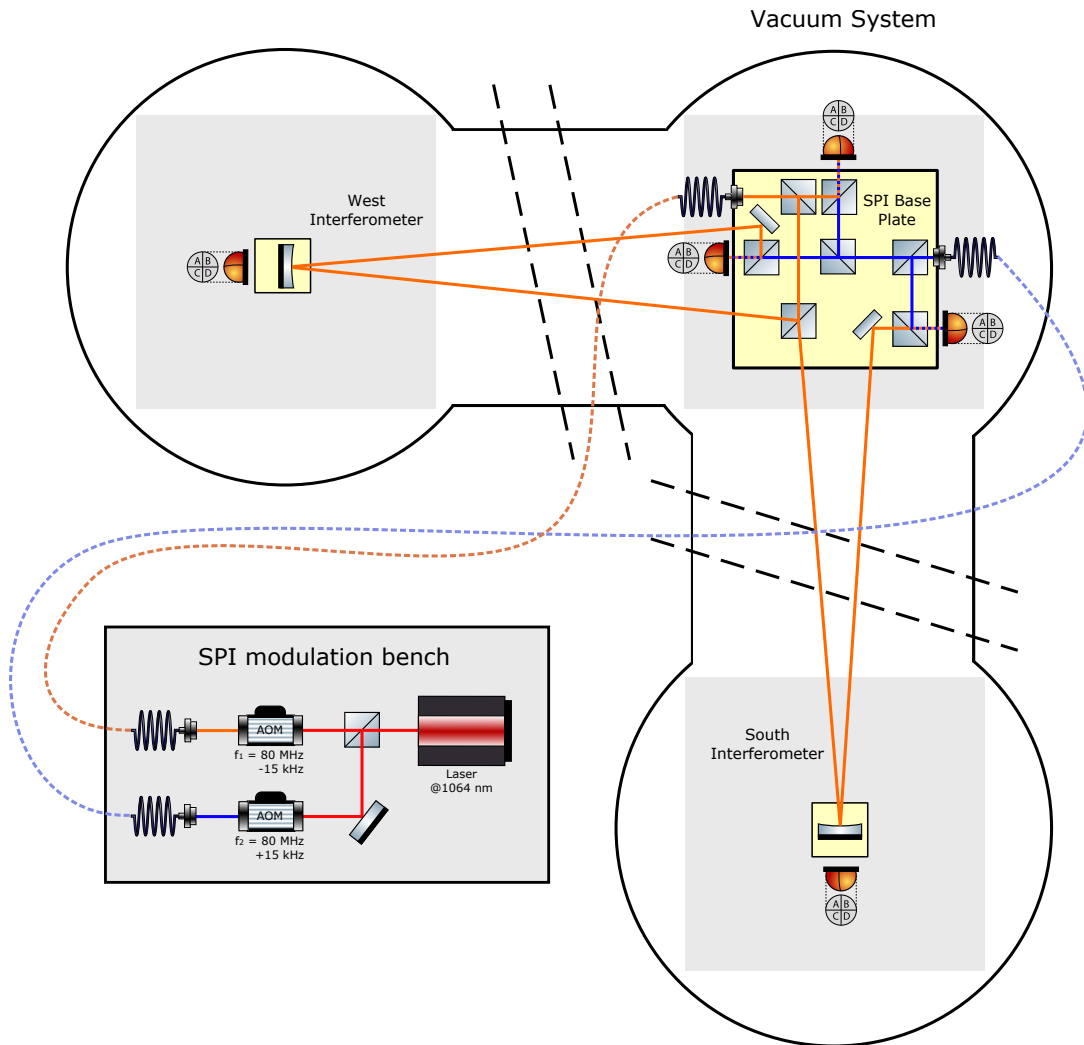the Suspension Platform Interferometer (SPI). It measures the differential motion of the two satellite optical tables to the central optical table and actively damps this motion via feedback control. The goal for longitudinal displacement stability between the tables is $100 \, \text{pm}/\sqrt{\text{Hz}}$ between 10 mHz and 100 Hz while the aim for relative angular noise in the same frequency range is $10 \, \text{nrad}/\sqrt{\text{Hz}}$ [Dah12].

The interferometric readout is realized by four Mach-Zehnder interferometers. A simplified sketch of the SPI layout is shown in figure 2.8. An iodine-stabilized Nd:YAG laser with a wavelength of 1064 nm was chosen as a laser source in order to provide the desired laser frequency noise requirement of $120 \, \text{Hz}/\sqrt{\text{Hz}}$ at 10 mHz [Dah12]. The laser is placed outside the vacuum system on the modulation bench, shown in the lower right of the picture. The beam is split into two paths on the modulation bench, each of them frequency shifted by passing an Acousto-Optic Modulator (AOM). The frequency difference of the two resulting beams is 15 kHz. The light is coupled into the vacuum system via optical fibers. The output couplers are placed on the central table inside vacuum on the measurement bench of the SPI. This is a quasi-monolithic base plate made of Clearceram ®-Z HS which provides sufficient stability in terms of thermal and mechanical drifts. The optical components are hydroxy-catalysis bonded to the base plate [Ell05].

On the SPI base plate the light is divided into the different interferometers. One interferometer connects the central and south optical table measuring relative displacement and angular deviations between these two. One arm of the interferometer is going from the central table to the south table while the other arm stays on the SPI base plate. Likewise the west interferometer senses displacement between the central and west table.

More information about the design and assembly of the SPI can be found in [Dah12] and [Dah13]. The commissioning and improvement of the SPI are described in [Koe18].

Figure 2.8: Simplified schematic of the Suspension Platform Interferometer (SPI) at the AEI 10 m Prototype. It consists of four Mach-Zehnder interferometers, namely the reference interferometer, the diagnostic interferometer and the two measurement interferometers (south and west interferometer). The laser light is prepared on a modulation bench outside of the vacuum system and fiber-coupled into the vacuum system. The distribution into the four interferometer is done on the SPI base plate inside the vacuum system. The two measurement interferometers sense relative motion between two reference points on the central table and on one of the end tables. The picture was made based on [Koe18].

Optical Lever

Between the central and south table, optical levers are installed to measure pitch and yaw motion of the optical tables relative to each other. The light for the optical lever is split off on the SPI base plate in vacuum. The beam from the central table is sent through a telescope consisting of two lenses to get a beam size on the far table in approximately 10 m distance of about 2 mm. A quadrant photodiode on the south table is used to detect the beam position. The signals from any beam displacement can be fed back to table actuators to control the position of the optical tables.

In the same way another optical lever is set up from the south table going to the central table. The light for this optical lever is fiber-coupled into the south tank. On the table it also passes two lenses to adjust the beam size and divergence angle. Another quadrant photodiode on the central table detects the light coming from the south table.

During writing of this thesis, the optical levers between central and south table were installed; see [Koe18] for more details. There is a second optical lever currently also going to the south table and used as an out-of-loop sensor to test the performance.

2.3.3 Suspensions

Due to the stringent requirements in terms of seismic isolation described in the earlier sections, all main optics at the AEI 10 m Prototype are suspended in multi-cascaded pendulum stages to get additional isolation to the AEI-SAS. Each pendulum stage provides an isolation of $1/f^2$ from seismic motion above its resonance frequency. Triple suspensions benefit from a $1/f^6$ slope of isolation in an ideal system.

Cavity mirrors, such as the optics of the sub-SQL interferometer and the frequency reference cavity, are required to be very quiet. Any length change of the cavity due to mirror motion disturbs its sensitivity. These length changes are imprinted onto the laser light as unwanted frequency modulation.

The cavity mirrors of the sub-SQL interferometer and the frequency reference cavity are suspended as triple pendulums. Due to their different applications, they are designed for different mirror dimensions. While the sub-SQL interferometer optics weigh 100 g to be able to detect radiation pressure noise, the frequency reference cavity mirrors are designed for 850 g optics to suppress radiation pressure effects.

All suspensions can be remotely controlled by the CDS of the AEI 10 m Prototype and are equipped with several sensors and actuators.

A short overview about the two different triple suspension designs and the single suspended steering mirror suspensions implemented in the AEI 10 m Prototype is given in this section.

Triple Suspensions for the Sub-SQL Interferometer

Since an important property of the sub-SQL interferometer is to measure quantum radiation pressure noise, light optics are required. The cavity mirror mass was chosen to be 100 g in

order to satisfy these requirements while keeping the size practical to handle at the same time. In contrast to this, gravitational wave detectors use heavier mirrors in order to not be affected by radiation pressure noise, aLIGO for example uses 40 kg core optics [Aas15]. The triple pendulum suspensions for the sub-SQL interferometer were developed at the University of Glasgow. Figure 2.9 shows a photograph of a sub-SQL interferometer suspension. It has three horizontal and two vertical isolation stages. The cross-shaped top mass is suspended via 100 μm thick steel wires from the two top blades that are attached to the suspension frame. The top mass and the penultimate mass are equipped with magnet-coil actuators for position control in different degrees of freedom. In addition passive eddy-current damping is realized by coils with co-located copper cups at both masses.

The penultimate mass is made of aluminum and has the same outer dimensions as the lowest stage. Actuation on the mirror can be achieved with an electrostatic drive in a plate capacitor configuration [Wit15].

The final configuration of the suspensions is planned to be monolithic in the last stage. Fused silica fibers with a thickness of 20 μm will be welded to fused silica ears bonded to the mirror and the penultimate mass [Grä13]. For the initial tests, non-monolithic suspensions with steel wires were chosen.

Triple Suspensions for the Frequency Reference Cavity

In contrast to the sub-SQL interferometer suspensions, the frequency reference cavity suspensions are designed for 850 g mirrors. This mass was chosen in order to avoid susceptibility to radiation pressure noise.

Similar to the sub-SQL interferometer suspensions the frequency reference cavity suspensions consist of three horizontal isolation stages provided by the pendulums and two vertical stages formed by blade springs. The top mass of the suspension chain is suspended via 150 μm thick steel wires from two blade springs that are attached to the frame structure. The intermediate mass is made of aluminum and has the same dimensions as the mirror. It is suspended with 100 μm thick steel wires from a set of blades inside the top mass. Two clamps at the intermediate mass hold the wire slings for the lowest mass, the mirror. These wires have a thickness of approximately 50 μm. The design of the suspensions are described in detail in [Wes16].

The suspension chain can be remotely controlled via the CDS. Therefore, the suspension frame is equipped with six sensors and actuators to control the position of the top mass in all degrees of freedom. Sensing and actuation of the suspensions is done at the top mass to avoid electronic noise coupling to mirror motion. The frequency reference cavity suspensions as well as their damping techniques will be described in more detail in chapter 3.3.1.
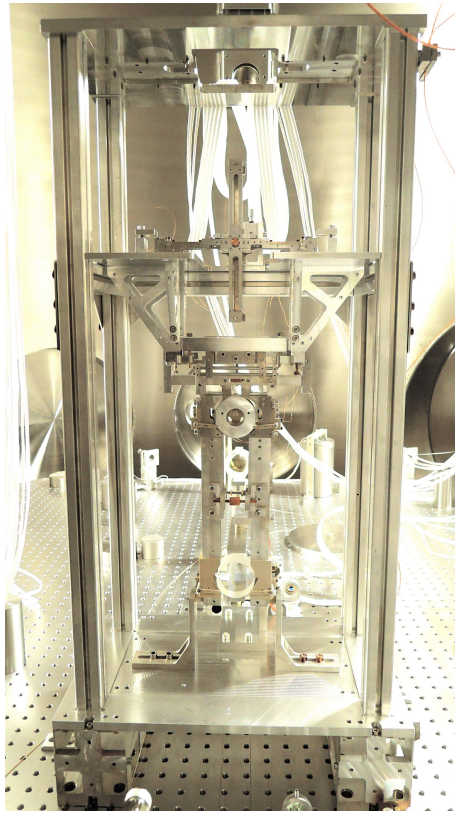
Figure 2.9: Photograph of the triple pendulum suspensions for the sub-SQL interferometer with 100 g optics. The top mass is suspended from vertical spring blades via 100 μm thick steel wires. The next stage, the penultimate mass, is supported by 50 μm thick steel wires. Fiber guards protect the suspension and give a possibility to clamp it for installation and commissioning work. In the final configuration the wires and aluminum masses will be exchanged by monolithic suspensions.

Steering Mirror Suspensions

A set of two steering mirrors is located in front of the frequency reference cavity to allow alignment of the input path to the cavity. They are suspended as single-stage pendulums. Two inch mirrors are placed in an aluminum holder and suspended with steel wires from the suspension frame. These wires have a thickness of 100 μm and are more robust than the wires of the lowest stage of the reference cavity suspensions.

The steering mirrors can be actuated remotely via CDS. Magnets are glued on the holding structure of the mirrors and allow, in addition with co-located coils, a control of the mirror position and the angular alignment. Two more pairs of magnets with coils are located at the side of the mirror frame. They are implemented for additional eddy current damping in the transversal degree of freedom.

A set of two steering mirrors is located in front of the sub-SQL interferometer. They

have a diameter of four inch. Besides the bigger dimensions of mirrors and frames these
suspensions are equivalent to the steering mirror suspensions in front of the frequency
reference cavity.

2.4 Laser Stabilization

For the planned experiments at the AEI 10 m Prototype facility a highly stable laser source
is required. Stringent requirements are placed on the intensity and frequency noise of the
laser in order to prevent degradation of sensitivity of the interferometer. Along with this,
an additional requirement is placed on the spatial mode of the input laser beam i.e. all the
input light is required to be in the fundamental transverse electromagnetic mode TEM_{00}.
Frequency noise is equivalent to length changes in the interferometer arms and disturbs the
noise performance of the core experiment. Mismatches in optical path lengths of the two
interferometer arms are present due to offsets needed for the interferometer readout such
as DC offsets and Schnupp asymmetry, and the limited ability to match both arm lengths
perfectly equal in optical path length. Laser frequency noise couples into the output of
an interferometer. Elaborate stabilization techniques are required to meet the AEI 10 m
Prototype's aim of becoming a test facility for the next generation of gravitational wave
observatories.

2.4.1 Laser Source

The laser system at the AEI 10 m Prototype was designed in cooperation with the AEI
and the LZH. It was developed to operate in the km-scale gravitational wave observatories
aLIGO and GEO 600. At the AEI 10 m Prototype, a two stage laser system is implemented,
similar to the one used in enhanced LIGO (eLIGO). The first stage is formed by the master
laser and input optics to the second stage. It consists of an amplifier to reach the desired
output power of 35 W.
The seed light is provided by a commercial Mephisto monolithic non-planar ring-oscillator
(NPRO) from InnoLight GmbH with an output power of 2 W at a wavelength of 1064 nm.
The laser is equipped with three different actuators that are used for the frequency reference
cavity control loop, described in section 3.4.2. A Peltier element is placed under the NPRO
and allows slow control on the laser frequency by changing the crystals temperature. In
addition, the NPRO is equipped with a Piezo-electric transducer acting as an actuator for
the mid-frequency regime. The laser frequency is modified by applying pressure to the
laser crystal and modifying the refractive index of the material and the optical path length.
The third actuator is an EOM inserted into the beam after the laser.
Figure 2.10 shows the optical layout of the laser system. Behind the NPRO $\lambda/2$- and $\lambda/4$-
wave plates are placed, followed by a polarizing beam splitter (PBS) to convert residual
elliptically polarized fractions of the light into linear polarization and assure a pure linearly
polarized laser beam.

The light is transmitted through an EOM which not only acts as fast actuator for the frequency reference cavity but also generates phase modulation sidebands at 35.5 MHz for stabilizing the mode cleaner cavity.

Behind the EOM a lens focuses the beam into an AOM, used for intensity modulation of the beam and actuator for the Intensity Stabilization System (ISS) control loop; see subsection 2.4.3 and [Jun17].

The second stage of the two stage laser system is formed by the amplifier. It consists of four neodymium doped yttrium orthovanadate crystals (Nd : YVO$_4$) pumped by fiber-coupled laser diodes at a wavelength of 808 nm [Fre07]. This results in an total output power of 35 W and approximately 95 % of the light in the fundamental Gaussian mode. The amplification stage together with the first stage of the laser system is also shown in figure 2.10.

The pre-stabilized laser system is placed outside the vacuum environment of the AEI 10 m Prototype on an optical bench. Owing to laser safety reasons and to protect it from environmental influences, it is housed in an aluminum box. A 4.5 m long photonic crystal fiber couples the light into the vacuum system. This set-up was chosen in order to provide a first stage of mode cleaning due to the mode selective properties of the fiber. An additional advantage compared to free beam propagation via a view port is the independence of relative positions of the optical benches inside and outside the vacuum system. After passing the fiber 99.16 % of the light is in the fundamental transverse electromagnetic mode TEM$_{00}$ [Opp17].

2.4.2 Mode Cleaner Cavity

The performance of the sub-SQL interferometer and other experiments at the AEI 10 m Prototype is dependent on the amount of light in the Gaussian fundamental mode. Higher order modes degrade the sensitivity of the interferometer. For mode cleaning purposes a triangular optical cavity is installed in the vacuum system of the AEI 10 m Prototype on the central optical bench. This mode cleaner cavity consists of two flat and one curved mirror with a radius of curvature of 1 m glued on an Super Invar ® spacer. This material was chosen for its low thermal expansion coefficient of 0.63×10^{-6} 1/K. The round trip length of the cavity is 53 cm [Opp17]. A finesse of 937 and a cavity g-factor of 0.74 allow sufficient suppression of higher order modes in the transmitted light. The length of the mode cleaner is stabilized to the laser frequency with a Pound-Drever-Hall (PDH) sensing scheme [Bla01]. A photodiode in reflection monitors the reflected light of the cavity. The curved mirror is equipped with a piezo-electric transducer which functions as actuator to vary the cavity length.

The mode cleaner cavity together with the fiber coupler as well as the mode matching and steering optics are placed on a bread board on the seismic isolation table inside vacuum. [Opp17].
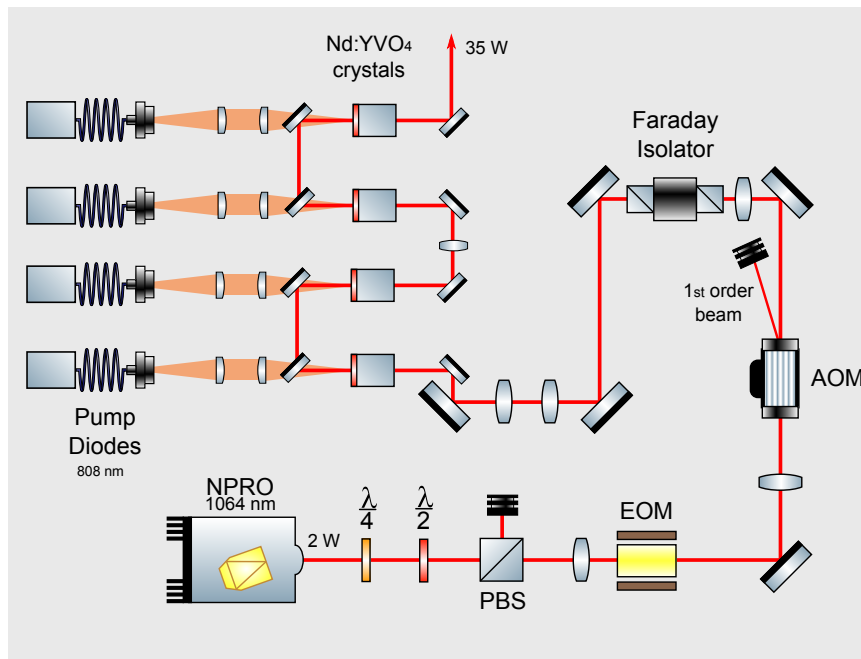
Figure 2.10: Optical layout of the laser system at the AEI 10 m Prototype. The master laser is a 2 W commercial Mephisto monolithic non-planar ring oscillator (NPRO). After passing some optical components such as an EOM for phase modulation and an AOM for intensity modulation the light enters an amplification stage. This consists of four $Nd:YVO_4$ crystals pumped by fiber-coupled pump diodes at 808 nm. After passing the amplifier the output power is increased to 35 W.

2.4.3 Intensity Stabilization System

For high-precision measurements, the laser source must be stabilized with respect to the intensity noise. The intensity stabilization requirement for the AEI 10 m Prototype Interferometer is $2 \times 10^{-9} \, \mathrm{Hz}^{-1/2}$ in a frequency band between 100 Hz and 1 kHz [Jun17]. In order to fulfill these requirements, the ISS from aLIGO was adopted and built onto the central optical bench inside the AEI 10 m Prototype vacuum system.

The laser intensity is detected by photodiodes and is fed back to an AOM in order to actuate onto the laser light and control its intensity. The detection photodiodes should be shot noise limited. With increased laser power more noise is introduced. For shot noise reduction purposes and longterm stability a set-up of four identical photodiodes was chosen. The input beam is split into four beams with identical power and is distributed on four in-loop photodiodes to control the intensity of the laser. In addition, four out-of-loop monitoring photodiodes are implemented.

Figure 2.11 shows the optical layout of the ISS in the vacuum system. The ISS uses a

pick-off of the light going to the prototype experiments like the sub-SQL interferometer and the frequency reference cavity. The input beam for the ISS is adjusted by two lenses. A combination of a $\lambda/2$-wave plate and polarizing beam splitter serves as a power adjustment stage to control the input light power to the ISS. For stray light reduction, the set-up is enclosed in an aluminum housing. Each of these laser beams is detected by an indium gallium arsenide (InGaAs) photodiode under an angle of $45°$ to avoid reflections back onto the photodiodes. In addition, absorption filters, not shown in figure 2.11, are implemented to reduce the amount of scattered light. The two photodiode arrays are placed on top of each other in order to reduce the footprint of this experiment. The AOM behind the laser is used as actuator for the intensity stabilization control loop.
The intensity stabilization at the AEI 10 m Prototype reaches a stability of $1.8 \times 10^{-9}\,\mathrm{Hz}^{-1/2}$ between 100 Hz and 1 kHz [Jun17].
More detailed information about the intensity stabilization at the AEI 10 m Prototype can be found in [Jun16], [Jun17] and [Opp17].

2.4.4 Laser Frequency Stabilization System

In order to provide a highly stabilized laser source for the sub-SQL interferometer the laser frequency noise at the AEI 10 m Prototype needs to be suppressed to a level of $10^{-4}\,\mathrm{Hz}/\sqrt{\mathrm{Hz}}$ at 20 Hz decreasing to below $10^{-6}\,\mathrm{Hz}/\sqrt{\mathrm{Hz}}$ at 1 kHz [Kaw10]. To achieve this high level of stability a triangular suspended free space cavity was set up in the vacuum system of the AEI 10 m Prototype facility. Since the laser frequency noise scales inversely proportionally to the cavity length, this was chosen to be as long as possible. This triangular cavity consists of two flat mirrors and one curved mirror, set up along one arm of the vacuum tube connecting central and south tank and hence separated by approximately 10 m. This results in a cavity round trip length of 21.2 m. The cavity mirrors are suspended in triple pendulum stages to reduce the influences of seismic noise coupling into the cavity suspensions, see also 3.3.1. A PDH sensing scheme is used in reflection of this cavity to control its length. The frequency reference cavity will be described in more detail in chapter 3.
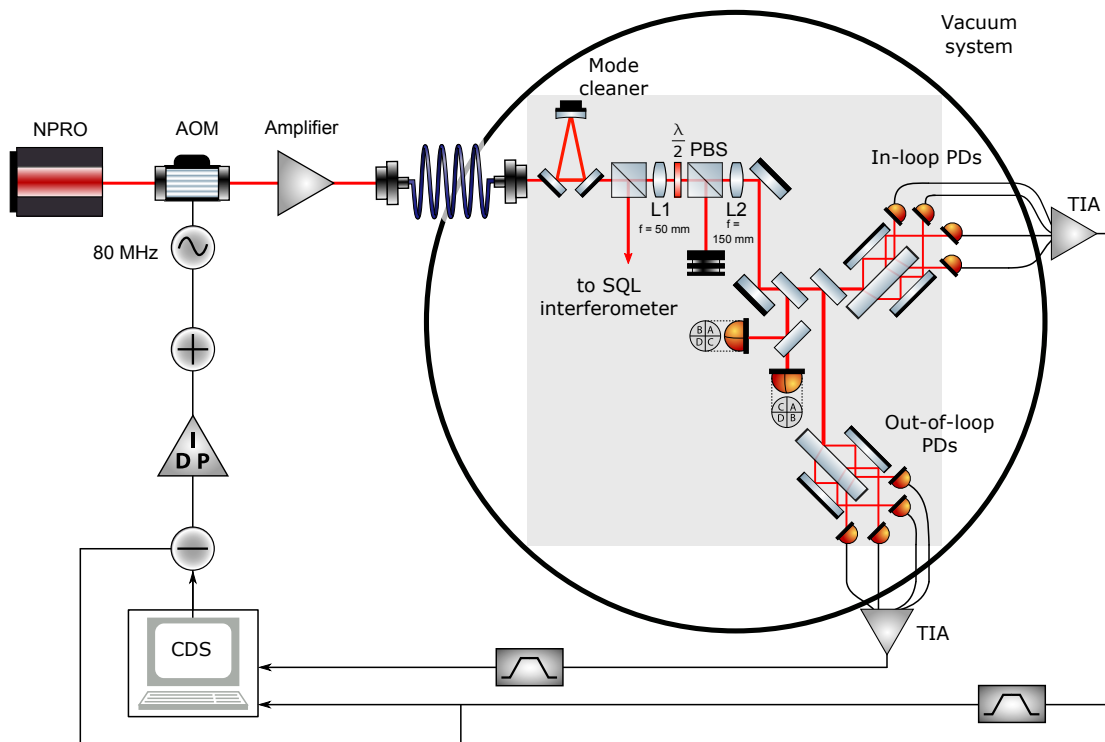
Figure 2.11: Sketch of the intensity stabilization at the AEI 10 m Prototype. The laser light is coupled into the vacuum system via an optical fiber. The ISS uses a pick-off of the main beam which is distributed equally onto four in-loop photodiodes. The measured laser intensity signal is fed back to the AOM in order to actuate onto the laser and control its intensity.

CHAPTER 3

Laser Frequency Stabilization

For high-precision experiments below the SQL all classical noise sources need to be suppressed, as discussed in chapter 2.1. Seismic noise contributions at the AEI 10 m Prototype are minimized by the AEI-SAS and the SPI, described in section 2.3.1 and 2.3.2. Further seismic noise reduction is achieved by using suspended mirrors as the triple suspension systems for the main optics. Laser intensity noise is reduced by the implementation of the ISS; see section 2.4.3.

A noise contribution limiting the performance of an interferometer is laser frequency noise, which is the main focus of this chapter. Both laser frequency fluctuations and cavity length variations result in the same signal converted to phase and cannot be distinguished from each other.

During this PhD thesis an ancillary triangular suspended cavity, in the following called frequency reference cavity, was assembled and commissioned. Its aim is to provide a stable length reference to which the laser frequency can be stabilized.

In a Michelson interferometer with exactly equal arm lengths laser frequency noise is canceled due to common mode rejection. Arm lengths differences relative to each other cause frequency fluctuations in the interferometer coupling to the output.

The laser frequency noise of the free running NPRO is $100\,\mathrm{Hz}/\sqrt{\mathrm{Hz}}$ at $100\,\mathrm{Hz}$. In order to fulfill the requirements for frequency noise suppression the free running laser noise needs to be suppressed down to a level of $10^{-4}\,\mathrm{Hz}/\sqrt{\mathrm{Hz}}$ at $20\,\mathrm{Hz}$ decreasing to below $10^{-6}\,\mathrm{Hz}/\sqrt{\mathrm{Hz}}$ at $1\,\mathrm{kHz}$ [Kaw10] with a $1/f$-slope. This corresponds to a suppression of $140\,\mathrm{dB}$ at $100\,\mathrm{Hz}$.

Figure 3.1 shows the laser frequency noise for the free running laser in comparison to the target of frequency noise suppression. This is set by the SQL including a safety margin of two orders of magnitude. It shows a noise projection of the free running NPRO frequency noise (blue line) and the frequency noise suppression target in the SQL measurement band (red line) as it would be measured by the frequency reference cavity. A noise suppression of almost seven orders of magnitude is required to reach the target at $100\,\mathrm{Hz}$ assuming a common mode rejection of a factor of hundred for the sub-SQL interferometer [Kaw10].
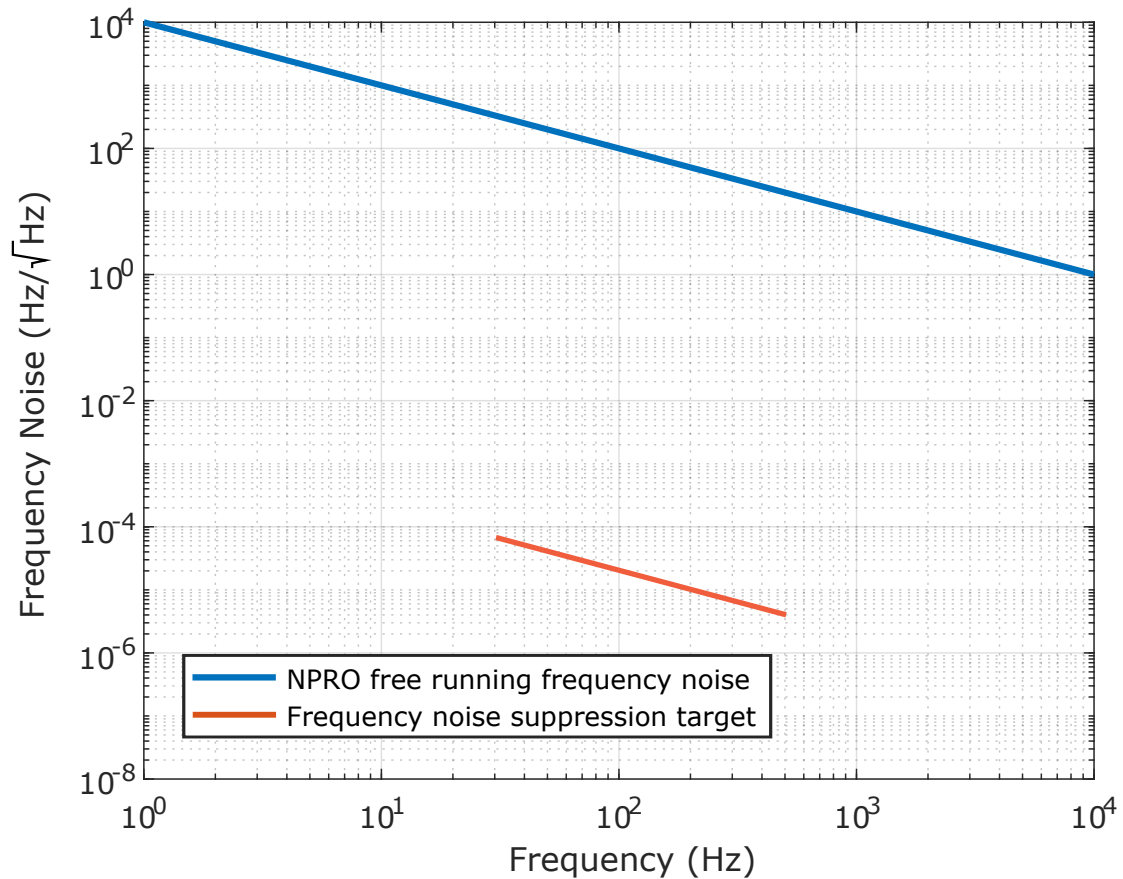
Figure 3.1: Laser frequency noise of the free running laser in comparison to the target set by the SQL in the SQL measurement band including a safety margin of two orders of magnitude. The free running NPRO frequency noise (blue line) and the theoretical requirement for frequency noise suppression (red line) is shown.

3.1 Laser Frequency Stabilization at Gravitational Wave Observatories

Before the frequency reference cavity is presented in detail, an overview about laser frequency stabilization at various gravitational wave observatories is described in this section. The stabilization schemes of Advanced LIGO (aLIGO), Advanced Virgo and GEO 600 are presented in the following section and the differences to the laser frequency stabilization at the AEI 10 m Prototype are shown. A more detailed overview about aLIGO, Advanced Virgo and GEO 600 can be found in [Aas15], [Ace14] and [Aff14b].

3.1.1 Advanced LIGO

The light source for the aLIGO gravitational wave observatory is a pre-stabilized laser system (PSL) consisting of three stages. It was developed at the AEI Hanover in cooperation with the LZH. The first two stages are identical to the PSL at the AEI 10 m Prototype, described in 2.4.1. A commercial NPRO from InnoLight GmbH forms the first stage of this laser system. It has an output power of 2 W. The light passes the second stage, an amplifier consisting of four diode-pumped Nd : YVO$_4$ crystals. This results in an output power of 35 W. The third stage consists of an injection-locked ring oscillator with total output power of 220 W, also diode-pumped at a wavelength of 808 nm [Win11], [Kwe12]. The laser source is stabilized in intensity, beam pointing, mode content and frequency. In order to suppress frequency noise a stabilization chain using three different optical cavities is implemented at LIGO [Hal]; a rigid linear cavity, the suspended input mode cleaner cavity and the common mode arm length of the Dual Recycled Fabry-Perot Michelson Interferometer (DRFPMI). The phase modulation frequencies are 21 MHz, 24 MHz and 9.1 MHz. A schematic of aLIGO with the frequency stabilization control loop is shown in figure 3.2.

Initial frequency stabilization is provided by stabilizing the laser to a linear high finesse 20.3 cm long fused silica cavity with a bandwidth of 77 kHz [Aas15]. A standard PDH locking scheme in reflection of the rigid cavity is obtained by demodulating at 21 MHz. The PDH error signal is fed back to three different actuators controlling different frequency ranges. The unity gain frequency of the control loop is 200 kHz [Hal]. For slow control, temperature feedback to the laser crystal is implemented, realized with a peltier element below the laser crystal. A piezo-electric transducer attached to the NPRO covers the mid-frequency ranges. For fast actuation and broadband phase correction an EOM is implemented in the system between the NPRO and the 35 W amplification stage.

In the second stabilization stage, the laser frequency is locked to the suspended triangular input mode cleaner. A PDH error signal in reflection is obtained by demodulating at 24 MHz. The unity gain frequency of this control loop is 50 kHz [Hal]. The error signal of the mode cleaner is added to the fused-silica cavity error point to stabilize the laser frequency to the input mode cleaner. This is achieved by actuating on an AOM placed in front of the table-top frequency reference cavity.

In addition to these two frequency stabilization systems, the laser is frequency-locked to the common mode arm length of the DRFPMI, acting as a 4 km long frequency reference cavity with a linewidth of 1 Hz [Hal]. A PDH error signal in reflection is obtained by demodulating at 9.1 MHz in a 15 kHz bandwidth loop. The error signal is fed back to the length of the mode cleaner and in addition summed to the error point of the mode cleaner feedback loop. In this way, the laser frequency can be stabilized to the common arm length of the DRFPMI.

The frequency noise is suppressed down to 10^{-6} Hz/$\sqrt{\text{Hz}}$ between 10 Hz and 100 Hz increasing with an $1/f$-slope at higher frequencies assuming 35 W of input power to the

interferometer. This is brought further down to $10^{-8}\,\mathrm{Hz}/\sqrt{\mathrm{Hz}}$ at $100\,\mathrm{Hz}$ by passively filtering the frequency noise above the common mode cavity pole.

In contrast to the $40\,\mathrm{kg}$ test masses at aLIGO, the sub-SQL interferometer at the AEI $10\,\mathrm{m}$ Prototype uses $100\,\mathrm{g}$ mirrors for measuring radiation pressure noise. As a consequence, the sub-SQL interferometer cannot be used as a stable length reference for the laser frequency and an ancillary cavity is required to provide the demanded frequency stability.

3.1.2 Advanced Virgo

The Italian Advanced Virgo detector in Cascina, one of the large-scale interferometric gravitational wave detectors, is a dual recycled Fabry-Perot Michelson interferometer with an arm length of $3\,\mathrm{km}$. Advanced Virgo uses a rigid frequency reference cavity, the input mode-cleaner and the common mode arm length of the Fabry-Perot Michelson interferometer for frequency stabilization. More details can be found in [Ace14], [Bon02] and [Bon96].

The detector facility provides a quiet environment minimizing the dominating noise sources at low frequencies such as seismic motion, acoustic coupling and thermal noise. All core optics are suspended as multi-pendulums from the so-called super attenuators which provide a low seismic noise environment. Since the frequency stabilization requirement is many orders of magnitude below the free running laser noise an additional pre-stabilization is necessary [Bon02].

The laser frequency is initially locked to a rigid triangular high-finesse frequency reference cavity. The cavity optics, two flat and one curved mirror, are attached to a ceramic spacer with a low thermal expansion coefficient. A second identical Fabry-Perot cavity is implemented as an out-of-loop sensor to evaluate residual frequency fluctuations [Bon96]. For locking the laser to the frequency reference cavity a PDH feedback control loop in reflection is used. To cover a large actuation bandwidth three different actuators are installed, a peltier element, a piezo-electric transducer and an EOM.

In addition to the rigid frequency reference cavity, the input mode cleaner is used for frequency stabilization. It is a triangular $143\,\mathrm{m}$ long cavity with suspended mirrors. The mode cleaner cavity is following the laser frequency which in turn is locked to the rigid frequency reference cavity. The last stabilization stage is the frequency lock to the common mode arm length of the Fabry-Perot Michelson interferometer.

3.1.3 GEO 600

GEO 600 is a gravitational wave detector in Ruthe close to Hanover in Germany, developed in a German-British collaboration [Gro03], [Aff14b]. Its core instrument is a dual recycled Michelson interferometer with an arm length of $600\,\mathrm{m}$ folded once to increase the effective arm length to $1200\,\mathrm{m}$.

The smaller baseline of GEO 600 compared to aLIGO and aVirgo poses a clear disad-
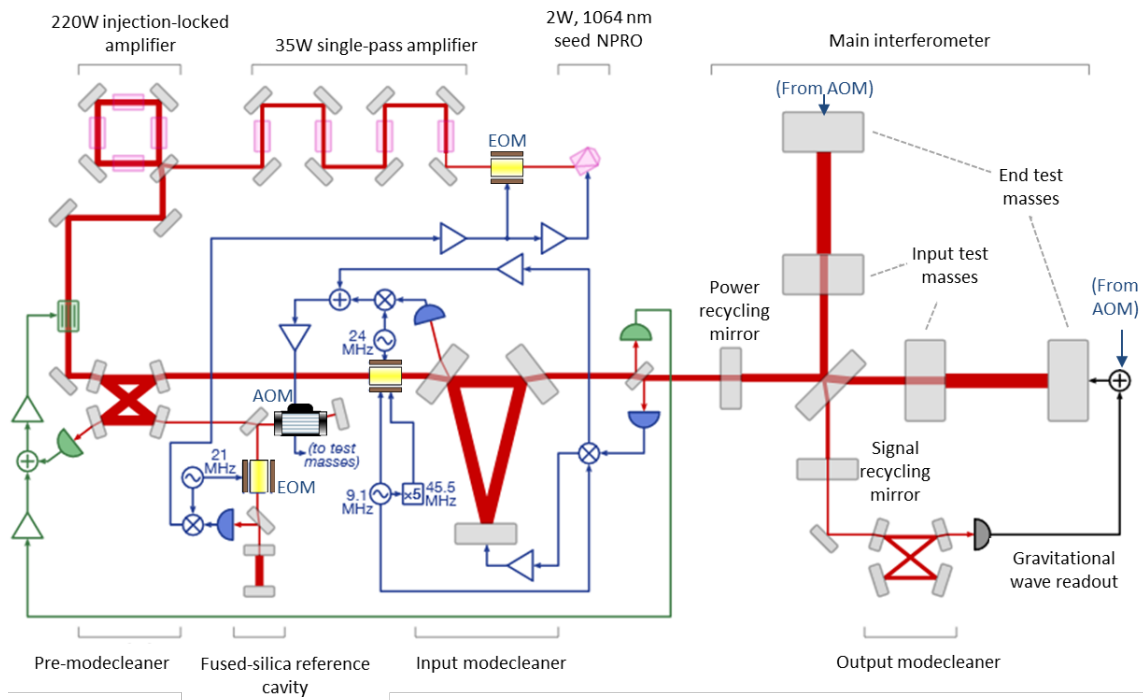
Figure 3.2: Schematic of the aLIGO including the control loops for frequency stabilization (blue trace) and intensity stabilization (green trace). Figure from [Hal].

vantage with respect to the sensitivity of the instrument. This disadvantage is partly compensated by pioneering so called second generation technologies such as monolithic suspensions or signal recycling from an early stage on [Aff14a]. Another prime example is the early use of squeezing [Aba11]. From 2011 till writing of this thesis squeezing is routinely applied during operation of GEO 600 [Sch18].

Due to the Schnupp asymmetry in the interferometer arms, the Michelson interferometer is sensitive to frequency fluctuations of the incident laser light.

The main goals for frequency stabilization are to minimize the noise coupling into the interferometer in the gravitational wave band from 50 Hz to 5000 Hz and to reduce the Root Mean Square (RMS) frequency noise for all frequencies to facilitate lock acquisition of the power recycling cavity [Gro03].

To accomplish the laser frequency noise requirements of GEO 600, $100\,\mu\text{Hz}/\sqrt{\text{Hz}}$ [Bro99], a stabilization chain was implemented that includes the two suspended input mode cleaners and the suspended power recycling cavity.
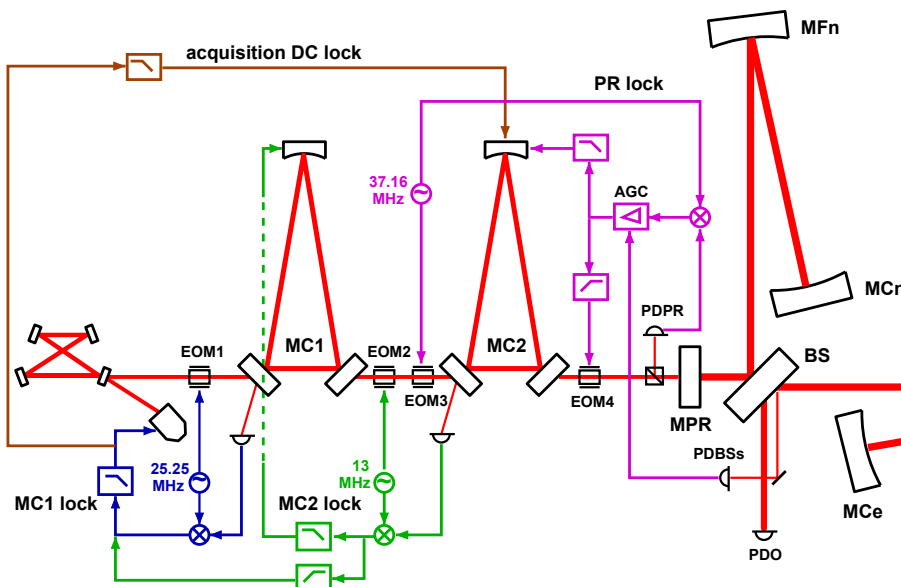
Figure 3.3 shows a schematic overview about the frequency stabilization chain at GEO 600 related to the power recycling lock. Simplified, the frequency stabilization chain works as follows: In case that only the first mode cleaner (MC1) is locked it serves as a frequency

reference cavity for the laser. The stabilization is achieved with a PDH control scheme in reflection of MC1. The phase modulation sidebands are created with an EOM (EOM1) in front of MC1. When MC1 is locked, the transmitted light reaches the second mode cleaner (MC2) and is stabilized to this. This is achieved by adjusting the length of MC1 since the laser follows this cavity. A PDH control loop is implemented with sidebands generated by another EOM (EOM2).

When both mode cleaner cavities are locked, the suspended power recycling cavity, formed by the power recycling mirror and the Michelson interferometer, is used for laser frequency stabilization with another PDH scheme. Phase sidebands are generated by EOM3.

In case that all three feedback loops are running the laser light is stabilized to the free hanging power recycling cavity. Since the mirrors of the 1200 m long power recycling cavity are suspended as double and triple pendulums they provide a sufficient seismic isolation and length fluctuations of the cavity are minimized.

More details can be found in [Gro03] and in [Aff14b].

Figure 3.3: Schematic control topology of the power recycling lock and the related frequency stabilization chain at GEO 600. Figure from [Gro03].

3.2 Frequency Reference Cavity at the AEI 10 m Prototype

The frequency reference cavity at the AEI 10 m Prototype is designed to provide a highly stable reference in terms of frequency noise for the sub-SQL interferometer in a frequency band from approximately 20 Hz to 1 kHz. An overview about the proposed design of the frequency reference cavity can be found in [Kaw10].

A seismically isolated environment is required to ensure a stable cavity length and minimize frequency fluctuations. The AEI 10 m Prototype facility with its vacuum system minimizing acoustic coupling and air flow, the seismic attenuation system and the inter-table control with the SPI provides the necessary environment conditions. Triple suspensions for the cavity mirrors ensure an isolation of seismic motion of the optics.

The frequency reference cavity is assembled inside the vacuum system along the vacuum tube connecting the central and south tank of the facility. The cavity mirrors are located on two of the in-vacuum optical tables to achieve a long round trip length of the cavity. Equation 3.1 shows the dependence of the relative laser frequency noise $\frac{\Delta f}{f}$ on cavity length deviations where L is the cavity length and ΔL the displacement noise of the cavity mirrors relative to the cavity length

$$\frac{\Delta f}{f} = \frac{\Delta L}{L}. \tag{3.1}$$

Since the laser frequency noise scales inversely proportionally to the cavity length this was chosen to be as long as possible. At the same time the cavity needs to fit to the dimensions of the vacuum system.

Figure 3.4 shows an overview of the frequency reference cavity properties including the distances between the mirrors and their reflectivities. The in-vacuum assembly including a simplified input path and the reflected and transmitted beam is shown in figure 3.5.

The cavity consists of two flat mirrors, the input and the output mirror, which are placed in the southeast corner of the central SAS. The curved mirror is placed on the south table and is separated by 10.44 m from the two flat mirrors. This set-up results in a round trip length of 21.2 m. The mode separation of p-polarization and s-polarization in a triangular cavity makes this arrangement well suited and offers practical advantages compared to linear cavities.

The input and the output mirror are separated by 0.32 m. Due to the geometry of the triangular cavity, the angle of beam propagation between mirror and optical axis at the input and output mirror is 89.1° and at the pointed angle at the curved mirror 1.8°. The Radius Of Curvature (ROC) of the curved mirror is 37.8 m.

An optical cavity is denominated as stable when the cavity g-factor is between $0 \leq g \leq 1$. The frequency reference cavity's g-factor is calculated as 0.67 which indicates it as optically stable.

Transversal modes of the cavity describe the spatial beam profile perpendicular to the optical axis. A Gaussian beam intensity profile shows maximal intensity centered around
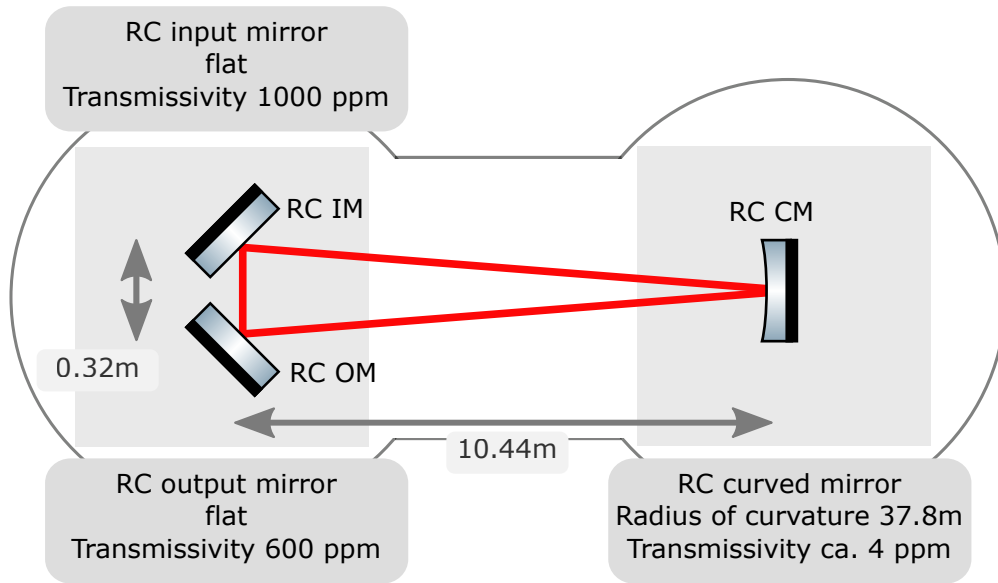
Figure 3.4: Properties of the frequency reference cavity. The two flat mirrors are placed on the central SAS while the Curved Mirror (CM) is assembled in a distance of 10.44 m onto the south SAS. The Input Mirror (IM) and the Output Mirror (OM) are separated by 0.32 m.

the optical axis. For mode-matching into the cavity, the laser light needs to be in the fundamental transversal electro magnetic mode, also called TEM_{00}. This is provided by the photonic crystal fiber and by the mode cleaner cavity as mentioned in 2.1.

The finesse of a cavity is defined by the relation of the Free Spectral Range (FSR) and the Full Width at Half Maximum (FWHM)

$$\mathscr{F} = \frac{FSR}{FWHM}. \tag{3.2}$$

It it related to the storage time of the light resonating inside the cavity and is dependent on the losses inside the cavity and the length.

The finesse of the frequency reference cavity is

$$\mathscr{F} = \frac{14.2\,\text{MHz}}{3.97\,\text{kHz}} = 3580$$

with a FSR of 14.2 MHz and a FWHM of 3.97 kHz.

The properties of the frequency reference cavity are summarized in table 3.1. A detailed theoretical background about optical cavities can be found in [Kog66].
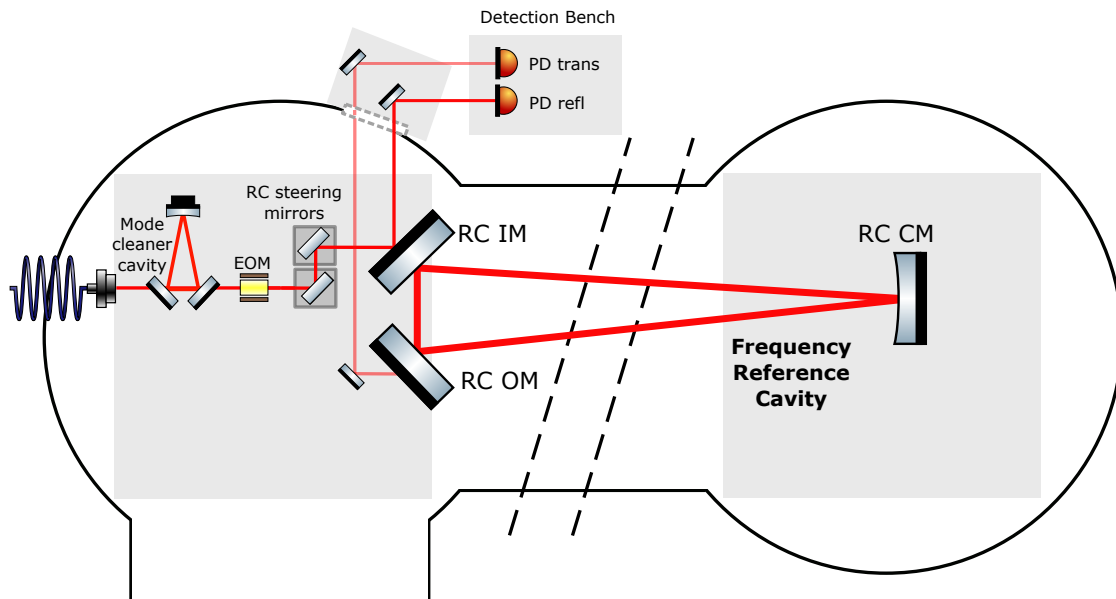
Figure 3.5: Set-up of the frequency reference cavity inside the AEI 10 m Prototype vacuum system including the input path as well as reflected and transmitted beams. To achieve a long round trip length of the cavity the input mirror and the output mirror are placed on the central optical bench while the curved mirror is located on the south optical table. This results in a round trip length of 21.2 m. The triangular layout separates input beam and reflected beam without additional polarization optics. Both the reflected and the transmitted beam of the cavity are guided through view ports out of the vacuum system and are detected on an optical bench with photo detectors.

3.2.1 Requirements and Noise Performance

The requirements for allowed frequency fluctuations in the input beam to the sub-SQL interferometer are given by the SQL, introduced in chapter 2, and by the expected common-mode rejection ratio. The latter is assumed to be 1 % [Kaw10]. These requirements were discussed in the beginning of this chapter and are shown in figure 3.1.
Figure 3.6 shows the sensitivities for the frequency reference cavity in equivalent length noise. The free running NPRO noise is shown by the dark blue line. It is approximately seven orders of magnitude above the other noise contributions at 100 Hz. Classical radiation pressure noise is displayed by the red line. This modeled noise performance is including the ISS. Quantum radiation pressure noise is well suppressed due to the 850 g mirrors and not shown here. The sensitivity of the frequency reference cavity at 100 Hz is limited by substrate thermal noise (gray line) and suspension thermal noise (purple line). At frequencies above 2 kHz it is limited by shot noise (magenta line). Other noise contributions are coating thermo-elastic noise (yellow line), coating thermo-refractive noise (light blue)

Table 3.1: Properties of the frequency reference cavity.

Finesse	3580
Input Power	266 mW
Circulating Power	ca. 800 W
Linewidth	3.97 kHz
Free Spectral Range	14.2 MHz
Round Trip Length	21.2 m
Modulation Frequency	8.047 MHz
Cavity g-Factor	0.67
Cavity Waist	2.4 mm
Mirror Mass	850 g
ROC RC CM	37.8 m
Light Polarization	p-Polarization

and seismic noise in vertical (light green) and horizontal (brown).

In addition to the requirements for frequency stability, the frequency reference cavity should also meet the requirements for high vacuum compatibility for AEI 10 m and enable automated long-term operation.

Since the cavity is built into a vacuum environment, a high standard in terms of vacuum compatibility is required. All in-vacuum parts of the cavity and the input optics need to be manufactured with vacuum compatible materials. Most of the components are fabricated out of aluminum or steel. Only certain synthetic materials can be used inside the vacuum environment. That includes cables and connectors that are needed to connect the experiments to the electronics outside of the vacuum system.

Damping Requirements

The goal of damping is to reduce the cavity mirror motion and to damp the suspensions at the pendulum resonance frequencies. Due to their design as triple pendulums, the suspensions for the frequency reference cavity are well-suited to provide seismic isolation at frequencies above 10 Hz. At their resonance frequencies they show a declined isolation performance and can be noisier than the free running laser. Active damping of the suspensions around their resonance frequencies from approximately 0.5 Hz to 10 Hz is required. This involves sensors and actuators that sense the position of the mirror and control it by a feedback control loop.

Damping at the frequency reference cavity suspensions is discussed in more detail in chapter 4.
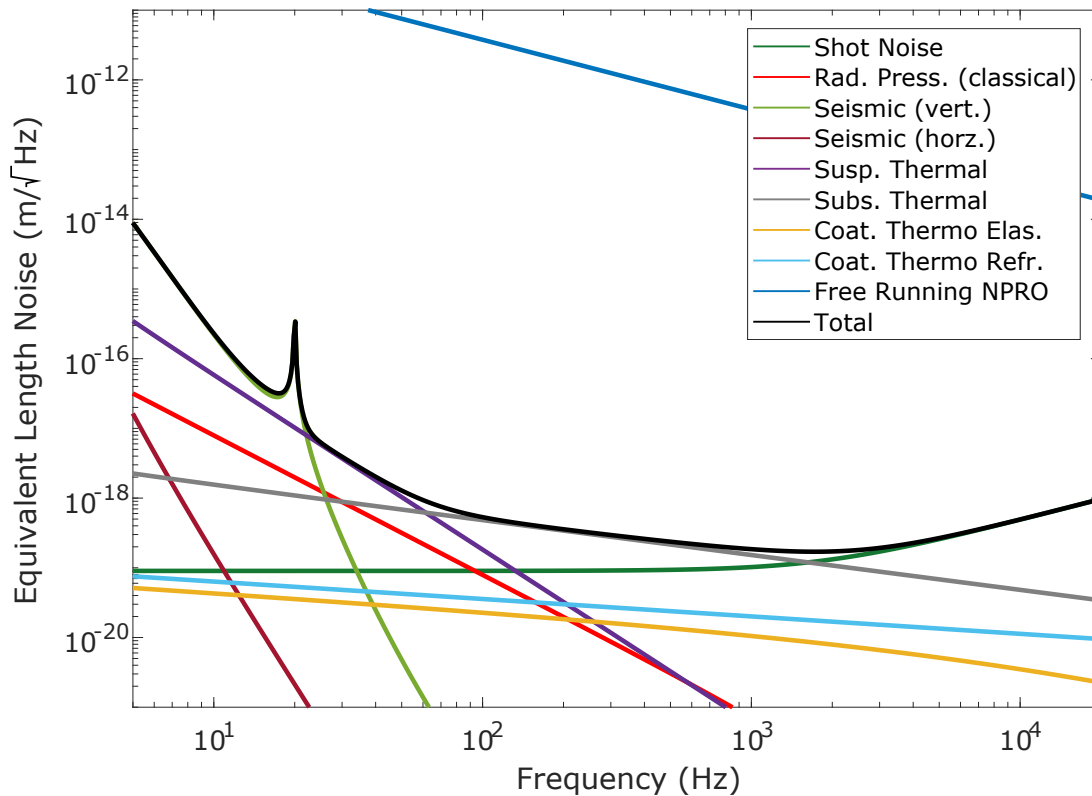
Figure 3.6: Noise budget of the frequency reference cavity. The noise contributions are shown in equivalent length noise in dependence on the frequency. The free running NPRO noise is depicted by the dark blue line and is approximately seven orders of magnitude above the other noise contributions. The sensitivity of the frequency reference cavity at 100 Hz is limited by substrate thermal noise (gray line) and suspension thermal noise (purple line). At higher frequencies above 2 kHz it is limited by shot noise (magenta line). Classical radiation pressure noise is displayed by the red line and includes the noise performance with the ISS. Coating thermo-elastic noise (yellow line), coating thermo-refractive noise (light blue) and seismic noise in vertical (light green) and horizontal (brown) are not limiting the sensitivity of the frequency reference cavity. This simulation was performed with Matlab originating from T. Westphal and modified by D. Wu.

Automated Operation

The automatic operation of the frequency reference cavity is required for the operation of the sub-SQL interferometer. This includes the demand on long term stability of the cavity and the ability to re-lock independently in case of loosing lock. The experimental set-up of the frequency reference cavity, including the electronics, should ensure a disturbance-free process and actively counteract any lock loss and keep the experiment running. This is provided by an auto-alignment system, further described in section 3.4.3, that allows a well-defined beam position in the cavity and adjusts the input beam automatically.

3.2.2 Noise Sources

Laser frequency fluctuations and cavity mirror displacements resulting in cavity length changes can not be distinguished from each other since their signal is identically converted to phase. This sets the requirements for the frequency reference cavity length stability. This stability is affected by different noise contributions that are listed in the following.

Shot Noise and Quantum Radiation Pressure Noise

In chapter 2 an introduction to shot noise and quantum radiation pressure noise was given. The crossover frequency of these two quantum noise contributions is linearly dependent on the input power in an interferometer and of the cavity mirror masses. This cannot be surpassed with classical approaches and is called SQL.
As mentioned before, the sub-SQL interferometer cannot be used as length reference for the laser frequency since the 100 g optics are too susceptible to radiation pressure noise. The frequency reference cavity mirrors with a mass of 850 g are heavy compared to the sub-SQL interferometer optics to minimize radiation pressure noise effects.
The input power of 266 mW to the frequency reference cavity was chosen in order to keep the shot noise and the radiation pressure noise below the required noise level. The finesse of the cavity was initially adjusted to ensure an optimized shot noise limited performance.

Seismic Noise

Seismic noise originates from the intrinsic motion of the ground, caused by natural or artificial sources. The pre-isolation from seismic noise in the AEI 10 m Prototype laboratory is provided by the AEI-SAS from 0.2 Hz on. The frequency reference cavity mirrors are passively isolated from ground motion above 10 Hz. Around the resonance frequencies from 0.5 Hz to 10 Hz the motion is enhanced compared to not suspended mirrors. Active damping is applied to damp these resonances, described in chapter 4. This improves the low-frequency performance of the suspensions without inducing noise at higher frequencies in the SQL frequency band of interest from 30 Hz to 1 kHz.
The measured seismic noise in the AEI 10 m Prototype laboratory is $10^{-7}\,\mathrm{m}/\sqrt{\mathrm{Hz}}$ at 1 Hz, rolling off with a slope of $1/f^2$ at higher frequencies [Kaw10]. The requirement in terms

of seismic noise performance of the frequency reference cavity is $10^{-18}\,\mathrm{m}/\sqrt{\mathrm{Hz}}$ at $50\,\mathrm{Hz}$ [Kaw10].

Brownian Coating Thermal Noise

Brownian coating thermal noise arises from random position fluctuations on the coating driven by thermal energy. The fluctuations are larger the more dissipative the coating material is. Brownian coating thermal noise scales inversely proportional to the laser spot size on the mirrors. The beam inside the frequency reference cavity between the two flat mirrors has a waist of 2.4 mm. The spot size on the mirrors is approximately the same due to the long Rayleigh range of the cavity and the proximity of the input and output mirror.

Electronic Noise

For the stabilization of the frequency reference cavity different sensors and actuators at the suspensions are required. As each mirror of the cavity has to be controlled in all degrees of freedom, the suspensions are equipped with six pairs of sensors and actuators. Electronics noise in the suspensions arises from the noise of photodiodes and LEDs in the optical sensors. It can couple into mirror motion and disturbs the sensitivity of the cavity. To reduce the influence of electronic noise onto the suspensions the electronics are placed at the top mass of the suspension chain. The cavity mirrors are isolated from the electronic noise by a $1/f^4$ slope of the pendulum stages above their resonance frequencies.

3.3 Characterization of the Frequency Reference Cavity

The following sections describe the frequency reference cavity suspensions and their assembly, the optical cavity layout and the stabilization schemes for the cavity control. The auto-alignment system is presented in the following.

3.3.1 Triple Suspensions

The frequency reference cavity mirrors are seismically isolated by suspending them as pendulums to benefit from a $1/f^2$ slope per pendulum stage above their resonance frequencies. Figure 3.7 shows on the left side a modeled transfer function of a single pendulum from a suspended mirror to its suspension point for the example of longitudinal motion. The mirror follows the motion of the suspension point at low frequencies. At the resonance frequency the motion is enhanced before it falls off with a $1/f^2$ slope at higher frequencies above the resonance. The objective with respect to the mirror suspension design is to push the resonance frequencies of the system as low as possible to benefit from the isolation behavior at higher frequencies. Lower resonance frequencies can be achieved by increasing the wire lengths of the suspensions. This is limited due to the height of the vacuum environment and becomes experimentally inconvenient. Another option is to add multiple pendulum stages together which is used for the frequency reference cavity mirror

suspensions. The right side of figure 3.7 shows the transfer function for a triple pendulum. In this way a $1/f^2$ slope is achieved per pendulum stage which results in an overall slope of $1/f^6$ in the case of a triple suspension system.

The design of the triple pendulum suspensions for the frequency reference cavity is based on the GEO 600 mode cleaner suspensions [Tor00]. The design of a pendulum suspension with three horizontal stages and two vertical suspension stages was proposed in [Tay09]. This design was adapted for the frequency reference cavity suspensions [Wes16].

Figure 3.8 shows a photograph of the three suspension chains. Each frequency reference cavity suspension consists of three horizontal and two vertical pendulum stages. The horizontal stages are formed by three masses suspended with steel wires. It is decoupled from the vertical isolation which is provided by two sets of blade springs. They are attached to a rigid aluminum structure which hosts the complete suspension. At the top of the suspension frame two blade springs are attached. They are initially bent upwards and are installed such that they are in a straight position when the masses are suspended. At their tips small aluminum clamps are attached that hold the suspension wire. The first stage is formed by the top mass, suspended from the tips of the vertical blades with $150\,\mu m$ diameter wire.

The wires are made of high carbon-containing stainless-steel with low mechanical loss. They have a high breaking stress allowing them to carry the weight of the suspension which is in total 2.71 kg [Wes16]. Using thin wires is limited by the weight of the suspended masses and the fiber's breaking point. Thinner wires have lower thermal noise and vertical bounce modes of the suspensions are shifted to lower frequencies. The vertical bounce modes at the frequency reference cavity suspensions are around 25 Hz.

Inside the top mass two additional blade springs are installed, forming the second vertical
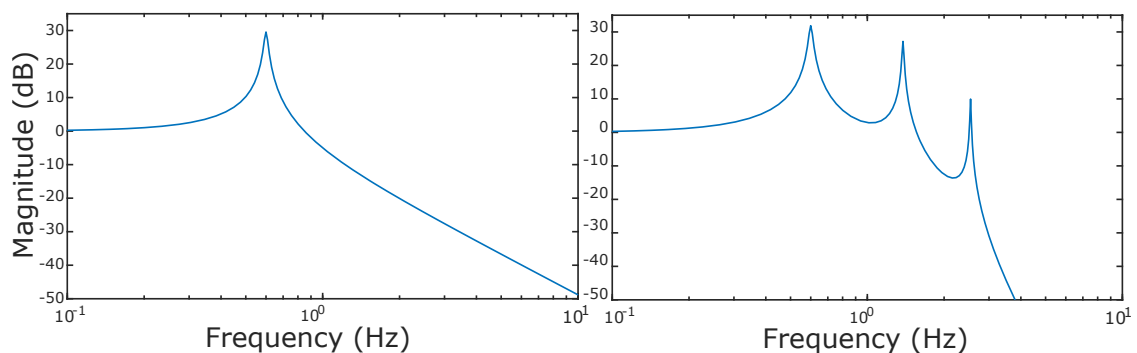
Figure 3.7: Modeled transfer function of a single pendulum suspension (left) and a triple pendulum suspension (right). The transfer function of a pendulum is flat at low frequencies and shows a resonant enhancement at its resonance frequency. Above the resonance it decays with a $1/f^2$ slope.

stage. From the tips of these two springs the wires for the second horizontal stage are suspended. These wires are installed as a pair of slings which hold the intermediate mass of the suspension. They have a thickness of 100 µm and are separated by 10 mm.

The intermediate mass is made of aluminum and has a round shape with the same outer dimensions as the mirror, a diameter of 10 cm and a thickness of 5 cm. On the sides of the intermediate mass clamps are attached that hold the lowest stage wires. The wires for this stage are 55 µm thick and are separated by 6 mm. Figure 3.9 shows a photograph of the intermediate mass of the frequency reference cavity suspensions chain.

The suspensions for the input mirror and the output mirror of the frequency reference cavity are both placed in one aluminum frame, located in the south-east corner of the central table. The suspension for the curved mirror is placed on the north-east corner of the south SAS. With a total weight of approximately 15 kg per suspension they contribute significantly to the allowed payload of the optical tables which is in total 220 kg.

Top Mass

Active control is performed at the top mass of the suspensions. Figure 3.10 shows the top mass enclosed by an aluminum safety structure to which Birmingham Optical Sensors and Electro-Magnetic actuators (BOSEMs) for position control are attached. They are mounted in six different places such that they cover all six degrees of freedom. The top mass itself is equipped with aluminum rods with flattened tips placed on cylindric magnets and reaching into the coil holder of the BOSEMs. The BOSEMs will be explained in more detail in 3.3.3.

The top mass also provides two round steel push rods for manually adjusting pitch and roll. Only the upper push rod for tuning pitch is visible in the photograph, the roll push rod is placed at the bottom of the top mass, hidden by the safety structure. Yaw can be adjusted by moving the complete suspension frame or shifting the upper vertical blades springs from where the masses are suspended.

Safety Structure for the Suspended Masses

To avoid the mass from falling in case of wire failure all three masses are surrounded by a safety structure.

The safety structure of the top mass consists of a cuboid-shaped piece of aluminum, which surrounds the top mass from all sides except of one and thus limits excessive movement. If the suspension wires break, the safety structure catches the mass and prevents complete destruction of the entire suspension, especially the mirror. The safety structure of the top mass additionally fulfills the task of the BOSEM positioning.
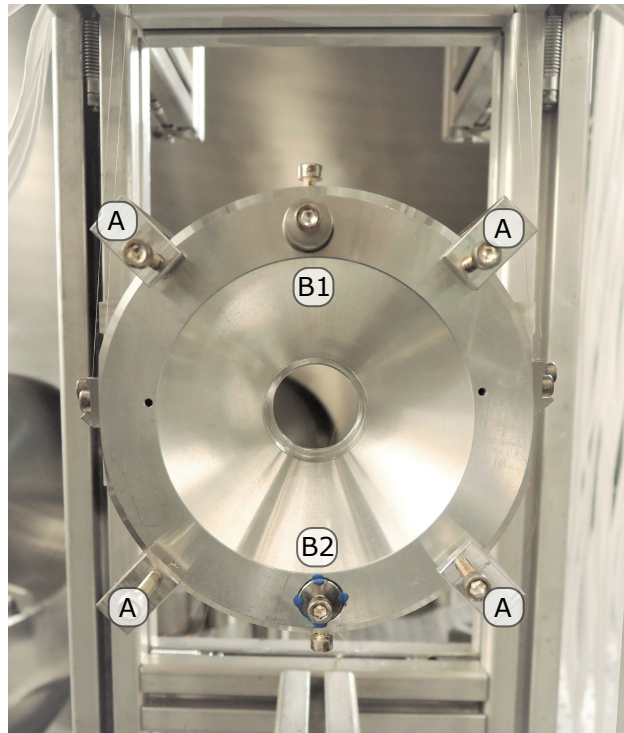
The safety structure for the intermediate mass and the mirror are similar and consist both of four flat rods with end stops at their fronts, two of them placed below the mass and two above. Their task is to prevent the mirror and the intermediate mass from falling or tilting over. They are shown in figure 3.9 for the intermediate mass and in figure 3.14 for
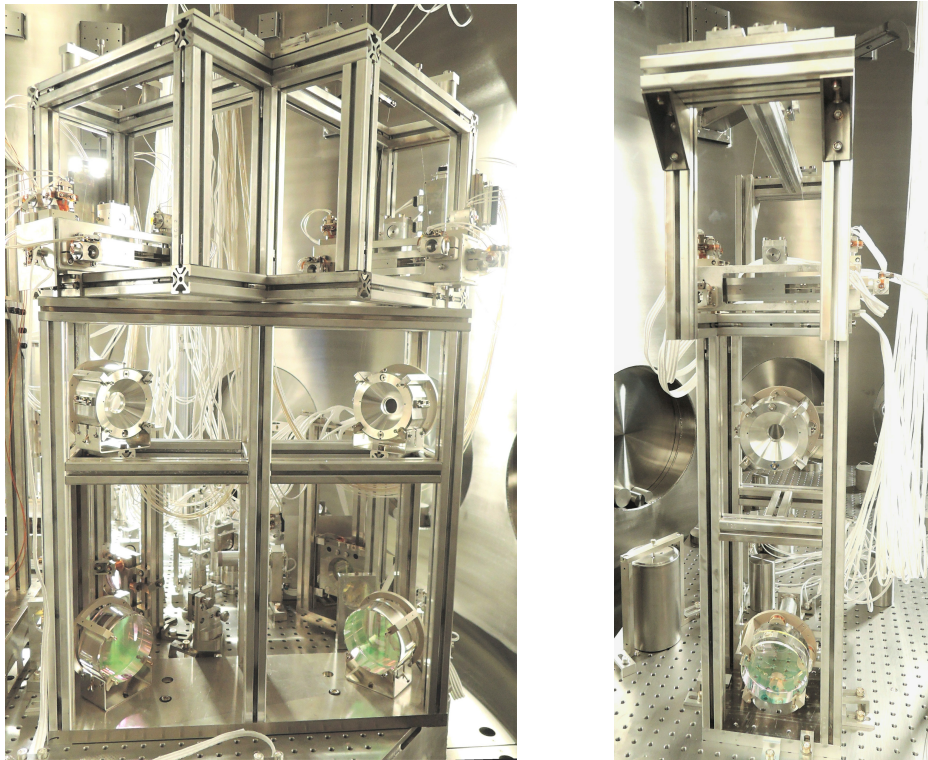
Figure 3.8: Photograph of the triple suspension systems with input and output mirror of the frequency reference cavity (left side) and the curved mirror (right side). The mirrors are suspended as triple pendulums from a rigid aluminum structure. Two vertical stages of isolation are provided by blade springs, placed at the top of the suspension chain and inside the top mass. Horizontal isolation is provided by the three pendulum stages. The top mass is suspended from the top blades by steel wires whereas the intermediate mass is suspended from the blade springs inside the top mass. The wire slings that hold the mirrors are suspended from aluminum clamps that are attached to the sides of the intermediate mass. The suspensions position sensing and control is applied at the top mass.

the curved cavity mirror. The latter is only equipped with three flat safety rods fabricated out of Polyether Ether Ketone (PEEK), a vacuum compatible synthetic. One of them was removed during installation since it was located too close to the suspensions wires due to tolerances of mechanical parts and imperfections in design and installation. The intermediate mass is secured by four flat safety rods made of aluminum as can be seen in figure 3.9.

In addition to their safety purposes, the structures can be used for clamping the masses during installation work, therefore the end stops of the safety rods are equipped with screws.

Figure 3.9: Intermediate mass of the frequency reference cavity suspension chain. It has the same outer dimensions as the cavity mirror and is surrounded by a safety structure formed by four aluminum fingers (A) to prevent the mass from falling in case of wire failure. Two steel push rods (B1) are implemented inside the mass to adjust pitch. The lower push rod (B2) was not used for alignment and fixed with vacuum compatible glue.

3.3.2 Steering Mirror Suspensions

In the incoming beam path to the frequency reference cavity two suspended steering mirrors are used to ensure the alignment of the input beam to the cavity. They are suspended as single pendulums, figure 3.11 shows a photograph and a sketch of a steering mirror suspension. The two inch mirrors are placed in an aluminum holder sitting in a single wire sling. This wire is attached with clamps to the top of the frame structure.
For position control and remote alignment of the steering mirrors they are equipped with magnets at their back which reach into coils mounted to the suspension frame. This allows a remote control of the mirrors via CDS. Eddy current damping is provided by these magnets and copper cups and by additionally implemented pairs of magnets and copper cups at the two sides of the mirrors. The steering mirrors are also used as actuators for the auto-alignment scheme of the frequency reference cavity, further explained in 3.4.3.
The steering mirrors were designed and assembled in a former PhD thesis [Wes16].
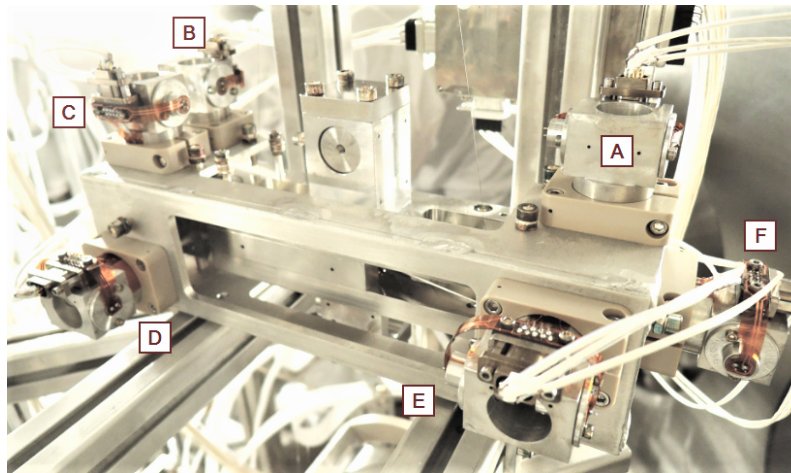
Figure 3.10: Photograph of the frequency reference cavity suspensions top mass including aluminum safety structure and BOSEMs. The BOSEMs are labeled from A-F. They are orientated in different directions to be able to cover all six degrees of freedom. The top mass is equipped with six cylindrical magnets with extended aluminum flags reaching into the BOSEM holder and blocking a fraction of the light sent from the LED to the photodiode. A change in the light power indicates a movement of the top mass. Via magnet-coil actuation, the suspension can be moved back to its original position.

3.3.3 Optical Sensors and Electro Magnetic Actuators

For the active control of the frequency reference cavity suspensions six shadow sensors with magnet-coil actuators are implemented at the top mass to control all six degrees of freedom pitch, longitudinal, transversal, roll, yaw and vertical; see 2.2.

The frequency reference cavity uses BOSEMs, provided by the University of Birmingham [Ast11]. They are used in aLIGO and were adapted for the AEI 10 m Prototype. The idea of using BOSEMs is to control the DC position of the suspensions, to supply a contactless actuation and to provide damping of the suspension chain.

A drawing and a photograph of a BOSEM are shown in figure 3.12. Every BOSEM is attached to the top mass safety structure and consists of an LED and a photodiode orientated facing each other on opposite sides inside the aluminum holder. A coil with 150 μm thick copper wire and 800 windings is wound to the holder. The electronics are connected by a vacuum compatible Kapton® circuit board.

The top mass of the suspensions is equipped with six flags in different positions placed on small cylindrical magnets with a diameter of 5 mm and a height of 5 mm. The flags are cylindrical aluminum rods with flattened tips. They extend into the coil on the aluminum BOSEM holder and reach with the tips in between the LED and the photodiode covering a part of the light sent from the LED. The flags are aligned in between LED and photodiode to half their maximum value of the photodiode. Any movement of the top mass is sensed due to a change of the amount of light that is hitting the photodiode and fed back to the
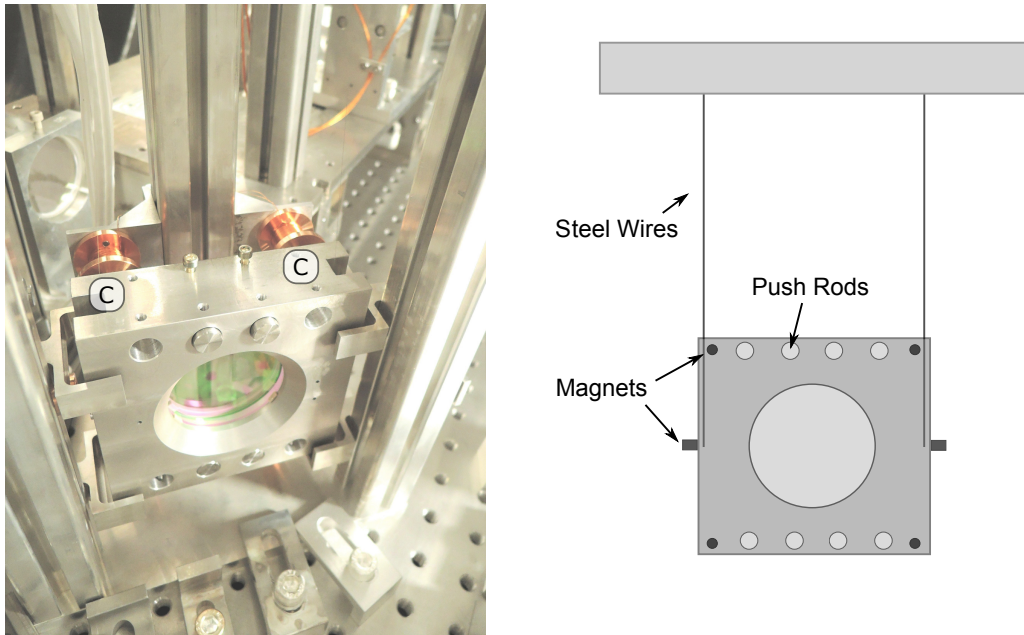
Figure 3.11: Suspended steering mirror for the frequency reference cavity. The two steering mirrors that couple the incoming beam to the frequency reference cavity are suspended as single pendulums. They are equipped with magnets at their back which reach into coils (C) mounted to the frame structure. This allows position control of the steering mirrors via CDS. The steering mirrors are also used for the auto-alignment scheme of the frequency reference cavity, further explained in 3.4.3.

coils. A variation of the current through the coils moves the suspension back to its original position. A view into the inside of a BOSEM with the flag centered between LED and PD is shown in figure 3.13.

The distribution of the BOSEMs on the top mass is shown in the photograph of figure 3.10. The three BOSEMs on the top of the top mass (A-C) control vertical motion as well as pitch and roll. Since the two pitch BOSEMs (B and C) are separated by 3.1 cm their lever arm is short resulting in a lower Signal-to-Noise Ratio (SNR) for sensing with these two BOSEMs compared to the others. The two BOSEMs on the front of the top mass (D and E, separated by 18 cm) control longitudinal motion as well as yaw motion. BOSEM F controls transversal motion of the suspension. Active control, e.g. damping of a suspension, depends on the specifications and characteristics of the sensors and actuators in the control loop. A limitation is often the noise floor of the sensor. In case of the frequency reference cavity suspensions, this defines the permissible noise of the BOSEM, which in turn consists of the noise of LEDs and PDs.

The BOSEM electronic noise requirements will be discussed in 4.1.1.

Further detailed information can be found in [Ast11].
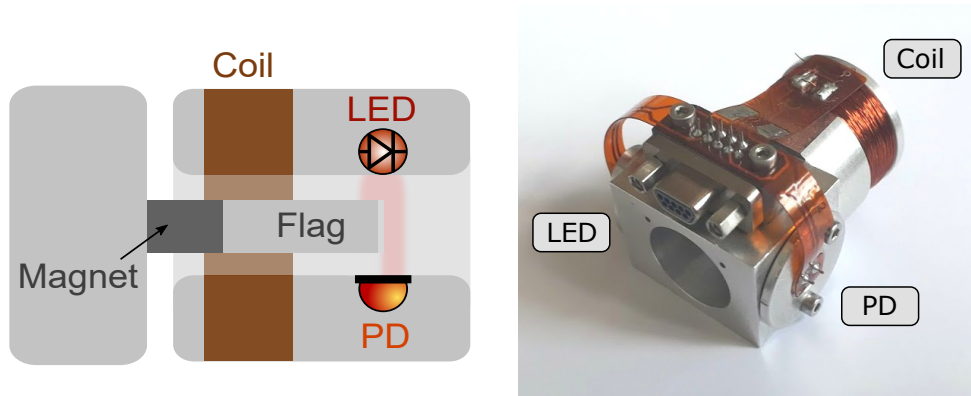
Figure 3.12: Schematic (left) and a photograph (right) of a BOSEM at the top mass of the frequency reference cavity suspensions for position readout and actuation.
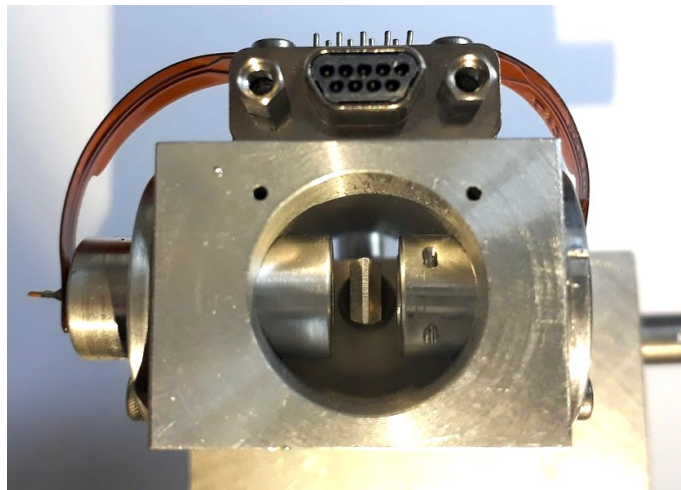
Figure 3.13: Photograph of the view into a BOSEM holder. The flag attached to cylindrical magnets sitting on the top mass is visible in the center of the aluminum holder. The LED is placed on the right shining the light through a lens and a slit onto the photodiode on the opposite side. This light is partly blocked by the flag in between. Top mass motion can be sensed in this way and controlled via the magnet-coil actuation.

3.3.4 Cavity Mirror Properties

The mirrors of the frequency reference cavity are made of Suprasil 2 Grade A, a low-mechanical loss fused silica material. Due to the triangular geometry of the frequency reference cavity it consists of two flat mirrors as input and output coupler and one curved mirror as the end mirror. Their properties are shown in figure 3.4. The curved mirror has a radius of curvature of 37.8 m and a transmissivity of approximately 4 ppm for p-polarized light. The input mirror has a transmissivity of 1000 ppm, while the output mirror transmits 600 ppm. The transmission values of the cavity mirrors differ from the original design values. Transmissivities of 500 ppm for the input mirror, 300 ppm for the output mirror and 10 ppm for the curved mirror were planned. The different values are due to the fact that the mirrors have been coated for unpolarized light. The initially planned use of s-polarized light for the frequency reference cavity was changed to p-polarization to avoid higher losses in the cavity. The initial design for the frequency reference cavity was planned to be impedance matched with the reflectivity of the input mirror almost equal to the round trip losses inside the cavity. In the impedance matched case no carrier light is reflected at the cavity and only the side bands at 8.047 MHz are reflected. This results in optimized shot noise, since there is no carrier light on the locking photodiode and only the side bands contribute to it. Changing the polarization of the cavity input light to p-polarization increased shot noise compared to the design configuration due to reduced finesse and the fact that it is further away from being impedance matched.

Triangular fused silica prisms are attached to the sides of all three mirrors. They were glued with UV light curing glue which provides high stability and also fulfills the requirements of vacuum compatibility. The steel wire slings that suspend the mirrors are placed on the prisms. They are not glued but stay in place due to friction on the mirrors. A photograph of the curved cavity mirror assembled in the vacuum system is shown in figure 3.14.

3.3.5 Triple Pendulum Assembly

The mirror and the intermediate mass had to be suspended in-situ in the vacuum system of the AEI 10 m Prototype since the suspension frame has no possibility to clamp the masses sufficiently for transportation. Due to the thicker and more robust wires of the intermediate stage, 100 μm instead of 55 μm for the lowest stage wires, and the better handling of the aluminum mass that is accessible from all sides, the intermediate masses can be suspended by hand. The lowest mass was suspended with a lifting platform with extended aluminum rods to hold the mirror and to place it inside the lowest wire slings.

The initial alignment of pitch and yaw to an accuracy of approximately 1 mrad was done during suspending the masses to offload actuation range from remote control. The orientation in pitch of the intermediate mass and the mirror can be changed by shifting the wire sling position on the masses. Fine tuning of pitch for the top mass and the intermediate mass is achieved by changing the position of the steel push rods inside the masses. Yaw
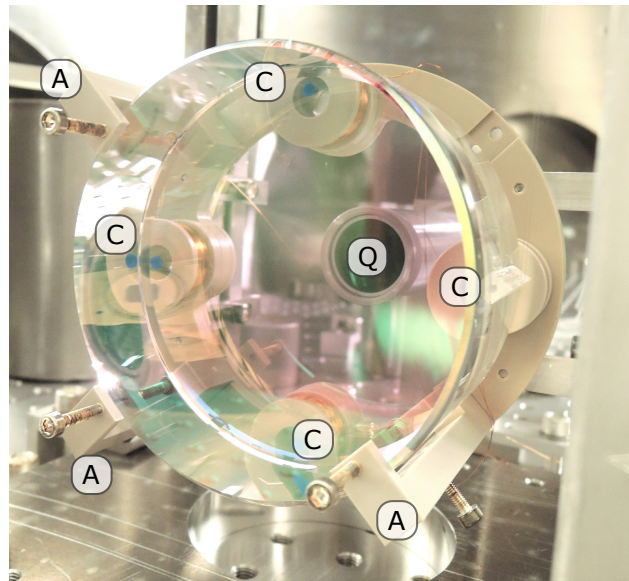
Figure 3.14: Photograph of the curved frequency reference cavity mirror on the south optical bench inside the vacuum system. It is suspended via 55 µm steel wires and surrounded by a safety clamping structure (A) that prevents the mirror from falling in case of wire failure. The coils (C) behind the mirror attached to the frame reaching into small magnets glued to the back side of the mirrors were designed to allow actuation onto the mirror in the longitudinal direction for compensating longterm drifts of the cavity. The aperture that is visible behind the mirror belongs to a spot position quadrant photodiode (Q) and can be used as reference position for initial alignment of the cavity.

alignment of the curved mirror is achieved by moving the complete suspension frame. The input and output mirror are suspended in one common frame structure which sets the relative angle between the two suspensions. Yaw alignment of these mirrors can be achieved by moving the top mass blade springs inside the top mass which in turn is not possible when the top mass is already installed. Roll for the intermediate mass and the mirror can be initially aligned during installation by hand. The top mass is also equipped with another push rod changing the roll position of the top mass. Longitudinal and transversal position can be set by the position of the suspension frame and the upper blades. Vertical position of the masses should be set well enough by producing the wires and slings with suitable jigs which set the right lengths. At the same time the required tension onto the wires during the production should be achieved by using weights according to the weight of the suspended masses. After installation the vertical position of the top mass and the other masses can be slightly changed by adding or removing weight at the top mass. Small ballast weights are initially installed and can be increased or removed.

3.3.6 Optical Layout of the Frequency Reference Cavity

The input beam to the frequency reference cavity is prepared outside of the vacuum system on a laser bench. The laser beam is launched from the fiber inside the vacuum system. Figure 3.15 shows the optical layout of the cavity including the input path. The frequency reference cavity uses a pick-off of the laser beam after the mode cleaner cavity while the main part is going to the sub-SQL interferometer. The input power to the frequency reference cavity is set to 266 mW and can be adjusted by a $\lambda/2$-wave plate and a polarizing beam splitter. An EOM is integrated for phase modulation of the light and provides sidebands at 8.047 MHz for the error signal. To adjust the mode of the incoming beam to the cavity mode three lenses are installed in the input path. Two suspended steering mirrors in front of the frequency reference cavity provide an aligned input path to the cavity.

The reflected light from the input mirror is guided out of the vacuum system by three high reflectivity mirrors through a viewport to the detection bench of the frequency reference cavity where the reflected cavity light is detected by the PDH locking photodiode and monitored by two quadrant photodiodes used for differential wave front sensing; see 3.4.3. In the same way the transmitted light of the cavity is sent out of vacuum to the detection bench and is detected with a photodiode. The layout of the detection bench is described in detail in 3.4.1.

EOM Commissioning

To create sidebands for the feedback loop, an EOM is placed in the input path of the frequency reference cavity providing sidebands at 8.047 MHz. The EOM crystal is made of Lithium Niobate (*LiNbO$_3$*). The initial EOM Radio Frequency (RF) matching electronic circuit and the EOM commissioning was done during this thesis at the Institute of Gravitational Research (IGR) of the University of Glasgow.

The matching circuit resonantly enhances the phase modulation and provides impedance matching to maximize the RF power delivered to the EOM and minimized RF reflections on the cable.

Before a vacuum-compatible set-up of an EOM including RF adaptation electronics was available, a non-vacuum compatible setup was selected as an intermediate solution. The non-vacuum compatible components of the RF adaptation electronics were placed in a vacuum can which is equipped with a feed through for cables and allows a connection to the EOM. Figure 3.16 shows a photograph of the EOM and the vacuum can. In order to keep the wire lengths short the can is placed next to the EOM on the central optical table. A 15 cm long twisted pair cable connects the EOM and the vacuum can through a cable feed through. The RF matching circuit inside the vacuum can consists of a coil with inductance L, a 22 kΩ resistor, a trim capacitor and two fixed 200 pF capacitors in parallel. The trim capacitor can be used for adjustment to achieve the correct resonance frequency. The resonance frequency can be calculated by $\Omega^2 = L \cdot C$ with $\Omega = 2 \cdot \pi \cdot f$.

The circuit is connected via a 3 m long coaxial cable to a vacuum feedthrough of the AEI
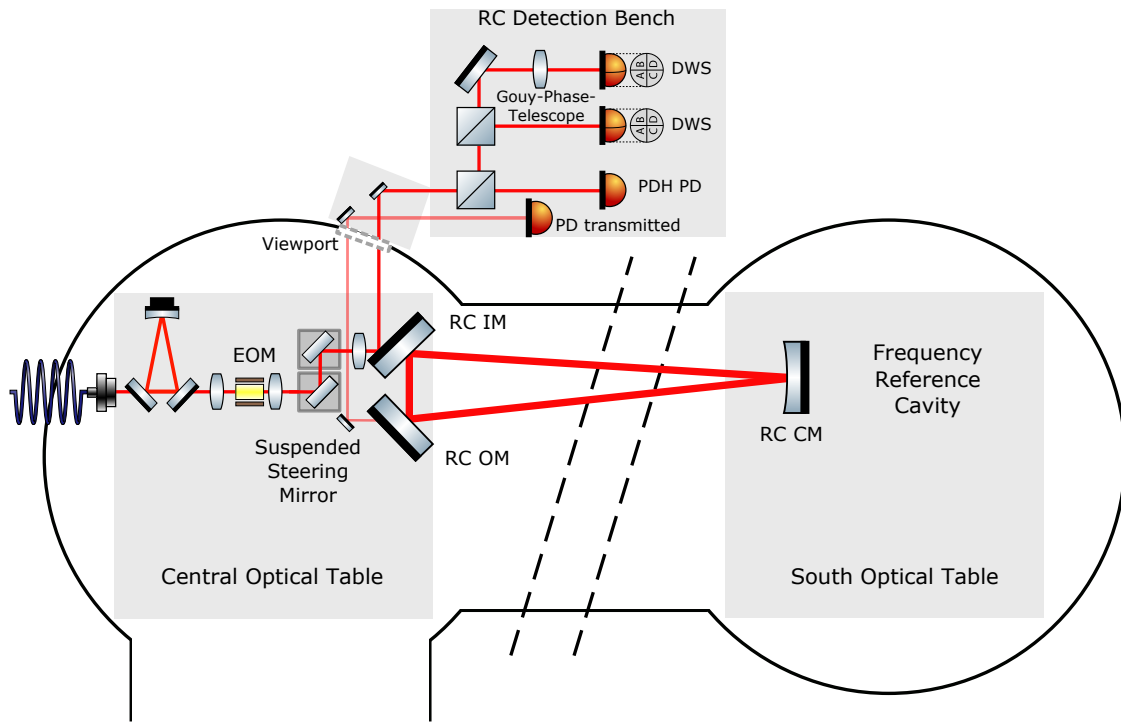
Figure 3.15: Optical layout of the frequency reference cavity in the vacuum system. The laser light is fiber coupled into the central optical table of the vacuum system. After passing the mode cleaner cavity and an EOM 266 mW of the light is split-off for the frequency reference cavity while the main part goes to the sub-SQL interferometer. In front of the frequency reference cavity two suspended steering mirrors ensure the alignment to the cavity. The frequency reference cavity itself is a triangular cavity set-up across the two in-vacuum optical tables with two flat mirrors placed on the central optical bench and the curved mirror (RC CM) located at the south optical table. The reflected light of the cavity input mirror (RC IM) and the transmitted light through the output mirror (RC OM) is sent out of the vacuum system through a viewport. On the detection bench both the reflected and transmitted light is detected by several photodiodes.

10 m Prototype tank. Outside of the vacuum system a self-built amplifier provided by the University of Glasgow increases the signal from the local oscillator to the modulator to 1 W. To be able to apply a voltage to the EOM crystal it is embedded in a pair of gold plated electrodes and mounted on a MACOR® plate. MACOR® is a machinable vacuum compatible glass ceramic with low thermal conductivity. Since a mounting unit from GEO 600 was used as a holder which was designed for two EOMs a second plate of electrodes is still assembled but not used for the AEI 10 m Prototype.

Figure 3.17 shows the EOM set-up including the RF matching circuit in the AEI 10 m Prototype vacuum system.

The implementation of an EOM with a vacuum compatible matching circuit to avoid the additional weight of the vacuum can on the central optical bench is under investigation as of the time of writing.

The modulation depth of the $LiNbO_3$ crystal was measured in a test setup with a scanning Fabry-Perot cavity as a spectrum analyzer. The signal from the Fabry-Perot cavity was monitored with an oscilloscope. The results with and without RF modulation are shown in figure 3.18 for an RF input power of 1 W.

The modulation index MI is calculated by

$$MI = 2 \cdot \frac{\sqrt{U_{SB}}}{\sqrt{U_{Carrier}}}.$$

This results in an modulation index of $MI = 0.47$ with $U_{Carrier} = 3.21\,\text{V}$ and $U_{SB} = 0.18\,\text{V}$ for an RF input power of 1 W.

Laser Input Beam Preparation

Incoming laser light to an optical cavity needs to be adjusted in terms of the mode profile such that it matches the eigenmode of the cavity, based on its geometry. This is known as mode-matching and is required to maximize the coupling of light into the resonant cavity mode. Laser light can couple into a cavity when an integer number of laser wavelengths is equal to twice the cavity length. The constellation of lenses and their positions in the input path of the frequency reference cavity were modeled with JAMMT (Just Another
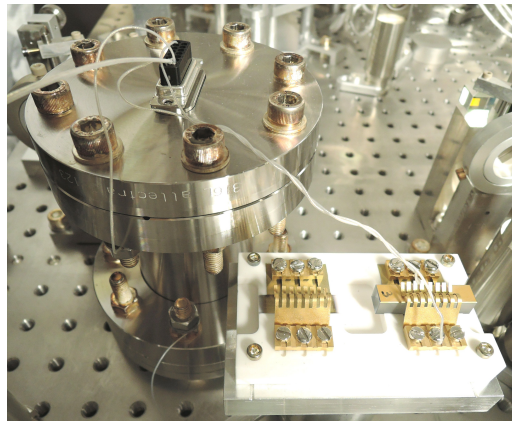
Figure 3.16: EOM in the frequency reference cavity input path. The crystal is a $LiNbO_3$ crystal with a front surface of 8 mm x 8 mm and a length of 40 mm. It is embedded in a pair of electrodes and mounted on a MACOR® mounting unit which was originally implemented in GEO 600 and was used for two EOMs in series. The vacuum can next to the EOM encloses a non-vacuum-compatible circuit board connected via a feedthrough for the cabling to the EOM and to the amplifier outside of the AEI 10 m Prototype vacuum system.
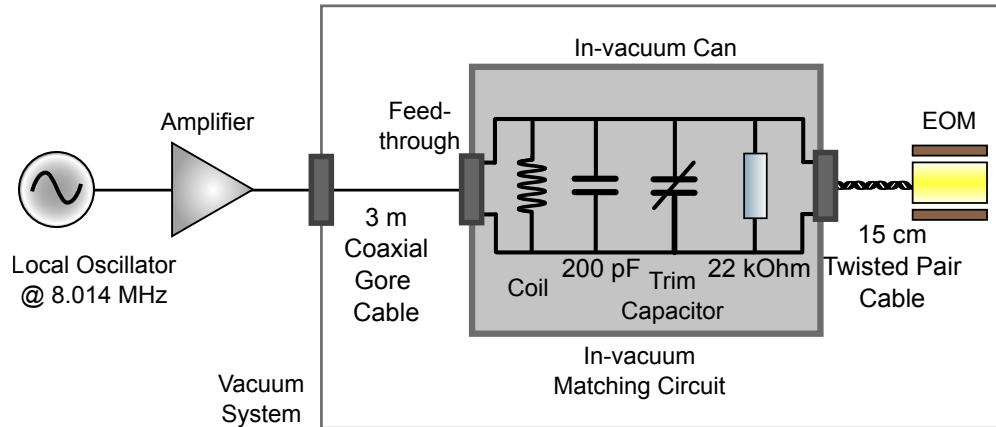
Figure 3.17: Schematic layout of the in-vacuum EOM for the frequency reference cavity control loop. The signal comes from the local oscillator, gets amplified and is fed into the vacuum system via a cable feed through. The matching circuit for the EOM is placed on the optical table next to the EOM. It consist of a coil, a capacitor, a trim capacitor and a resistor in parallel. It was adjusted before installation such that the reflected RF signal from the circuit was minimized.
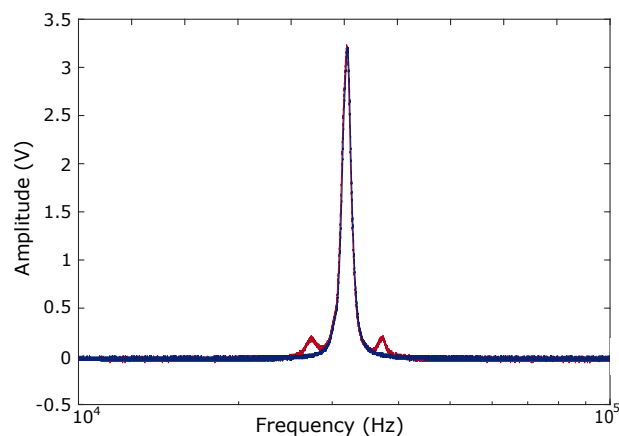
Figure 3.18: Measurement to determine the modulation depth of the *LiNbO*$_3$ crystal with RF modulation (red) and without RF modulation (blue) as a reference. The modulation index is 0.47 for an RF input power of 1 W.

Mode Matching Tool). Given the waist behind the mode cleaner and the spot size on the frequency reference cavity input mirror, a solution with three lenses was found with focal lengths of 300 mm, 100 mm and 500 mm. A schematic overview is shown in figure 3.19. A Gouy phase difference of 90° between the two steering mirrors is desired to ensure that both steering mirrors control independent degrees of freedom. In the existing set-up the beam impinging on the first steering mirror has an accumulated Gouy phase of −10.7° while the beam on the second steering mirror has a Gouy phase of −87.8°. In this constellation the beam waist sits on one steering mirror. Due to the steep slope of the Gouy phase at the beam waist this steering mirror is sensitive to its position; therefore, misalignments of the steering mirror during installation result in a significant variation of the Gouy phase.

3.3.7 Alignment

The initial alignment of the cavity is realized manually, as the range of the remote control drive is limited. The linear alignment range of the BOSEMs is approximately 500 μm before they show a non-linear behavior [Ast11]. The cavity alignment across the two in-vacuum optical tables requires them in a well-known reference position with all stabilization control loops running. Remote cavity control is required when the vacuum system is pumped.

Manual Alignment

The manual alignment of the complete suspension and in particular of the top mass was described in 3.3.5. This section focuses on the manual alignment of the optical input path to the cavity and of the cavity itself.
The input beam needs to be centered on all optical components in the input path, especially on lenses to avoid beam shape distortion. Steering mirrors allow the alignment onto the EOM, lenses and suspended steering mirrors and the cavity mirrors. On the input mirror of the cavity, the beam is aligned such that it is centered on the surface facing the inside of the cavity.
The initial manual alignment of the suspensions is realized during installation. More tuning can be achieved by moving suspension frames or using push rods inside the top mass, the intermediate mass or at the suspended steering mirrors. This manual alignment of the input beam and the input mirror suspension is able to get the beam aligned up to a few centimeters on the south optical table. Before the alignment of the beam inside the cavity, the central optical table and the south optical table need to be in the optimal reference position to each other.
The alignment of the cavity is a stepwise approach. The first suspended steering mirror before the cavity centers the beam onto the second steering mirror which in turn is used to guide the beam through the cavity input mirror and center the spot onto the curved mirror on the south optical bench. The reflected beam from the curved mirror is sent to the cavity

Steering mirror 1 · Steering mirror 2 · RC input mirror · Lens 1 f = 300 mm · Lens 2 f = 100 mm · Lens 3 f = 500 mm · Mode Cleaner Waist · EOM

w = 386 µm
z = 0 m

z = 0.541 m

w = 750 µm
z = 0.767 m
φ = 0 deg

w = 625 µm
z = 1.516 m
φ = 0 deg

w = 2375 µm
z = 2.188 m

w = 2355 µm
z = 2.37 m

z = 1.663 m   z = 2.087 m
φ = -10.72 deg   φ = -87.762 deg
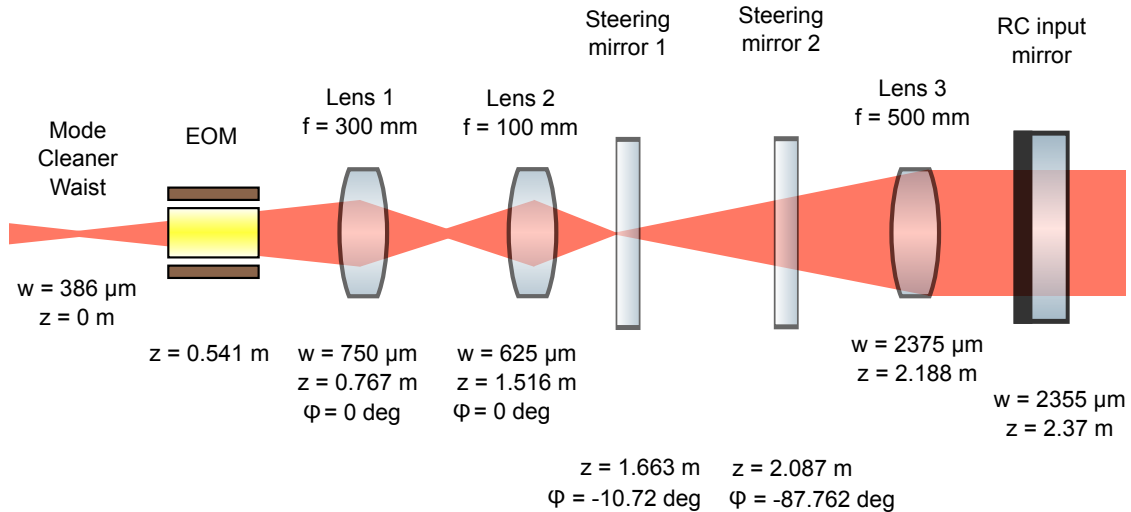
Figure 3.19: Mode matching into the frequency reference cavity. Three lenses are used to get the desired spot sizes and Gouy phases on the optical components. A Gouy phase difference of 90° is desired on the two steering mirrors in order to guarantee a maximum actuation range. Parameter like the distance from the mode cleaner cavity waist z, the beam waist w and the Gouy phase ϕ are given for the different components. The laser beam is shown in red.

output mirror which aligns its reflected beam to the input mirror.

Careful manual alignment of all mirrors can already lead to visible laser round trips inside the cavity which can be viewed with an infrared viewer card. For a more accurate alignment, fine tuning needs to be done with the actuators at the suspensions and steering mirrors.

Remote Alignment

If the cavity is manually coarse aligned such that several laser round trips inside the cavity separated by some centimeters are visible, further electronic fine alignment is necessary. Due to the long lever arm of more than 10 m the alignment is sensitive and manual tuning is limited. Via CDS the cavity suspensions can be remotely controlled with the BOSEMs at the top mass. In addition, the two suspended steering mirrors in front of the cavity can be tuned remotely by actuating onto their magnet-coil actuators. In comparison to the cavity suspensions, the steering mirrors have no position readout at the mirrors themselves. Spot position QPDs behind the second steering mirror and behind every cavity mirror give information about the beam displacement and allow spot monitoring on the mirrors even when the vacuum system is pumped and not accessible. This is limited behind the curved frequency reference cavity mirror which transmits approximately 4 ppm and therefore

some picowatts of light are incident on the QPD. Due to the weak signal in comparison to stray light from in-vacuum propagating laser beams this method is not always reliable and requires a high level of interpretation to use. An overview about where the spot position QPDs for the frequency reference cavity are located is shown in figure 3.20. Like the coarse manual adjustment the CDS remote alignment is a stepwise approach starting from the first steering mirror on which centers the beam onto the second one which in turn is used to align the beam through the input mirror onto the curved south cavity mirror. This and the output mirror allow the alignment inside the cavity while the latter also sets the transmitted beam path that is guided out of the vacuum system to the detection bench.

The input mirror of the cavity also defines the path of the reflected beam on the detection bench outside vacuum. The DC power on two quadrant photodiodes used for the differential wavefront sensing can serve as spot position sensors in this case and can be used as reference position for future re-alignments. Likewise, the locking photodiode in the reflected path as well as the photodiode in transmission of the cavity indicate the alignment.

Two CCD cameras in both the reflected and transmitted beam path are set up to observe beam shape and position. Especially during the initial alignment phase they were used to gain information about the status of the cavity showing flashes or later on the modes to which the cavity was locked.

After misalignments or drifts of the cavity mirrors the re-establishment of the BOSEM values can re-gain alignment. The top mass can be automatically controlled to a user determined position via BOSEMs. Using automatically stored data via CDS, the suspensions can be set to the last known well-aligned configuration.

A safety mechanism is implemented into CDS to automatically switch off the feedback from the BOSEM coils in case of excessive table motion to avoid the feedback loop exciting unwanted movement.

The aim of the initial alignment is to get the cavity in a condition such that it can be locked. Therefore, the majority of flashes of the transmitted light need to be in the fundamental transverse electromagnetic mode TEM_{00}.
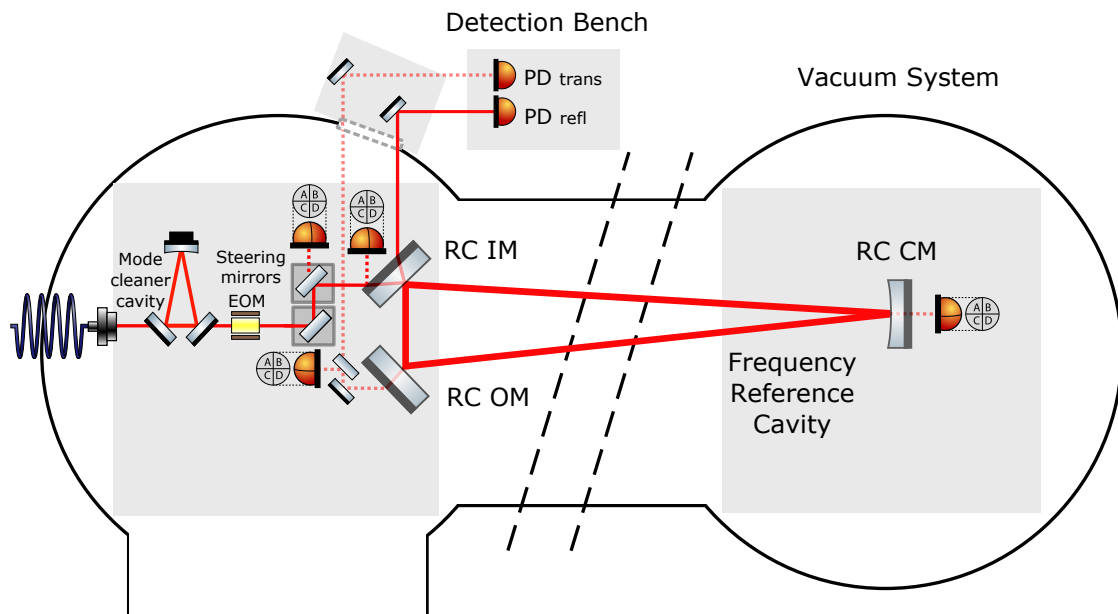
Figure 3.20: Overview about the spot position QPDs for the frequency reference cavity. They are located behind the second suspended steering in transmission and next to every frequency reference cavity mirror. At the input mirror the directly reflected light is detected whereas the transmitted light through the curved mirror and the output mirror is detected. The spot position QPDs can be used for alignment purposes and to detect angular beam misalignments at DC.

3.4 Stabilization of the Frequency Reference Cavity

3.4.1 Optical Layout of the Detection System

The frequency reference cavity readout is completely performed outside of the vacuum system. The reflected and transmitted beams of the frequency reference cavity are sent with steering mirrors out of the vacuum system through an infrared transmissive view port. At this view port a small optical bench is mounted to the vacuum flange equipped with two additional steering mirrors in order to guide the beams to the detection bench.

Figure 3.21 shows a sketch of the detection bench layout. The reflected beam from the frequency reference cavity starting from the lower right side is shown in red. It is sent to a periscope on the detection bench consisting of two mirrors to bring the beam down to the desired beam height of 10 cm above the table top.

An attenuation unit consisting of a $\lambda/2$-wave plate and a polarizing beam splitter allows an adjustment of the light power on the detection bench independent from the reflected power from the cavity. A beam dump blocks the residual power.

Three lenses (L1, L2 and L3) are installed for the Gouy phase telescope necessary for the differential wave front sensing which is explained in section 3.4.3.

The reflected path is split into two beams by a 50:50 beam splitter. Each beam is sent to a quadrant RF photodiode, implemented for the differential wave front sensing.

The split-off beam with the shorter lever arm uses another small pick-off of 10 % to monitor the beam on a CCD camera. A neutral density filter in front of the camera avoids saturation of the CCD chip. The residual 90 % of the beam is guided to the first Wave Front Sensor (WFS). In front of WFS1, two Galvo motors equipped with one mirror each keep the beam centered on the quadrant photodiode by controlling pitch and yaw motion of the beam. This is further explained in 3.4.3.

The second 50 % path of the reflected cavity beam is sent to the second WFS. Two Galvo motors keep the beam centered on WFS2 and on the PDH locking photodiode which is placed after a 90:10 beam splitter. In front of the locking photodiode an attenuation unit consisting of a $\lambda/2$-wave plate and a polarizing beam splitter give the possibility to control the incident light power on the photodiode in order to reduce the laser power in the initial alignment and commissioning phase on the photodiode. The power will be increased when an optimal shot noise performance is required. A lens (L5) with a focal length of 50 mm is used to image the beam onto the photodiode.

The transmitted cavity beam is also sent to the detection bench and brought to a beam height of 10 cm by a periscope. A lens (L4) with a focal length of 450 mm images the beam onto the photodiode in transmission and on another CCD camera.

3.4.2 Frequency Reference Cavity Feedback Control Loop

A feedback control loop in general consists of a plant with a certain parameter that needs to be controlled, a sensor, a servo and an actuator. Noise or longterm drifts keep the plant output away from the desired value and make a control of the output necessary. A sensor detects the current output of the plant and compares it to a reference which sets the desired value for the plant parameter. The difference between the current output and the reference value gives the error signal. This signal is sent to a servo to generate a feedback signal which is sent to an actuator. The actuator changes the current value of the plant to the desired value given by the reference. Since the signal is fed back to the plant to compensate the measured error signal this scheme is called a negative feedback control loop. Careful design of a control loop is needed to avoid instability. This would result in positive feedback where deviations arising from noise get amplified and grow exponentially.

Detailed information about feedback control systems can be found in [Abr12].

A layout of the control loop for the laser frequency stabilization is shown in figure 3.22. The plant output that has to be controlled is the laser frequency. The reference for the desired frequency stability is the length of the frequency reference cavity. The error signal, given by the difference between the current laser frequency and the reference set by the cavity, is detected by a photo detector. This signal is sent to the Table-Top Frequency Stabilization Servo (TTFSS) where it is filtered and amplified and sent to the actuators. The
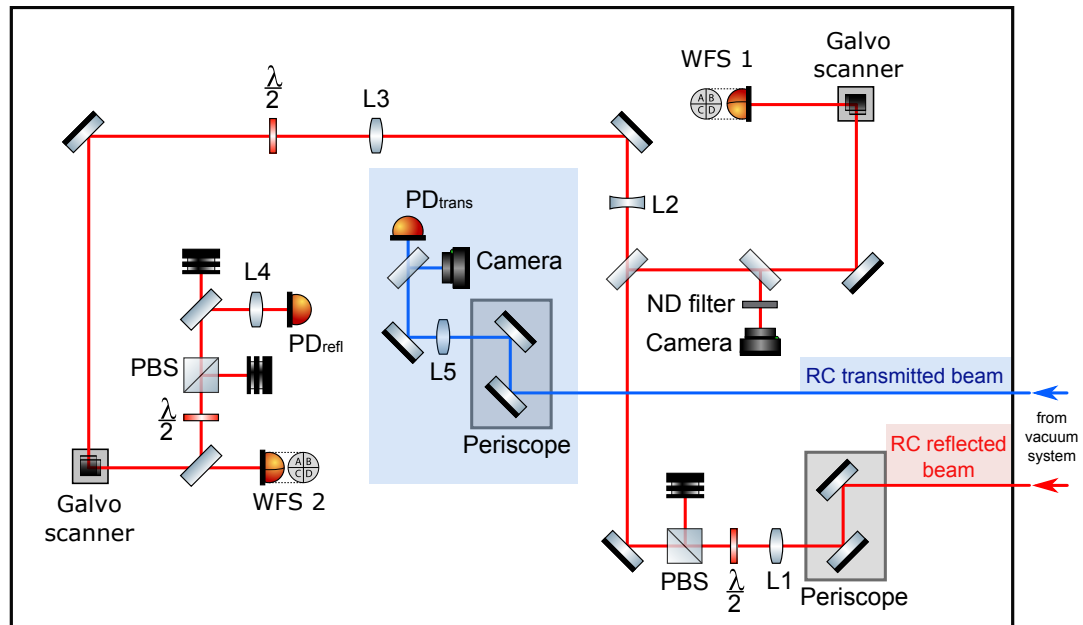
Figure 3.21: Sketch of the frequency reference cavity detection bench. Both the reflected and transmitted beam of the cavity leave the vacuum system via an infrared transmissive view port. The reflected path, shown in red, passes a lens (L1) with a focal length of 750 mm. With a lambda half wave plate and a polarizing beam splitter in front the power of the beam can be adjusted. Additional unused power is sent to a beam dump. The reflected beam is split up with an AR window into two paths. One passes a beam splitter where a small fraction is picked up and directed to a neutral density filter for power attenuation and onto a CCD camera. The main part of the beam goes to a Galvo scanner, consisting of two mirrors that can be steered, that adjusts the beam spot on WFS1 and keeps the beam centered. The other part of the reflected beam passes two other lenses with -75 mm (L2) and 200 mm (L3) focal lengths. The three lenses (L1, L2 and L3) form the Gouy phase telescope for the auto-alignment. Another Galvo scanner in this beam path keeps the beam spot centered on WFS2. A pick-off of that beam is directed to the photodiode in reflection PD_{refl}. Before the photodiode another power attenuation stage is implemented with a lambda half wave plate and a polarizing beam splitter. A lens (L4) focuses the beam onto a photodiode. The transmitted beam of the frequency reference cavity, shown in blue, is focused by a lens (L5) with a focal length of 450 mm onto a photodiode and another CCD camera.

frequency reference cavity control loop uses three different actuators in order to provide a high control bandwidth.

The complete control topology for the laser frequency stabilization is shown in figure 3.23. Individual parts of the control loop will be discussed in the following.

PDH Locking Photodiode

The effectiveness of the laser frequency noise suppression depends on the loop gain of the control loop as well as on the sensitivity of the sensor. In the frequency reference cavity feedback control loop, a photodiode is used as sensor as shown in figure 3.22, realized in a bachelor thesis project [Pla17].

A 3 mm InGaAs photodiode from Epigap, model number EOPD-1300-3.0, is used for the frequency reference cavity locking. The photodiode including electronics are shot noise limited between 1 mW and 28 mW. This is the fundamental limit of a servo loop performance and limits standard PDH sensing. The upper limit of 28 mW results from current limiting electronics, described in this section.

The electronics are optimized for the modulation frequency of 8.074 MHz. In case that the frequency reference cavity is not locked, all incoming light is reflected at the input mirror. In lock, the reflected light is less than 10 % of the incoming light when the cavity is stabilized due to the cavity being close to impedance matched. This sets requirements for the photodiode that needs to be sensitive enough when a small fraction of the power is arriving but should survive the higher power that can possibly hit the photodiode every time when the cavity loses lock.

The planned input power of the frequency reference cavity is 266 mW. As of the time of writing, the full laser power has not yet been used. The reflected power from the unlocked frequency reference cavity is approximately 110 mW. Due to the power distribution on the detection bench with two power attenuation units consisting of a $\lambda/2$-wave plate and a PBS, approximately 10 mW is impinging on the locking photodiode. Solutions for the future, when more laser power is used and incident on the locking photodiode, have been investigated and discussed. The amount of power dumped on a photodiode is converted into heat and would destroy the photodiode.

A photodiode with built-in security mechanisms was implemented in the frequency reference cavity path. Three different methods are used to prevent damage of the photodiode due to high light power exposure. They will be discussed in the following.

A design with a mechanical shutter in front of the photodiode was proposed and investigated. This shutter closes when the cavity falls out of lock and prevents the incoming light impinging onto the photodiode. This shutter is a commercially available shutter from Thorlabs, model SHB1T. It is remotely controllable via CDS where it also gets the signal that the cavity lost lock. The shutter has a delay between the arrival time of the signal and its actual closing time. This was measured to be 22.2 ms which lies even below
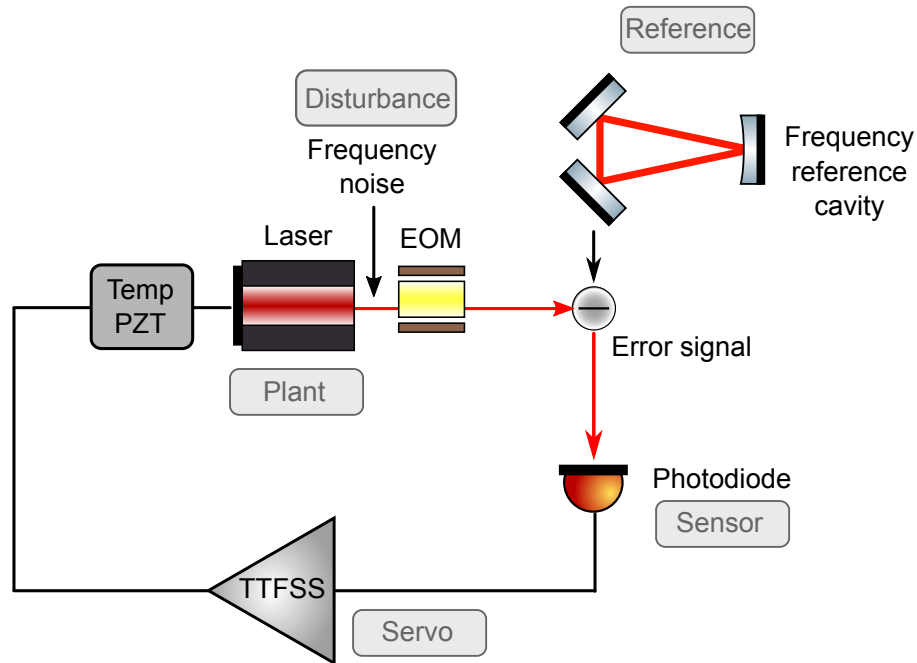
Figure 3.22: Feedback control loop of the frequency reference cavity. Optical laser light is shown in red while electronic signals are represented by black lines. The plant is depicted by the laser source with the laser frequency as controllable plant output. The desired stability of the laser frequency is provided by the frequency reference cavity. The error signal is detected by a locking photodiode and sent to the Table-Top Frequency Stabilization Servo. From there is goes to the three actuators that provide a frequency dependent actuation onto the laser. They are realized by a temperature loop, a PZT and an EOM placed in front of the laser.

the provided value from the manufacturer. Due to a delay of the switching mechanisms in combination with this shutter closing time the photodiode is exposed for 25.7 ms to the complete input power of the cavity. This time is covered by two additional safety mechanisms.

One of them is a passive heat sink that is installed underneath the photodiode. This is realized with a copper cylinder that is attached to the circuit board for heat dissipation.

To protect the photodiode from additional heat load by the bias voltage and the photo current, a current limiter is included into the electronic circuit board design. This is realized with a combination of two Positive-Negative-Positive transition (PNP) transistors and two resistors. The dissipated power comes from the optical part while the electronic component is minimized and the photodiode is protected from large photo currents.
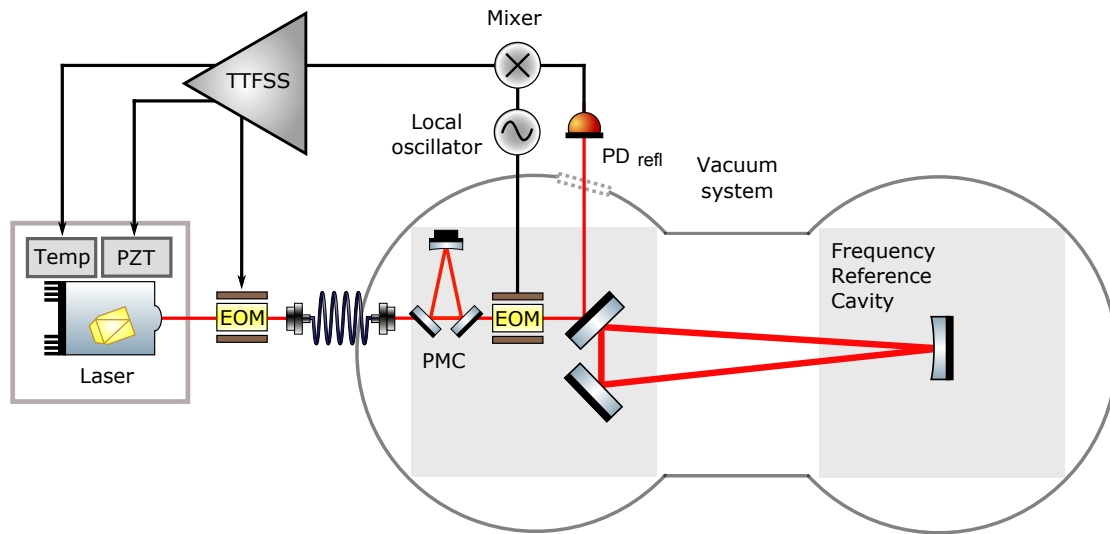
Figure 3.23: Sketch of the control topology for the frequency reference cavity at the AEI 10 m Prototype. A PDH sensing scheme in reflection is used as feedback control loop. The laser light is fiber-coupled into the vacuum system. After passing the mode cleaner cavity an in-vacuum EOM phase modulates the light in the frequency reference cavity input path. A local oscillator provides the 8.074 MHz signal for the EOM. The reflected light of the frequency reference cavity is detected by a photodiode outside the vacuum system. This signal together with the local oscillator signal is mixed and sent to the TTFSS. There, the signal is divided into three different paths, namely the temperature path, the fast (PZT) path and the EOM path. The demodulation of the photodiode signal is also done inside the TTFSS. After processing of the signals they are fed back to the three laser actuators, temperature, PZT and EOM.

Figure 3.24 shows this current limiting electronic circuit. A PNP transistor allows the current to flow from the emitter to the collector if the base potential is 0.7 V lower than the emitter potential. 0.7 V is the diode forward voltage drop of a silicon diode. The emitter-base potential is given by $I \cdot R$ with the current I and the resistance R, in case of transistor T_1 this potential relation is given by $I \cdot R_1$. For low currents, T_1 is closed since the voltage drop across R_1 is less than 0.7 V. The base of T_2 is connected via R_2 to ground and current can flow to T_2.

For high currents, the voltage drop across R_1 exceeds 0.7 V and T_1 opens. The base B_2 of T_2 is no longer grounded and T_2 starts to become closed. The current flowing through R_1 is restricted such that the voltage drop is less than 0.7 V. In conclusion, the current limit is set to 0.7 V/R_1.

The circuit board schematics for the locking photodiode are included in the appendix B.1. Figure 3.25 shows the current (blue lines) and the bias voltage (red lines) in dependence
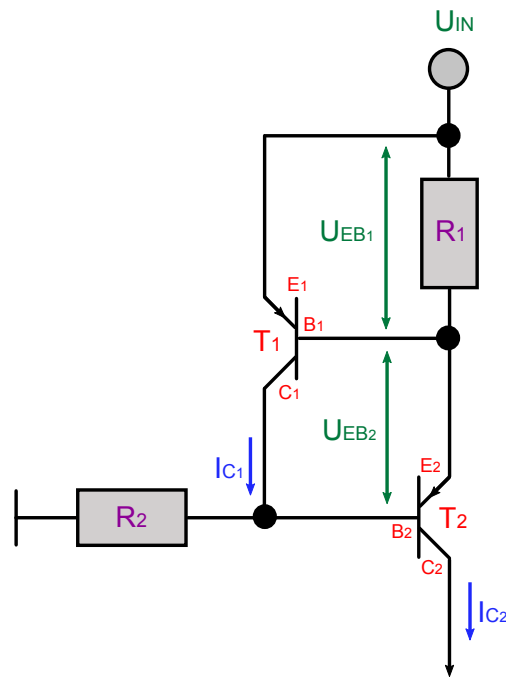
Figure 3.24: Circuit of the current limiter in the frequency reference cavity locking photodiode. For low currents, the voltage drop across R_1 is less than 0.7 V and T_1 closes. Due to some bias voltage of more than 0.7 V, T_2 is open and current can flow to the photodiode. The base of T_2 is connected via R_2 to ground. For high currents, T_1 opens and T_2 becomes closed since the base of T_2 is no longer at ground potential. The current limit is set to 0.7 V divided by R_1.

on the optical laser power for different resistors 16 Ω, 30 Ω and 62 Ω. The current initially increases linearly. The current limitation starts at different powers, depending on the selected resistors. At higher resistances the current limitation starts earlier at lower laser powers.

Figure 3.26 shows the shot noise of the AC path of the PDH locking photodiode for different optical powers. The Amplitude Spectral Density (ASD) in a frequency range around the modulation frequency of 8.074 MHz is shown. For the indicated optical powers between 1 mW and 28 mW the photodiode is limited by shot noise at 8.074 MHz. The measurement and the simulation is consistent for optical powers of 1 mW, 8 mW and 16 mW. For a power of 28 mW the measured value is above the theory, since the current limitation in this range has already reached the set limit.
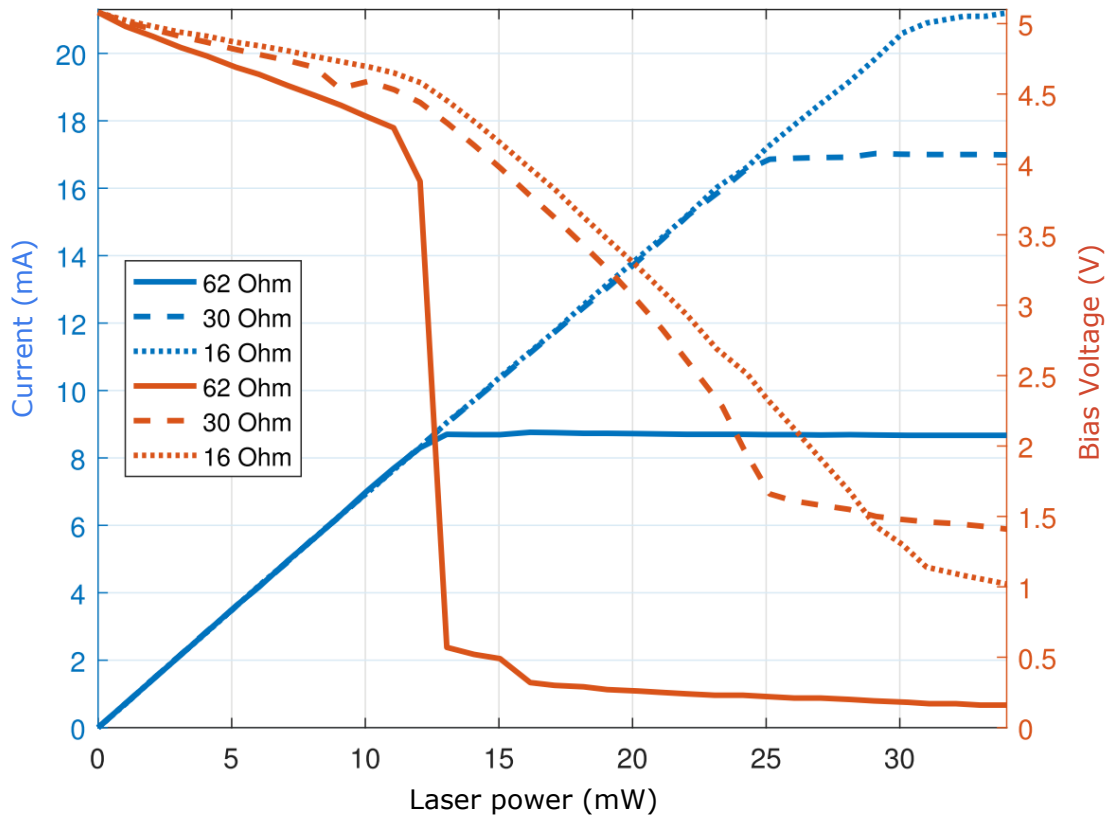
Figure 3.25: Current and bias voltage in dependence on the optical laser power for different resistors. The current limitation starts at different powers, depending on the selected resistors.

Table Top Frequency Stabilization Servo

The servo in a control loop provides a filtering and amplification of the error signal. This signal is sent to the actuators to control the plant's output. For the frequency reference cavity control loop a modified version of the Table Top Frequency Stabilization Servo (TTFSS) from aLIGO is used. The design was changed according to the purposes and specifications of the AEI 10 m Prototype system. Three additional daughter boards are installed. The purpose of these are to provide a boost for the low frequency gain and to compensate for the cavity poles of the frequency reference cavity and the mode cleaner cavity.

The TTFSS is placed on the optical table next to the laser source in order to keep cable lengths short since the phase delay from several meter long cables would be significant. Figure 3.27 shows a block diagram of the TTFSS. It has a complex design including multiple circuit boards. Input signals from the local oscillator and the locking photodiode
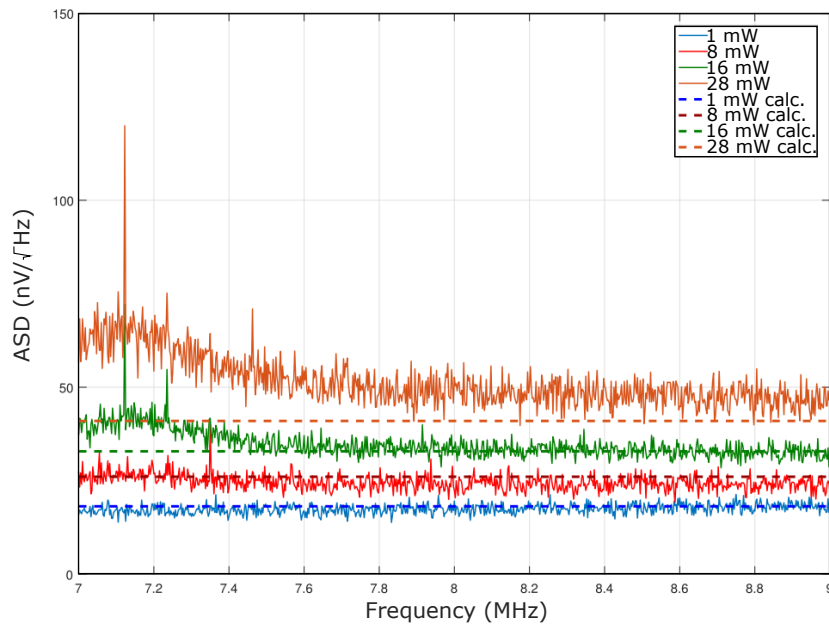
Figure 3.26: Shot noise of the PDH locking photodiode AC path for different optical powers. The modulation frequency of the frequency reference cavity is 8.074 Hz.

are passing the first RF board. The demodulation of the locking photodiode is provided here.

An additional input is added to apply a test signal into the TTFSS which can be controlled with a switch on the RF board. The possibility of applying an analogue offset is given by an additional input.

In the common path a variable gain amplifier allows the adjustment of the common gain. A daughter board attached to the common path circuit board is installed to compensate for the frequency reference cavity pole at 3.97 kHz.

After the common board the signal is split into the paths to the different actuators, described in the next section, the fast path and the EOM path. The fast path is added to increase the actuation bandwidth and to cover the mid-frequency range. The low-frequency actuation range of the piezo-electric transducer of the fast path is offloaded to a slow temperature controlled path. The temperature path is picked off from the fast path and is processed digitally in CDS.

Before the splitting in the EOM path another daughter board is attached to the circuit to compensate for the mode cleaner cavity pole at 300 kHz.

Actuators

The frequency reference cavity control loop uses multiple actuators, as mentioned in the previous section, to cover a frequency range of approximately 300 kHz. The frequency
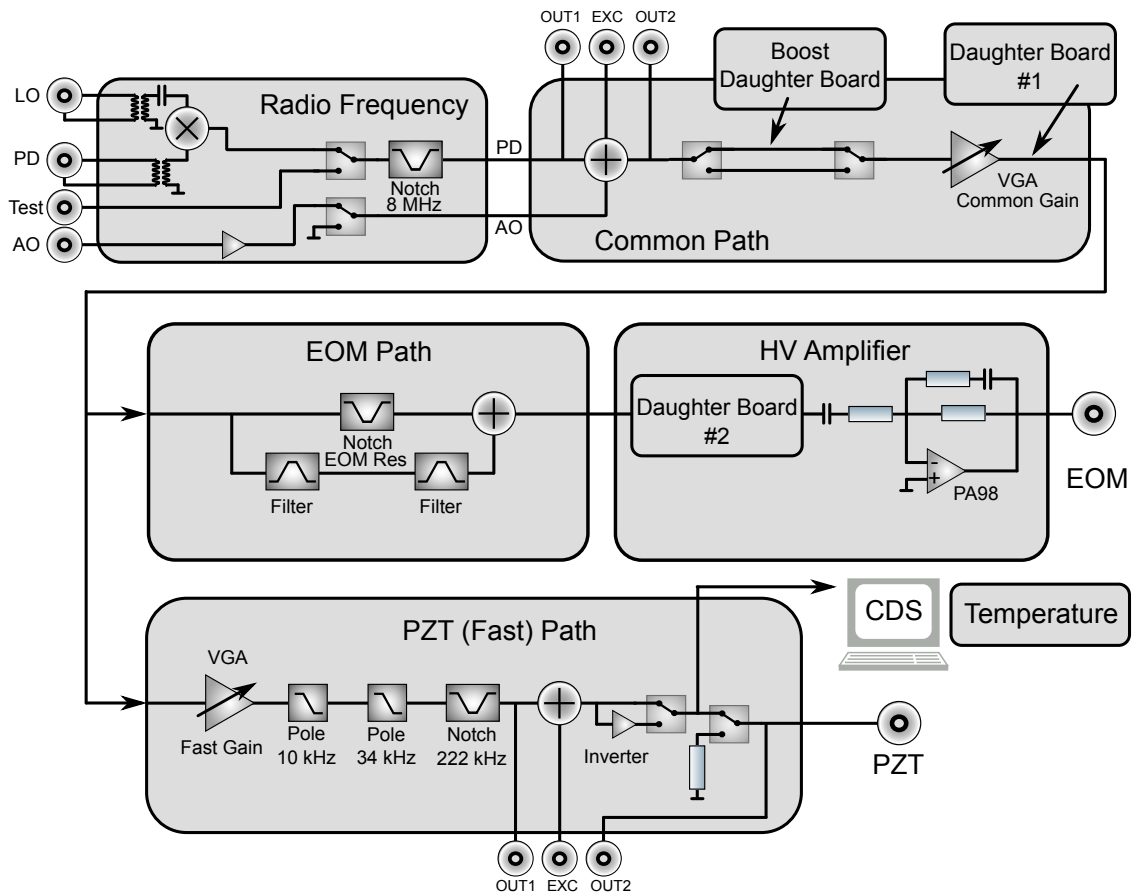
Figure 3.27: Simplified block diagram of the TTFSS layout. The demodulation of the locking photodiode signal is done on the radio frequency board inside the TTFSS. After a common path the signal is split into different paths for the three laser actuators, the EOM path for high frequencies, the fast path for the mid-frequency regime. The slow temperature path for low frequencies is processed digitally in CDS.

dependent, amplified signal is sent from the servo to three actuators, which actuate on the laser.

For slow control below 1 Hz the system is temperature controlled, realized by a peltier element placed underneath the NPRO crystal. A change of the temperature in the crystal causes both a thermo elastic effect and a thermo refractive effect. The first is a change of the crystal length while the latter is a modification of the refractive index. Both are resulting in a change of the optical path length of the laser light passing the crystal which in turn results in a phase change and hence in a change of the laser frequency.

For higher frequency actuation onto the laser a piezo-electric transducer is installed in the

laser, applying pressure to the crystal such that the refractive index of the material changes. This results in an optical path length change and in a frequency change. This method is used for frequencies between 1 Hz and 10 kHz. Due to internal mechanical resonances in the material higher frequencies can not be controlled by the piezo-electric transducer. The actuation coefficient is $1.35 \, \text{MHz}/V$.

For frequencies higher than 10 kHz an EOM is used. It is installed in front of the laser on the optical bench outside the vacuum system. It consists of a *LiNbO$_3$* crystal which is embedded between a pair of gold plated electrodes. If a voltage is applied to these electrodes an electric field is generated which changes the material structure and modulates the refractive index of the crystal. The optical path length of the laser light through the crystal changes resulting in a phase change of the exiting laser light.

Open Loop Gain of the Frequency Reference Cavity

The efficiency of the frequency stabilization is indicated by the loop gain of the complete feedback control system of the frequency reference cavity. For measuring the Open Loop Gain (OLG), the TTFSS is equipped with several test points as shown in figure 3.27. The OLG of the locked cavity is shown in figure 3.28. The control loop of the frequency reference cavity was measured including the loops of the different laser actuators PZT and EOM. Several measurements for different frequency ranges were recorded and then combined. They are shown in blue. A modeled OLG is represented by the dotted black line. The simulated OLG at 100 Hz is 125 dB. The measured OLG is with approximately 110 dB below the estimate. As mentioned in the beginning of this chapter, the requirements in laser frequency noise suppression are $10^{-4} \, \text{Hz}/\sqrt{\text{Hz}}$ at 20 Hz decreasing to $10^{-6} \, \text{Hz}/\sqrt{\text{Hz}}$ at 1 kHz [Kaw10]. This corresponds to 140 dB at 100 Hz. In summary, the final frequency noise suppression is not yet been reached.

Frequency Stabilization at low Frequencies

The frequency reference cavity is designed to show optimal performance at the frequency region of interest for the sub-SQL interferometer. At lower frequencies the performance is limited due to the pendulum resonances of the suspensions. The lowest resonance frequencies are around 0.6 Hz while the higher bounce modes are around 25 Hz. In the initial design of the frequency control loop it was planned to stabilize the laser to an iodine reference at frequencies below 4 Hz. Therefore the south frequency reference cavity suspension is equipped with magnets and coils at the mirror and at the intermediate mass. This was meant to compensate for slow long-term drifts of the cavity in the longitudinal direction and improve the low frequency performance of the frequency reference cavity. During writing this thesis, this is not fully integrated in the system and the final frequency stabilization scheme at low frequencies is under discussion.

Another possibility is to use an additional rigid spacer cavity made from a low thermal expansion material, installed in a quiet environment as for example inside the vacuum
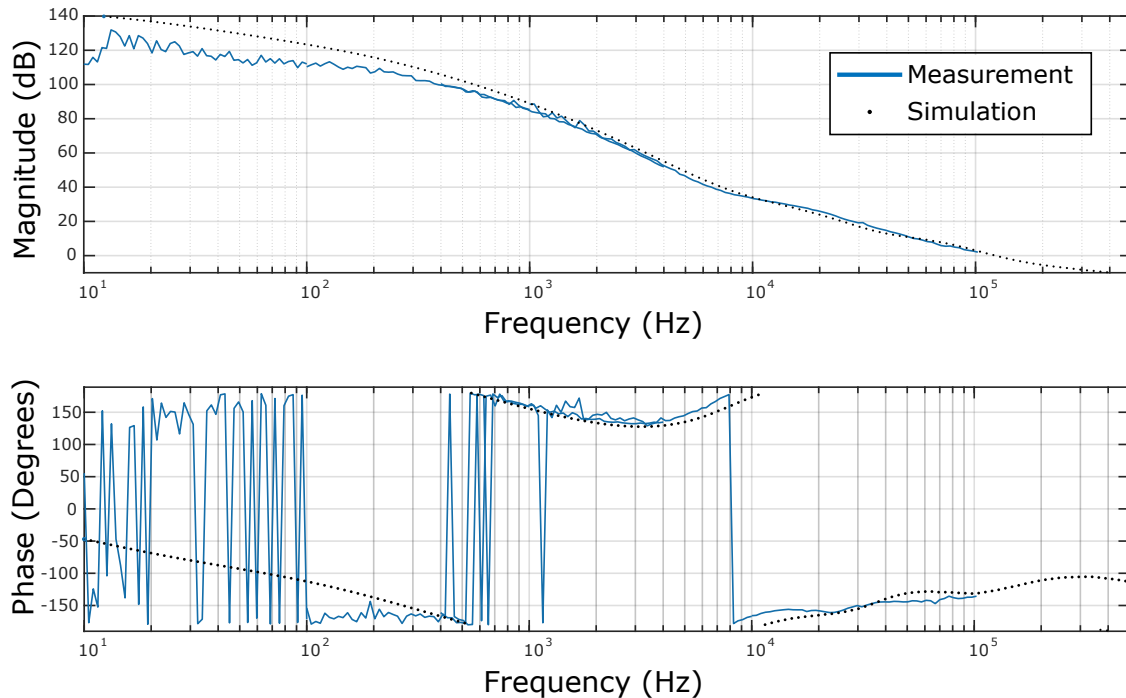
Figure 3.28: Open loop gain of the stabilized frequency reference cavity. This includes the feedback control loops for the different actuators PZT and EOM. The measurements and simulations were performed by D. Wu.

system of the AEI 10 m Prototype.

Similar to this solution, another option is to use the mode cleaner cavity for that purpose. The advantage is its availability in the system and the composition of a low thermal expansion material which is well suited for a stable length reference at frequencies below approximately 4 Hz. The noise performance of the mode cleaner is not fully investigated at the moment.

Improved damping of the pendulum resonance frequencies might be sufficient for the low frequency performance.

3.4.3 Auto-Alignment with Differential Wavefront Sensing

During operation of the frequency reference cavity slow angular drifts or disturbances can potentially drive the cavity out of its locking range. To compensate for longterm drifts and misalignments due to seismic motion or other noise contributions an auto-alignment system was implemented at the frequency reference cavity.

Figure 3.29 shows a sketch of the auto-alignment system. It provides an aligned input

path to the cavity mode using the two suspended steering mirrors in front of the cavity in a feedback control loop. A change in the alignment of the cavity input beam in shift or tilt is detected by two quadrant photodiodes on the detection bench. The information is processed in CDS and sent to the steering mirrors which can be remotely controlled and are aligned such that they minimize the error signal.

The goal of auto-alignment is to provide a better longterm stability of the cavity resulting in an optimized noise performance.

Spot position QPDs are placed behind the cavity mirrors and the second steering mirror to detect beam misalignments on the mirrors.

The sensing matrix for the auto-alignment scheme was determined in transfer function measurements; therefore, the two steering mirrors were excited in pitch and yaw and the transfer function from the steering mirrors to the WFSs were measured. The response magnitude for every combination (SM1 to WFS 1, SM1 to WFS2, SM2 to WFS1 and SM2 to WFS2) was taken and a linear combination of these were made in order to minimize the error signal that is going to the steering mirrors.

Information about wavefront sensing auto-alignment systems for triangular cavities can be found in [Eic03].

The input light of the frequency reference cavity is phase modulated at 8.074 MHz. While the carrier of the light is transmitted into the cavity the two sidebands are reflected since they do not fulfill the resonance condition. Some of the circulating light inside the cavity is transmitted through the output mirror. The principle of differential wavefront sensing compares the wavefronts of the directly reflected light from the cavity and the light that leaks out of the cavity which gives information about the angular alignment of the incoming beam to the cavity mode. WFS are used to detect the demodulated light field reflected at the cavity.

A tilt of the two light fields relative to each other can only by detected in the near field and not in the far field. The situation for a beam shift is the other way around. This is shown in figure 3.30. To cover both beam tilts and shifts two photodiode are necessary. Assuming Gaussian beams, they need to be separated by one Rayleigh range to cover both the near field and the far field. Equivalent, that means that the Gouy phases between the two fields or in other words the positions where the WFSs need to be placed, are separated by 90°. Dependent on the cavity waist and the laser wavelength the Rayleigh range is several meters in case of the frequency reference cavity. Therefore, a projection of the far field is produced by a Gouy phase telescope consisting of three lenses.

Design and Layout of the Gouy-Phase Telescope

The requirements for the Gouy phase telescope are given by the desired Gouy phase difference of 90° and the aspired spot sizes on the WFSs of about 4 mm. These spot sizes were chosen in order to guarantee a good distribution of the laser beam on the quadrant photodiodes without being too large for the active photo sensitive area of 8 mm. The Gouy
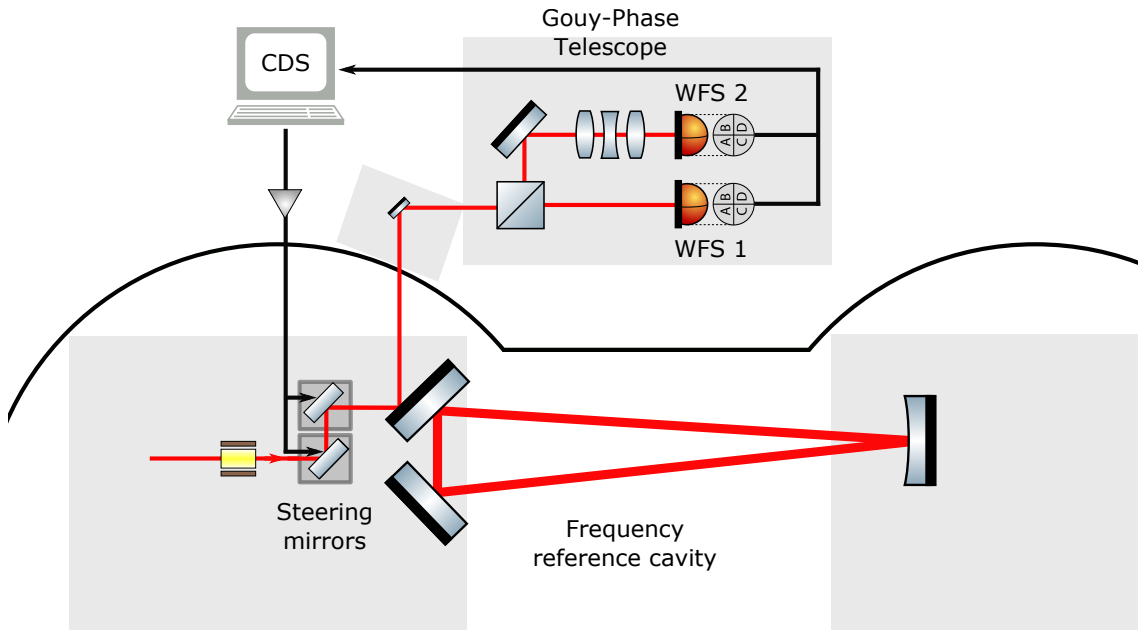
Figure 3.29: Layout of the auto-alignment for the frequency reference cavity. The reflected beam of the cavity is monitored by two RF quadrant photodiodes (WFS1 and WFS2). The are separated by a Gouy phase difference of 90°, provided by a Gouy-phase telescope. The detected signal gives information about any shift or tilt of the reflected laser beam. This information is filtered, amplified and processed in CDS and fed back to the steering mirrors in front of the frequency reference cavity to ensure an aligned input path.
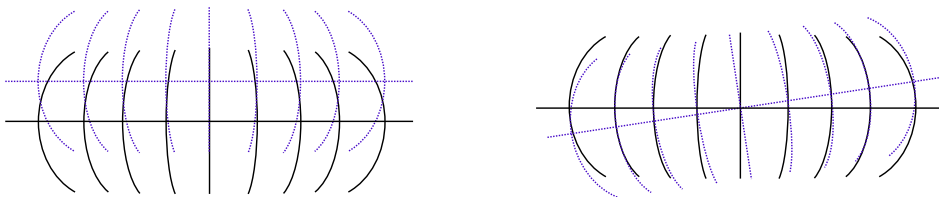
Figure 3.30: The wavefronts of two laser beams which are shifted vertically are equal in the near field but differ in the far field (left picture). This can be detected by a quadrant photodiode. A beam tilt is detectable in the near field but not in the far field (right picture)

phase difference of 90° is desirable in order to get a maximum actuation range. At the same time, the laser propagation path should not become too long due to limited space on the detection bench and the space requirements in the laboratory.

The constellation of lenses and their positions were modeled initially with a Matlab script and verified with JAMMT. The Matlab script iteratively changes the positions of the different lenses and gives the results for the desired beam parameter.

The Gouy phase telescope is created by three lenses in total with the compromise to use as few lenses as possible and to get a resulting beam path length that is realizable due to the space constrains on the detection bench. The lenses have focal lengths of 750 mm (L1), −75 mm (L2) and 200 mm (L3) and are distributed in the reflected beam path of the cavity on the detection bench.

The layout of the detection bench with the positions and focal lengths of the three Gouy phase telescope lenses is shown in figure 3.21.

Wavefront Sensors

The RF WFSs used for the differential wavefront sensing were built at GEO 600, used for their auto-alignment system. They are quadrant photodiodes with an active area of 8 mm and directly attached analog electronics in the housing. The RF demodulation is implemented in a built-in circuit board. An external phase shifter box is needed to adjust the phase of the local oscillator. The DC signal subtraction to get the pitch and yaw signals from the raw data of the four quadrants is done in CDS. The two upper quadrants are subtracted from the sum of the two lower quadrants to obtain the pitch signal and the two left quadrants are subtracted from the two right quadrants for the yaw signal. The demodulated signals are also calculated into pitch, yaw and sum of the WFSs.

The output signals from the WFSs are processed in CDS.

Spot-Centering System of the Wavefront Sensors

Due to the long lever of several meters of the reflected cavity beam to the two WFSs already small misalignments of the input mirror or the in-vacuum optical tables cause a significant displacement on the detection bench. The beam spot size on the WFS is 4 mm while the WFSs have an active photo sensitive area of 8 mm.

To avoid misalignments on the QPDs, a spot-centering system is implemented for the WFSs. This is realized by two mirrors in front of each WFS mounted onto one galvo motor each. A photograph of such a galvo scanner with two mirrors is shown in figure 3.31. The galvo scanner used for the spot-centering system are from Cambridge Technology (Open Loop Scanner, model G102). Square-shaped 10 mm x 15 mm mirrors are glued into a small aluminum holder which is attached to the rotation axis of the galvo motor such that they can control pitch and yaw motion of the laser beam incident on the WFS. With this design, the laser beam is raised by 2.5 cm and rotated in polarization.

The motors are connected to CDS and can thus be controlled remotely. A control loop

feeding back the WFS signal to the galvo scanner is implemented to keep the laser beam centered onto the WFS.

The orientation of the galvo mirror rotates the beam by 90°. Horizontal motion of the beam, e.g. due to yaw motion of the frequency reference cavity, is converted to vertical motion on the QPD and vice versa for vertical motion of the beam due to pitch motion of the cavity. This is corrected digitally with CDS.

Since the galvo scanner in front of WFS 2 is placed before the locking photodiode, this also profits from the spot centering system and provides an aligned input beam on the locking photodiode.
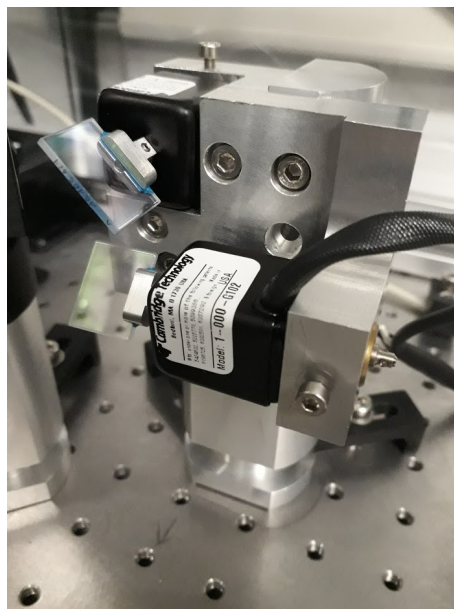
Figure 3.31: Galvo scanner with two mirrors mounted to their rotation axis to control pitch and yaw of the laser beam. Two galvo scanners are placed in front of each WFS. They are controlled via CDS. A spot-centering control loop centers the laser beam on the WFSs.

CHAPTER 4

Triple Suspension Damping Investigation and Improvement

To achieve the required frequency sensitivity in the SQL measurement band around 200 Hz the frequency reference cavity mirror motions need to be minimized to provide a stable length reference to which the laser frequency can be stabilized. This requires both passive isolation against seismic disturbances and active damping of the suspension resonances with the aid of control loops that can read out the current position and bring the mirror back to the desired location. The suspension resonance frequencies are below the SQL measurement band but low frequency motion could induce noise at higher frequencies and should be therefore minimized.

The AEI-SAS and the SPI provide pre-isolation in addition to the passive isolation of the pendulum suspensions. This is introduced in 2.3. Without this pre-isolation, the RMS motion of the suspensions would be on the order of micrometers. Further seismic isolation of the optics is provided by the triple pendulum suspensions. They are designed to suppress mirror motion above 10 Hz as described in 3.3.1. While the previous chapter mainly describes the mechanical design and passive seismic isolation, this chapter focuses on the active control and damping of the frequency reference cavity suspensions.

4.1 Active Damping of the Frequency Reference Cavity Suspensions

The three pendulum stages of the suspensions provide horizontal isolation with a slope of $1/f^2$ for each stage. In addition, vertical isolation is achieved by suspending the masses from two stages of stiff blade springs. The mirrors were chosen heavy compared to the SQL mirrors in order to minimize radiation pressure coupling and to push violin modes to higher frequencies of hundreds of Hertz.

The mirror motion is decoupled from seismic noise at frequencies above 10 Hz in most degrees of freedom. Only the vertical and roll modes appear at higher frequencies. The aim of damping is to suppress the cavity mirror motion at the pendulum resonance frequencies such that the mirror returns to its original position after an excitation of the ground. The noise coupling of individual mirrors into changes in the cavity length should be minimized, since this movement corresponds to the frequency fluctuations.

Active control of the frequency reference cavity suspensions is performed at the top mass,

as described in 3.3.1. While the movement of the test masses must be reduced to a minimum, a complete reduction of top mass motion relative to the suspension frame should be avoided. This would lead to an effective attachment of the top mass, which in turn means the omission of a pendulum step. Instead, the inertial movement of the masses needs to be suppressed. The suspensions need to be characterized in order to design suitable digital damping filters. Therefore, transfer function measurements of the triple pendulums from an excitation of the top mass to the motion of the mirror mass were measured to obtain information about the system's behavior. Damping filters can be chosen and optimized by knowing the transfer functions for different degrees of freedom.

The efficiency of damping can be analyzed by ring-down measurements. These measurements determine the time it takes for the suspension to drop to $1/e$ of its original excitation amplitude after excitation. Ring down measurements performed at the frequency reference cavity suspensions will be presented in 4.3.2.

Around their resonance frequencies, the suspensions are sensitive to ground motion excitations. This complicates lock maintenance of the frequency reference cavity and can in the worst case lead to wire failure. The requirement of active damping is essential around their pendulum resonance frequencies. Since a long-term stability of the frequency reference cavity is required, it is equally important that the mirror suspensions already show a stable behavior. This also means that the damping is able to suppress all suspension excitations satisfactorily, ensuring the long-term behavior of the frequency reference cavity and a high lock acquisition rate.

4.1.1 Sensors and Actuators

The position readout and actuation is applied to the top mass of the suspension chain. A contact-less actuation is recommended for the control of the suspensions, as this does not have any disadvantages due to mechanical connections between suspension and ground such as cables. In case of the frequency reference cavity suspensions, the position of the top mass is controlled by BOSEMs, introduced in 3.3.3. They are attached to the suspension frame. This has the advantage that electronic noise induced by the readout and actuation electronics is filtered by the pendulum stages to avoid coupling into mirror motion. All cable-containing parts are connected to the suspension frame and thus the optical table and not to the suspension itself. The sensed motion is measured relative to ground where the sensors can not distinguish between ground motion and movement of the mass. An overview about the BOSEM locations at the top mass and which degrees of freedom they control is shown in figure 4.1. Six sensor-actuator pairs are required for sensing and controlling the position of the top mass in all degrees of freedom. Three BOSEMs are located on top of the top mass to sense and actuate the vertical degrees of freedom. Vertical movement of the complete mass as well as pitch of the mass which raises or lowers the beam and roll around the beam axis which ideally has no effect on the beam itself.

Cross-coupling between the different degrees of freedom occurs due to slight deviations in the structure of the suspensions and tolerances of the assembled components. For example, pitch motion couples into longitudinal motion of the top mass since the wire's suspension points are not in the center of mass of the top mass. In addition, the two BOSEMs at the front of the top mass responsible for long motion (BOSEM D and E in figure 4.1) also induce pitch motion since they are not placed on the same horizontal axis but separated by some millimeters.

BOSEM Noise

Active damping in a feedback loop is limited by the performance of the sensors and actuators. The BOSEM noise floor sets the limitation for the suspension damping performance. BOSEM sensing noise consists of the noise of different components, e.g. photodiodes, LEDs and coils. The photodiodes and LEDs of the BOSEMs are shot noise limited above 5 Hz. Actuation noise of the coils contributes in addition to this.
A detailed description of the BOSEMs and a full characterization of their performance can be found in [Ast11]. The BOSEM noise requirements for aLIGO are $3 \times 10^{-10} \, \text{m}/\sqrt{\text{Hz}}$ at 1 Hz dropping down to $10^{-10} \, \text{m}/\sqrt{\text{Hz}}$ at 10 Hz. At frequencies below 0.1 Hz the noise rises significantly.

4.1.2 Different Damping Approaches

Damping of the suspensions resonance frequencies can be applied in different ways. An overview is given in the following sections.
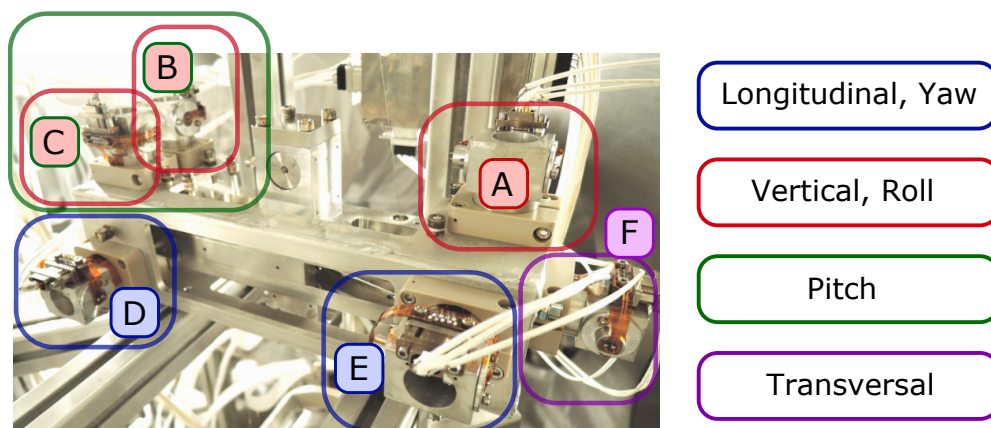
Figure 4.1: Overview about the BOSEM locations at the top mass and the according degrees of freedom controlled by them.

Point-to-Point

The initial damping at the frequency reference cavity is applied from one BOSEM sensor to the corresponding actuator. In particular, the position of the suspension chain in respect to the ground is sensed by every BOSEM and fed back to the same BOSEM.
Figure 4.2 shows a block diagram of the point-to-point damping at the frequency reference cavity suspensions. The readout of the BOSEMs is done with analog electronics outside of the vacuum system. For this, the cables of the individual BOSEMs are connected to a vacuum feed through and routed to the electronic racks which contain the BOSEM readout electronics. The signals are digitized with an ADC and converted from CDS counts into micrometers. Damping filters are simple velocity damping filters and are applied to every individual BOSEM. They are equal in aspects except their overall gain which was empirically determined and optimized from measured data. The signals are fed back to the coils of the same BOSEM after a re-calibration into CDS counts and a conversion into analog signals with a DAC.
The damping filters for the point-to-point damping are robust, which is advantageous for the initial cavity assembly and alignment phase as well as during pump downs and venting of the vacuum system. It can still provide damping in case of a BOSEM failure, as the malfunction can be compensated with other BOSEMs. Their simplicity and robustness are at the expense of their performance compared to other damping methods.

Degree of Freedom

Another possibility of active damping apart from feeding back to individual BOSEMs is to convert the BOSEM signals into the six different mechanical degrees of freedom longitudinal, pitch, roll, side, vertical and yaw. The feedback signal is applied to these degrees of freedom. This is called degree of freedom damping at the AEI 10 m Prototype, although the feedback is applied locally at every suspension and is designated as local damping in aLIGO.
A schematic of the degree of freedom damping at the frequency reference cavity suspensions is shown in figure 4.3. The readout, conversion into digital signals and calibration into micrometers is identical to the point-to-point damping. But in contrast to that, the signals from the individual BOSEMs are converted into the different degrees of freedom by a sensing matrix. The matrix entries are modeled based on the geometry of the top mass and the BOSEM placement. The same accounts for the actuation matrix which converts the degrees of freedom back to correspond to the individual BOSEMs. The sensing and actuation matrices are constant and equal for every suspension.

Multiple-Input Multiple-Output

Multiple-input multiple-output (MIMO) damping is a modern control approach where, in case of frequency reference cavity damping, the signal from every BOSEM is fed back to
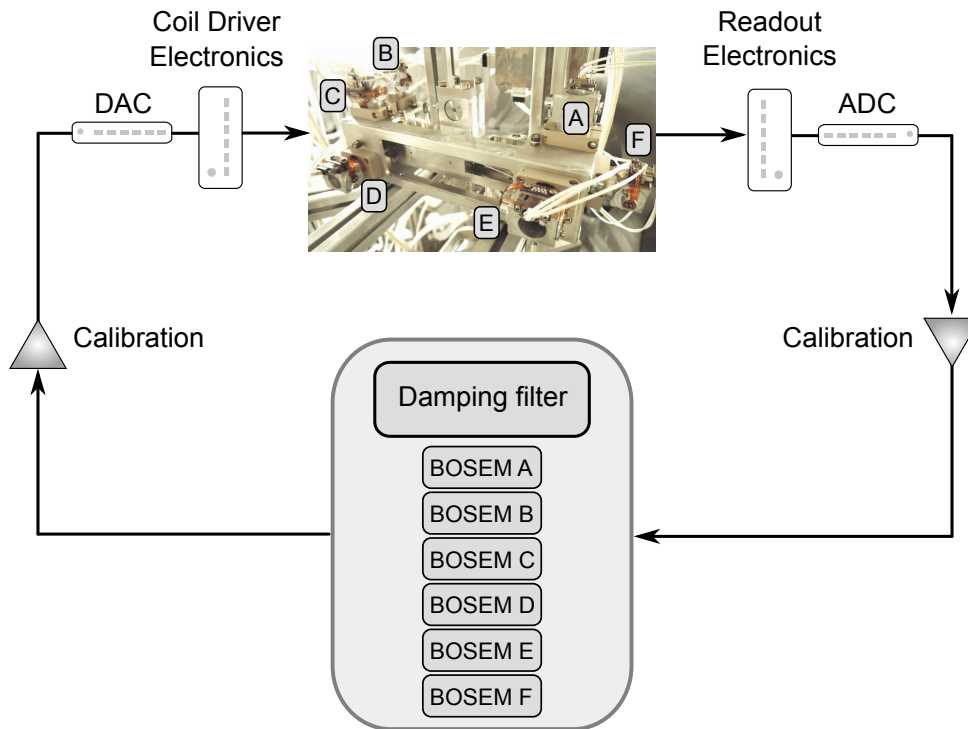
Figure 4.2: Schematic of BOSEM point-to-point damping at the frequency reference cavity. The BOSEMs are connected to readout electronics outside the vacuum system and converted into digital signals in the ADCs. A calibration filter converts the signals from CDS counts into micrometers. A damping filter for every individual BOSEM signal is applied and then fed back to the coils of the same BOSEM after a re-calibration into CDS counts, a conversion into an analog signal in the DACs and passing the coil driver electronics.

all BOSEMs. This method takes cross-coupling between the different degrees of freedom into account which is not the case for Single-Input Single-Output (SISO) schemes.

To realize MIMO damping, the system needs to be well-known and the suspensions need to be fully characterized. Transfer function measurements from the suspension point to the mirror masses are necessary to provide useful information for a damping filter design.

MIMO damping of triple suspensions equivalent to the frequency reference cavity suspensions was investigated by the Quantum Control group at the AEI in Hanover and is described in [Sch16]. A structurally identical suspension to the frequency reference cavity suspensions was set up in air. Actuation was done at the top mass with BOSEMs while the read out could be realized at the lower mass by using optical levers. The damping filters were designed based on the transfer function measurements from the optical lever set-up. MIMO damping for the suspensions of the AEI 10 m Prototype system is not realized yet
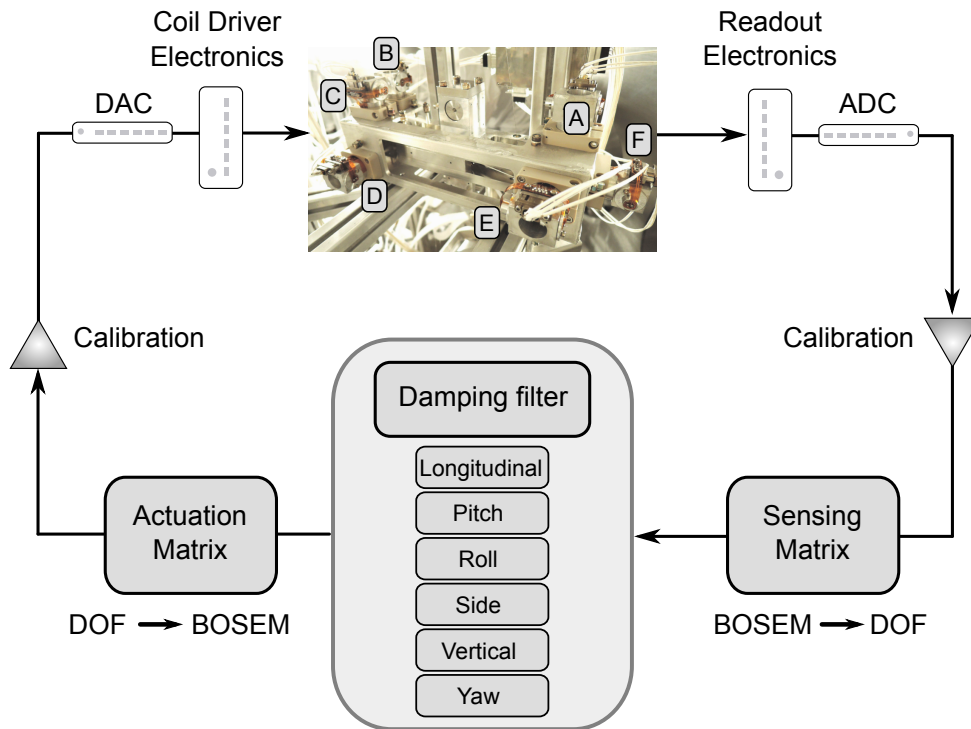
Figure 4.3: Schematic of degree of freedom damping at the frequency reference cavity. Likewise to the point-to-point damping, the BOSEM signals are processed in readout electronics, converted into digital signals in the ADCs and calibrated into micrometers. A sensing matrix converts the BOSEM signals into the six degrees of freedom. The entries of the matrix are based on the geometry of the top mass and the BOSEM positioning. Damping filters are applied for every degree of freedom individually. These signals are converted back into BOSEM signals with the actuation matrix, calibrated back into CDS counts and converted into analog signals. After passing the coil driver electronics the signals are fed back to the coils of several BOSEMs depending on the degree of freedom they control.

and would need some more investigation before it can be adapted for the same.

Global Cavity Length Control

Global length control at the frequency reference cavity is not implemented for each individual suspension but is applied instead to one suspension only, which in turn controls the longitudinal movement of the entire cavity. Therefore global damping in the context of the frequency reference cavity means global longitudinal control of the cavity rather than suspension damping. It is mentioned in this context, because it is also used to damp the fundamental longitudinal resonance frequency of the suspensions.

For the implementation of global longitudinal control, the calibrated mode cleaner feedback signal is used as readout for the frequency reference cavity length. This signal includes a damping filter that is adapted to the relevant transfer function and is fed back to the curved cavity mirror.

The performance of the suspensions was characterized in transfer function measurements of the longitudinal degree of freedom. From this information, the control loop's plant was designed and tested together with the damping filter to simulate the damping performance. More details on this scheme and its results are discussed in section 4.4.
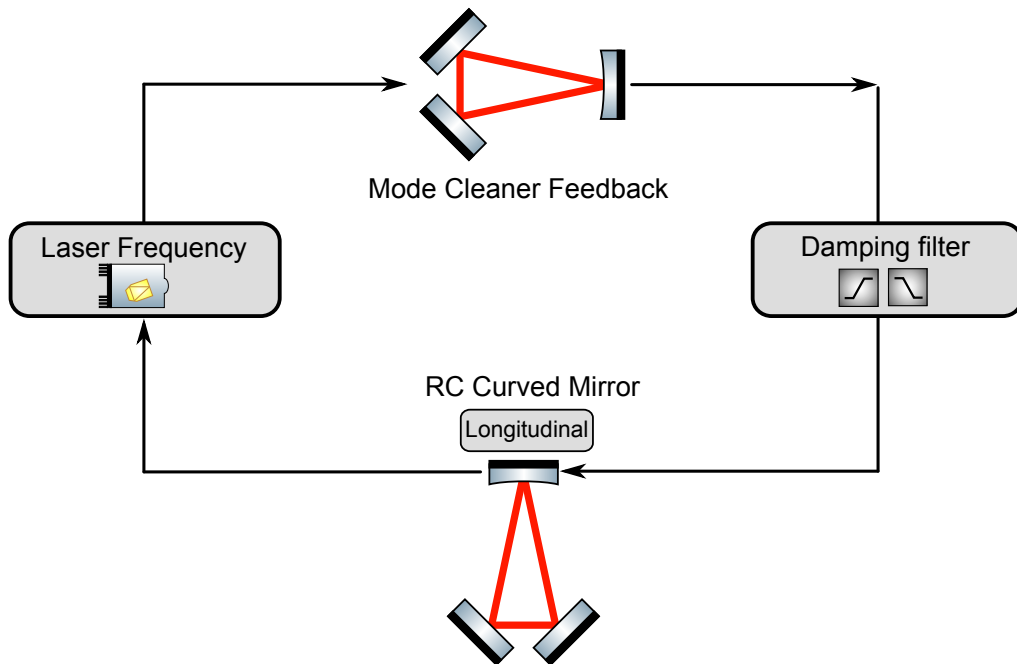
Figure 4.4: Schematic of global longitudinal control of the frequency reference cavity. The longitudinal motion of the cavity mirrors and therefore the cavity length resulting in a laser frequency change is measured by the mode cleaner. The laser needs to be locked to the frequency reference cavity and the mode cleaner follows the laser frequency. The frequency fluctuation of the laser light is measured by the mode cleaner and the feedback signal of the mode cleaner is fed back to the curved frequency reference cavity mirror after passing the global longitudinal control damping filter.

4.2 Characterization of the Triple Suspensions

A complete characterization of the triple suspensions is needed to understand their damping performance and to improve the damping efficiency.

Figure 4.5 and 4.6 show the ASDs of the curved cavity mirror motion for the different degrees of freedom. The measurements were performed while the cavity was locked with suspension damping switched off. The resonance frequencies for different degrees of freedom are colored according to the values in the table 4.1. In addition to the resonance frequencies of the respective degrees of freedom, other resonances are visible in the spectrum, which result from cross-coupling of other degrees of freedom. The state space model, introduced in section 4.2.2 was used to determine the individual degrees of freedom with the corresponding resonance frequencies.

The resonance frequencies for the three frequency reference cavity suspensions for all six degrees of freedom compared to the simulated resonance frequencies from the state space

model are shown in table 4.1. The resonance frequencies differ from the measurements carried out previously in [Wes16] because two of the suspensions had to be re-suspended due to wire failures. To make sure that no significant change of the resonance frequencies occurred they were measured after re-suspending the optics. Pitch as the softest degree of freedom shows the most noticeable deviations from the previously measured values in comparison between the three suspensions.

Table 4.1: Suspension resonance frequencies from the measurement in comparison to the model.

DOF	Model	RCIM Suspension	RCOM Suspension	RCCM Suspension
Long.	0.64 Hz	0.64 Hz	0.63 Hz	0.64 Hz
	1.39 Hz	1.37 Hz	1.38 Hz	1.38 Hz
	2.59 Hz	2.54 Hz	2.56 Hz	2.54 Hz
Pitch	0.98 Hz	0.88 Hz	0.69 Hz	0.79 Hz
	1.88 Hz	1.65 Hz	1.72 Hz	1.6 Hz
	5.2 Hz	5.45 Hz	5.1 Hz	5.02 Hz
Roll	2.26 Hz	1.03 Hz	1.03 Hz	1.03 Hz
	9.12 Hz	3.6 Hz	3.64 Hz	3.66 Hz
	26.54 Hz			
Side	0.64 Hz	0.64 Hz	0.63 Hz	0.64 Hz
	1.39 Hz	1.41 Hz	1.42 Hz	1.41 Hz
	2.61 Hz	2.55 Hz	2.54 Hz	2.55 Hz
Vert.	1.24 Hz	0.98 Hz	0.98 Hz	0.98 Hz
	4.07 Hz	3.72 Hz	3.76 Hz	3.76 Hz
	18.62 Hz	24.03 Hz	24 Hz	26.6 Hz
Yaw	0.97 Hz	0.83 Hz	0.82 Hz	0.85 Hz
	2.3 Hz	1.6 Hz	1.6 Hz	1.6 Hz
	5.55 Hz	3.09 Hz	3.07 Hz	3.09 Hz

4.2.1 Transfer Functions and Cavity Length Performance

To analyze the suspension behavior during ground excitations in the different degrees of freedom, transfer functions from the respective suspension point to the movement of the lowest mass were measured. An exact idea of where the resonance frequencies of the individual pendulum stages are for the different degrees of freedom is a prerequisite for the analysis and possible improvement of the active damping, especially when more advanced damping methods are required. A limitation is the readout of the mirror motion. In the initial experimental setup of the frequency reference cavity, no readout techniques for the individual cavity mirror motions like optical levers were implemented. Optical lever measurements of constructionally identical suspensions were performed in the Quantum Control Group of the AEI Hanover. Detailed information can be found in [Sch16]. This
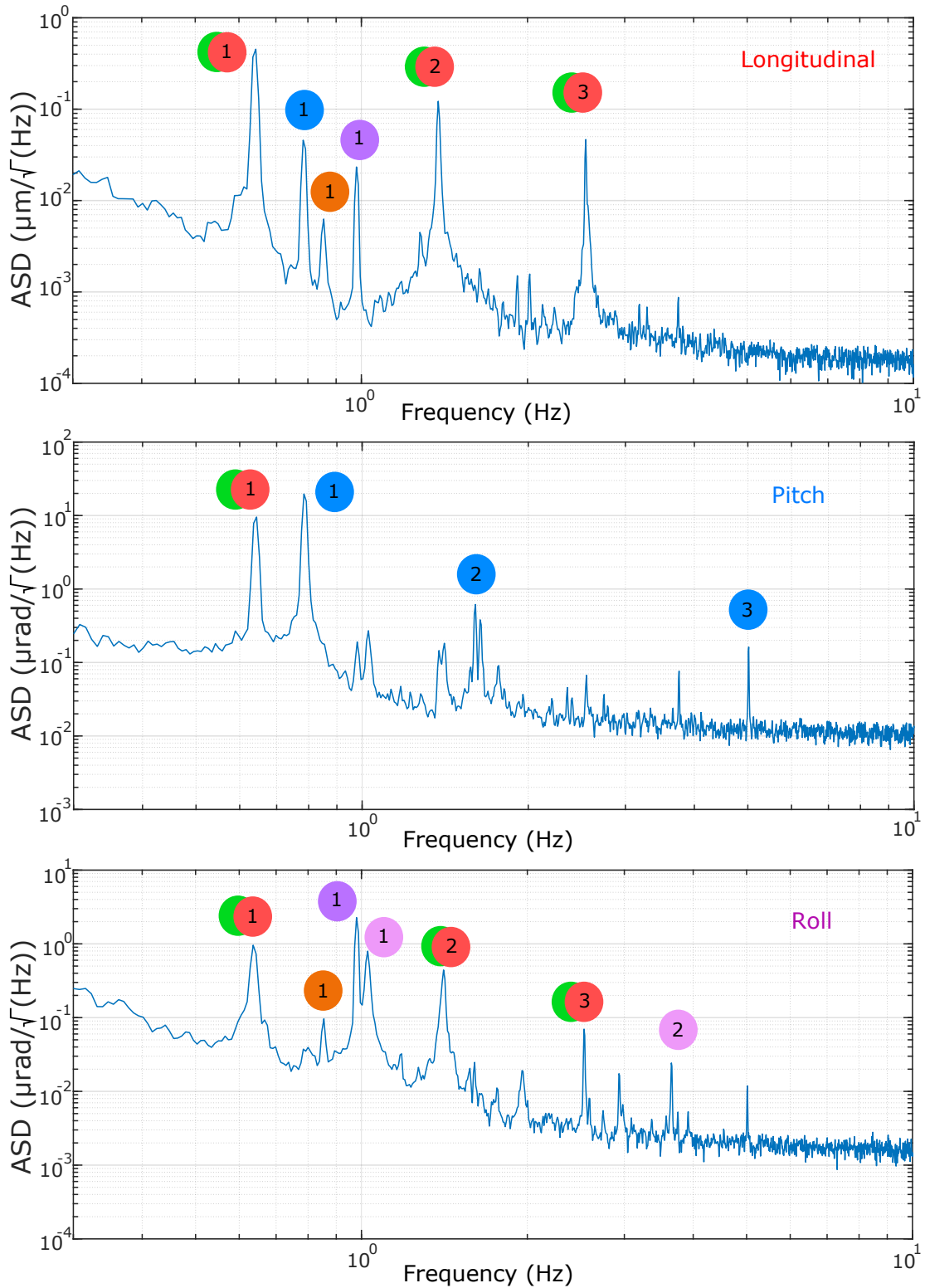
Figure 4.5: ASD for the frequency reference cavity curved mirror suspension for longitudinal, pitch and roll. The measurements were performed during the cavity was locked with suspension damping switched off. The resonance frequencies for different degrees of freedom are colored according to the values in the table 4.1.
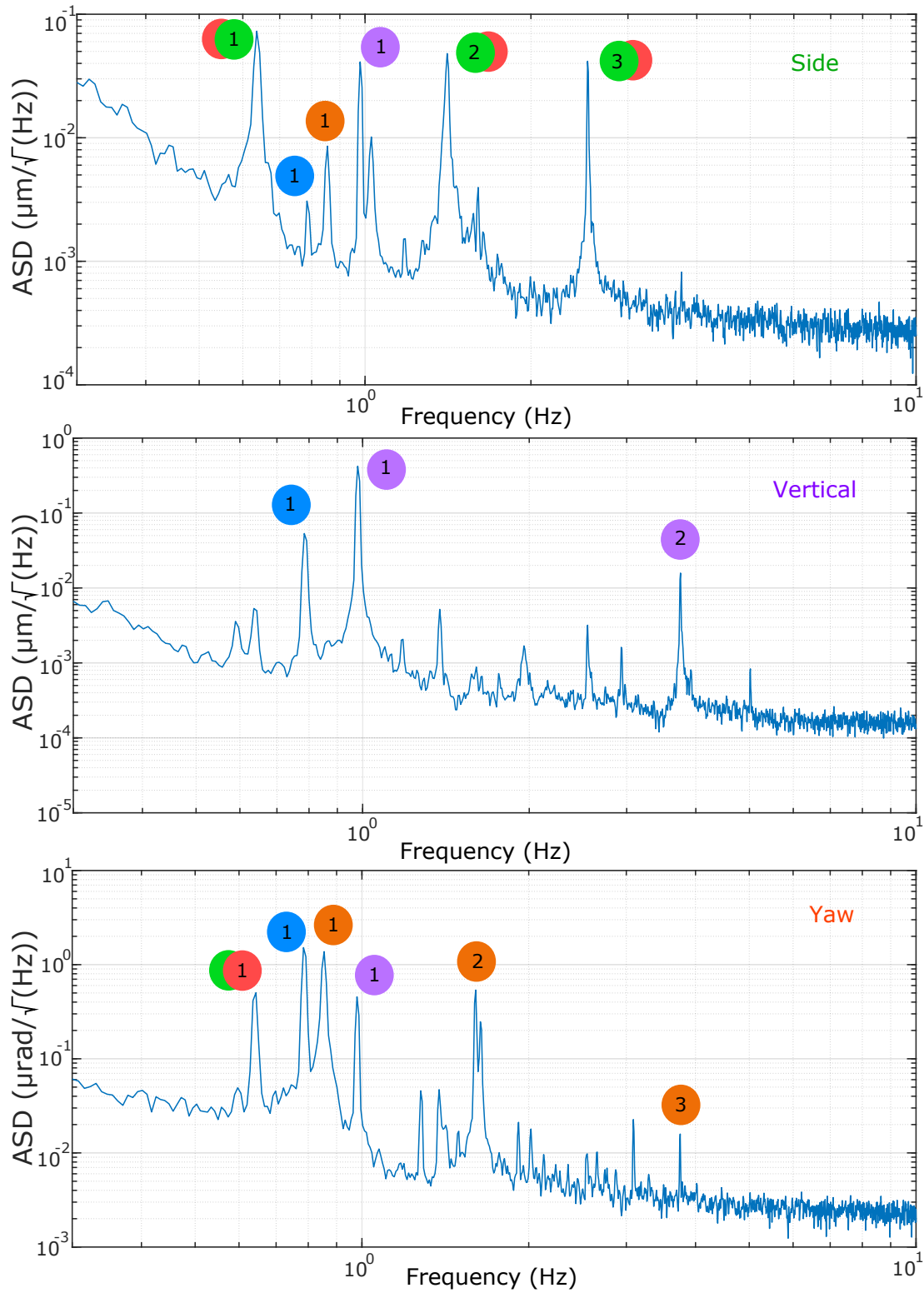
Figure 4.6: ASD for the frequency reference cavity curved mirror suspension for side, vertical and yaw. The measurements were performed during the cavity was locked with suspension damping switched off. The resonance frequencies for different degrees of freedom are colored according to the values in the table 4.1.
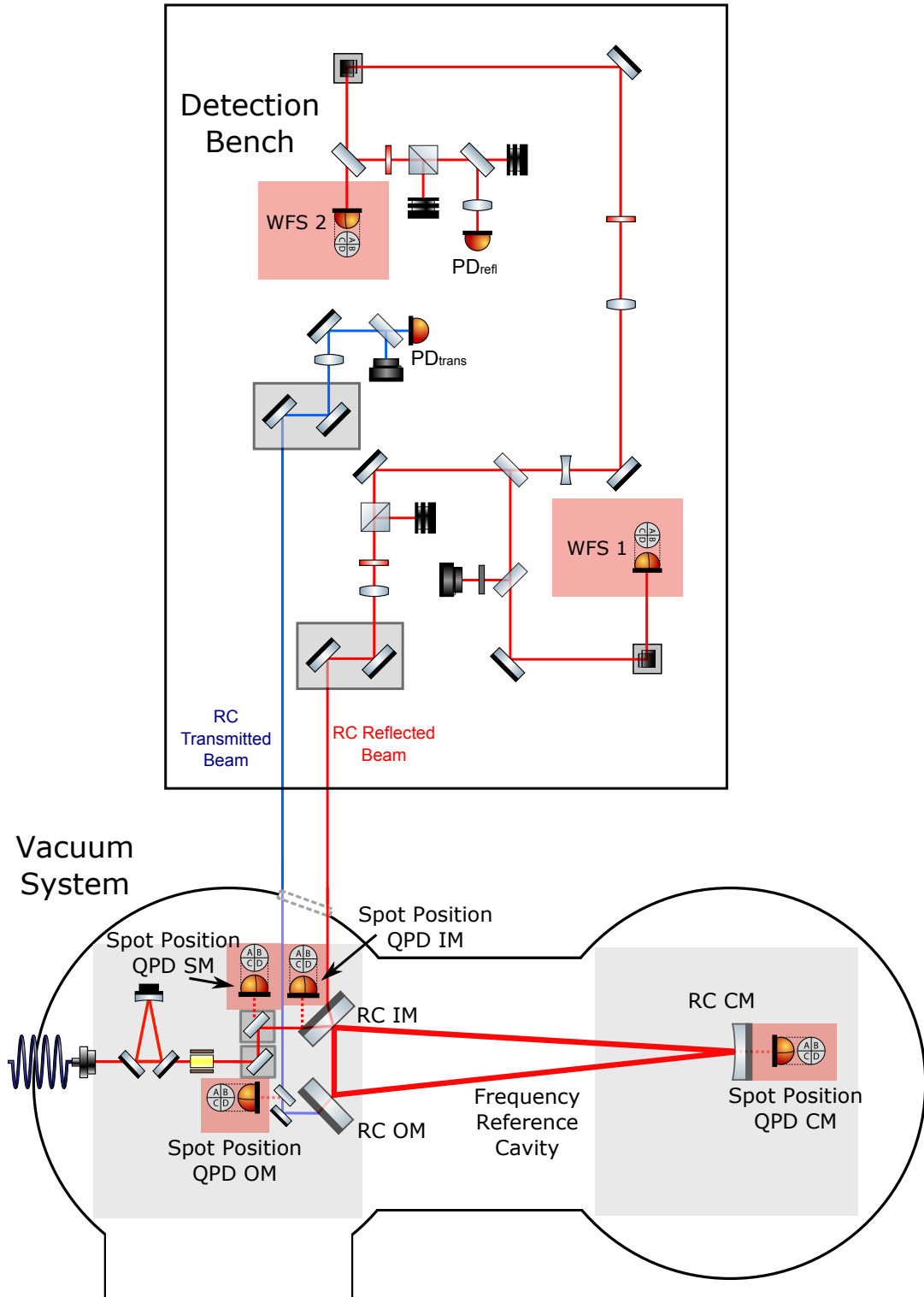
Figure 4.7: Overview of the locations of the in-vacuum spot position QPDs and the WFS on the detection bench, highlighted in red.

method uses two additional laser beams incident on a suspended mirror and being reflected from the mirror towards two QPDs under different angles. This is sensitive to pitch, yaw and longitudinal. The technology was demonstrated but has not yet been implemented at the AEI 10 m Prototype.

In case of the frequency reference cavity, the longitudinal motion of the mirrors change the cavity length. This can be read out by the feedback signal of the locked cavity or the mode cleaner feedback signal. The input mirror motion can also be read out in pitch and yaw by the spot position QPD that is placed behind it to detect any beam position displacement on the mirror and to serve as a reference during cavity alignment. Due to the short lever arm of approximately 10 cm this requires a higher excitation on the suspension point to get detectable results on the quadrant photodiode.

Figure 4.7 shows an overview of the locations of the in-vacuum QPDs and the WFS on the detection bench outside the vacuum system. The spot position QPDs of the curved cavity mirror on the south optical bench and the output cavity mirror are not suited for read out for transfer function measurements. They are placed behind high reflectivity mirrors and are sensitive to transmitted cavity light when the latter is well-aligned. Especially the curved mirror which transmits only 4 ppm can not be read out with a QPD in transmission. The transmitted light of the flashing cavity interferes with the measurement signal so that this option is omitted. For the transfer function measurements of the input mirror in pitch, yaw and longitudinal the cavity was misaligned to avoid flashes.

Transfer function measurements with the wavefront sensors on the detection bench as a mirror motion readout showed no satisfying results. They are positioned on the detection bench outside the vacuum system whose position is not controlled with respect to the in-vacuum table position which is seismically isolated and the measurement is dominated by seismic noise.

The excitation at the top mass during the measurement was frequency dependent in order to excite less at the resonance frequencies but enough for a sufficient Signal-to-Noise Ratio (SNR). Above the pendulum resonance frequencies the excitation was increased because the excitation gets damped due to the $1/f^6$ isolation slope. The measurements were taken in a frequency range from 0.1 Hz to 10 Hz. Above 2 Hz, the coherence of the measurements is decreased significantly.

The cavity feedback control signal contains information about the length stability of the frequency reference cavity. To characterize the performance of the cavity an analysis of how much movement of the ground would result in how much longitudinal cavity motion at different frequencies has been carried out. Therefore transfer function measurements from the south suspension to the mode cleaner feedback signal were taken. The mode cleaner signal is calibrated in micrometers and is therefore a suitable tool for measuring the length performance of the frequency reference cavity at frequencies up to 4 Hz. Above that, it gets noisier than the frequency reference cavity feedback signal which is dominated by free running laser frequency noise.

Figure 4.8 shows the transfer function from the top mass of the frequency reference cavity

output mirror to the mode cleaner cavity feedback signal. The measurement was done in vacuum with the AEI-SAS in full control and the SPI switched on. The frequency reference cavity was locked but damping of the suspensions was switched off in order to characterize the suspension behavior without damping. The suspension was excited at the top mass BOSEMs in longitudinal direction. The three longitudinal resonance frequencies are visible at 0.63 Hz, 1.38 Hz and 2.56 Hz. Residual resonance peaks are caused by cross-coupling from other degrees of freedom, the most prominent being e.g. pitch resonances at 0.69 Hz and 1.72 Hz. The transfer functions were measured from the excitation signal in CDS to the mirror since the same measurement from the BOSEMs to the mirror is limited by the accuracy of the BOSEM sensor.

These measurements, which were performed with the locked frequency reference cavity, contain information about a cavity length change and provide information about all three cavity mirrors simultaneously.

4.2.2 Modeling the Suspensions

A simulation of the suspensions of the frequency reference cavity is demanding due to their complexity. A state space model was used as a solution to model the suspensions. An introduction into the state space model can be found in [Fri12]. It describes the different degrees of freedom of the suspended masses and is for instance able to simulate their transfer functions and behavior after excitations at various points.

The state space model was customized to suit the triple suspensions of the frequency reference cavity by changing dimensions, distances and other parameters. One of the modifications to the state space model was the splitting of the signals into the six BOSEMs at the top mass to describe the point-to-point damping. In this thesis, the state space model was used to simulate the transfer functions for the different degrees of freedom and to model OLGs in order to find the optimal gain settings; see section 4.3.1. The stability of damping loops was also tested and examples for the same are shown with ring-down simulations and Bode plots. The initial design and testing of the damping filter before implementing them in the suspensions was done with the state space model.

More information about the theory of state space modeling can be found in [Sch16]. An extraction of the simulink model including the state space model for longitudinal and pitch motion is attached in the appendix A.1.
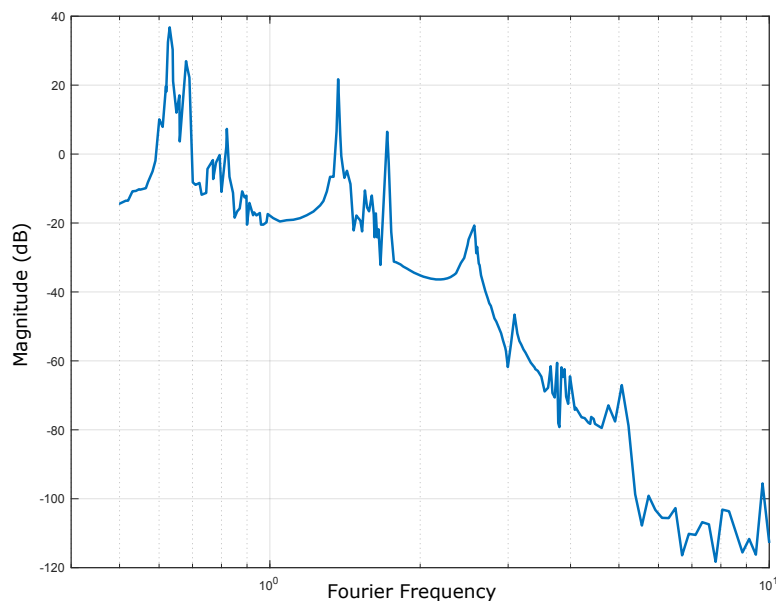
Figure 4.8: Transfer function from excitation of the top mass of the output mirror suspension in the longitudinal degree of freedom to the mode cleaner cavity feedback signal. The three longitudinal resonance frequencies at 0.63 Hz, 1.38 Hz and 2.56 Hz are visible as well as a $1/f^6$ decay above the third resonance. Cross-coupling from other degrees of freedom is indicated by the residual resonance peaks, the most prominent being e.g. pitch resonances at 0.69 Hz and 1.72 Hz. The measurement was done with Diagnostic Test Tools (DTT) in a swept sine measurement. The amplitude of the excitation was frequency dependent in order to excite the suspension less around the resonance frequencies and more above the resonances.

4.3 Improved Degree of Freedom Damping

Longitudinal motion of the cavity is the most crucial degree of freedom and the first longitudinal pendulum resonance frequency of the suspensions is also the most prominent one. It is visible in every subsystem measurement and is limiting the sensitivity of the SAT and will be a severe issue for the sub-SQL interferometer. Therefore, special emphasis was taken on the suppression of this mode. The former point-to-point damping was designed to be robust and therefore well-suited during the construction and initial commissioning phase of the frequency reference cavity, as it does not run the risk of driving the loop instable. During the later commissioning phase the robustness of the simple damping filters is no longer the primary requirement but better suppression of the resonance frequencies is required.

Although the point-to-point damping suppressed reliably the suspension motion after excitations the resonance frequencies were strongly visible in power spectra measurements of the SAT, see 2.1.1. Especially the fundamental longitudinal resonance frequency at 0.64 Hz was limiting the SAT performance.

During this thesis new damping filters for the frequency reference cavity suspensions were implemented and tested to realize degree of freedom damping.

Before implementing a new damping filter its design and behavior in a control loop were simulated in the state space model. The design of the damping filter was created with Matlab and Foton and will be discussed in the following. The decision of the filter type and the initial implementation of zeros, poles and gain factors was done in Foton. The according Bode plot can be immediately generated for scrutinizing the filter shape and expose potential stability issues when taken into account all parts of the control loop and display the phase margin at unity gain frequency in the OLG.

4.3.1 Filter Design

For creating damping filters the suspensions need to be well characterized. Around the pendulum resonances more gain is required while at higher frequencies the suspensions suppress motion due to their triple pendulum design.

The resonances of the suspensions are between 0.6 Hz and 10 Hz. Bounce modes and violin modes above 10 Hz are seismically isolated by the pendulum suspensions. Therefore, the damping filters for the frequency reference cavity suspensions were designed to have gain in a frequency region from 0.6 Hz to 10 Hz. New filters for the frequency reference cavity suspensions were simulated with the state space model before being used at the suspensions. Previous transfer function measurements of the suspensions from the top mass to the cavity mirrors showed sufficient agreement with the state space model and indicated the model as a suitable tool for the filter design.

The efficiency of a feedback control loop depends on the performance of the respective sensors and actuators and is limited by the noise introduced by them. The noise of the BOSEMs for example couples into longitudinal motion of the cavity mirrors. For every suspension the BOSEMs at the top mass introduce approximately $1 \times 10^{-19} \, \text{m}/\sqrt{\text{Hz}}$ of longitudinal motion from 30 Hz on. This assumption is a requirement to meet the frequency reference cavity design sensitivity. The electronic noise of the BOSEMs is approximated as $1 \times 10^{-10} \, \text{m}/\sqrt{\text{Hz}}$. This is based on [Ast11] and on former measurements of the frequency reference cavity BOSEMs. Only white noise as BOSEM shot noise was considered. The electronics noise which is actually dominant below 5 Hz was assumed to be small compared to seismic motion. Measured seismic noise from the AEI-SAS was used and extrapolated at high frequencies due to the sensors being noise limited.

Figure 4.9 shows a noise projection of the BOSEMs for longitudinal motion. The upper plot shows a simulation of the suspension ring-down after an excitation to show the damping performance of the filters and display potential stability issues. This simulation was done with the state space model.

The lower plot displays the noise contributions affecting the suspension motions. They consists of BOSEM shot noise, displayed by the blue line, and seismic noise, shown in red. Both contributions are considered after the isolation of the pendulum stages. The total

noise is shown by the yellow dashed line. It touches the target, depicted by the black line, at approximately 30 Hz.

Pitch motion couples into longitudinal cavity motion and needs to be considered as well. The noise projection for pitch is shown in figure 4.10. The total noise touches the target for BOSEM noise at frequencies above 30 Hz. The requirements are less stringent since pitch motion couples less into cavity length changes than longitudinal mirror motion. The first damping filter design is based on a filter that is preferably simple and has sufficient gain around the pendulum resonances. The idea was, to create a filter with a zero at low frequencies that causes the filter shape to rise, a pole for flattening the shape and a roll off by another pole above the resonance frequencies. The new filter for damping of longitudinal motion is a fourth order Butterworth band pass filter with a rising gain from lower frequencies on, a flattened behavior around the pendulum resonance frequencies and a steep roll off above 10 Hz without loosing too much phase to still ensure stability of the loop. The filter is designed to re-gain phase after the steep roll off. A Bode plot of the filter is shown in figure 4.11. The stability of the filters was tested in Bode plots by displaying the filter in combination with the modeled plant. This was simulated based on transfer function measurements which were measured from the suspension top mass to the mirror for every degree of freedom. The damping filters were designed conforming to the transfer function of the suspensions for the individual degrees of freedom.

For the other degrees of freedom besides longitudinal different filters were implemented based on the requirement to use a simple filter to reduce complexity of the control loop. These filters contain a zero at 0 Hz and two poles at 50 Hz. A Bode plot of these filter is shown in figure 4.12. For further suppression of the fundamental longitudinal resonance a resonant gain was implemented in the control loops of all other degrees of freedom. This was implemented at 0.64 Hz for the input mirror suspension and the curved mirror suspension and at 0.66 Hz for the output mirror suspension due to the slightly different resonance frequencies at this suspension.

The gains of the damping filters were adjusted using OLG measurements and comparing them to the simulated OLG from the state space model. Increasing the gain was limited due to a saturation of the BOSEM coil output.

Figure 4.13 shows an OLG measurement of the south mirror suspension in longitudinal. Two different gain settings are displayed corresponding to the total gain of the MEDM filter bank. The filter gains are in arbitrary units, a gain of -1 is shown in red while the yellow line displays a filter gain of -0.75. The simulation from the state space model is shown in blue. This measurement was performed in order to make sure that the measurement matches the model. Since it was not possible to measure directly at high frequencies, a measurement was carried out at low frequencies. Based on the state space model, the assumption was made that the noise requirements are met at high frequencies. The filter gain was adjusted such that it matches the model at the highest unity gain frequency around 3 Hz. In this configuration, a filter gain of -0.75 is the best match to the model at the highest unity gain frequency.

Long Impulse Response

Mirror long motion
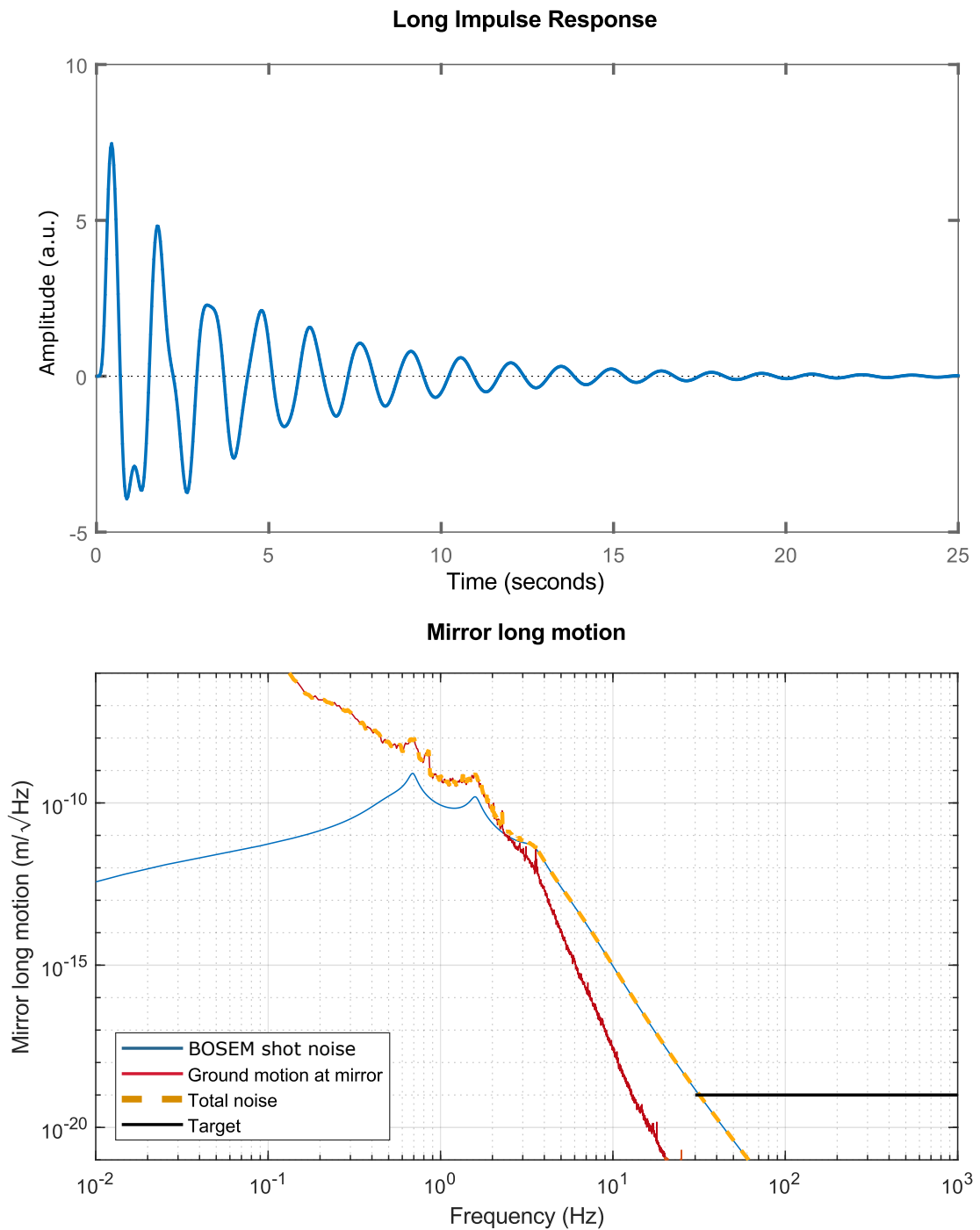
Figure 4.9: Noise projection of the BOSEMs for longitudinal suspension motion. The upper plot shows the simulated ring-down behavior of the suspensions after an impulse excitation, modeled with the state space model. The lower plot displays the noise contributions affecting the suspension motion, consisting of BOSEM noise (blue line) and seismic noise at the mirror (red line). The total noise is displayed in the yellow dashed line. It touches the target that was estimated for BOSEM noise from 30 Hz on (black line).
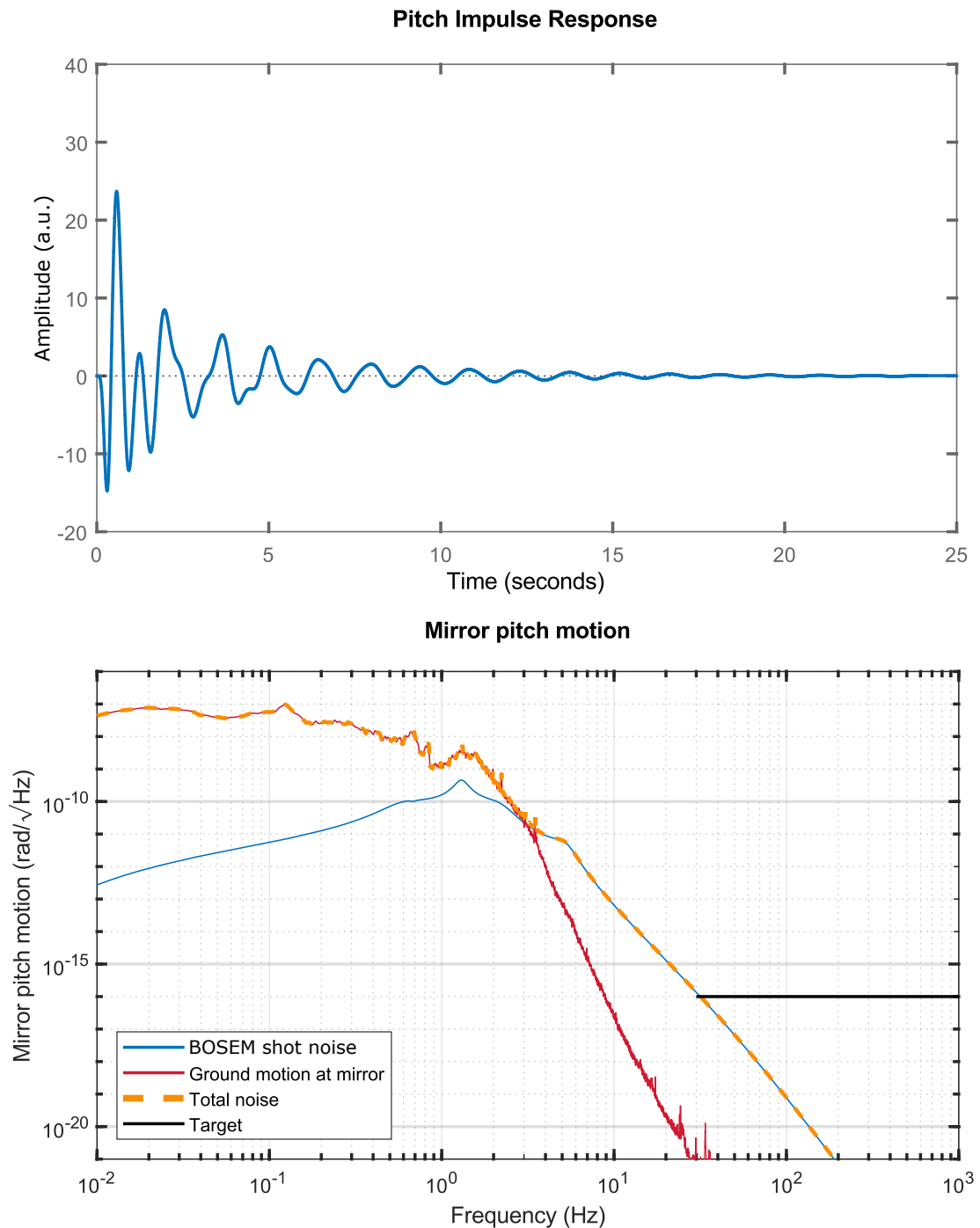
Figure 4.10: Noise projection of the BOSEMs for pitch suspension motion. The upper plot shows the simulated ring-down behavior of the suspensions after an impulse excitation, modeled with the state space model. The lower plot displays the noise contributions affecting the suspension motion, consisting of BOSEM noise (blue line) and seismic noise at the mirror (red line). The total noise is displayed in yellow. It touches the target that was estimated for BOSEM noise from 30 Hz on (black line).
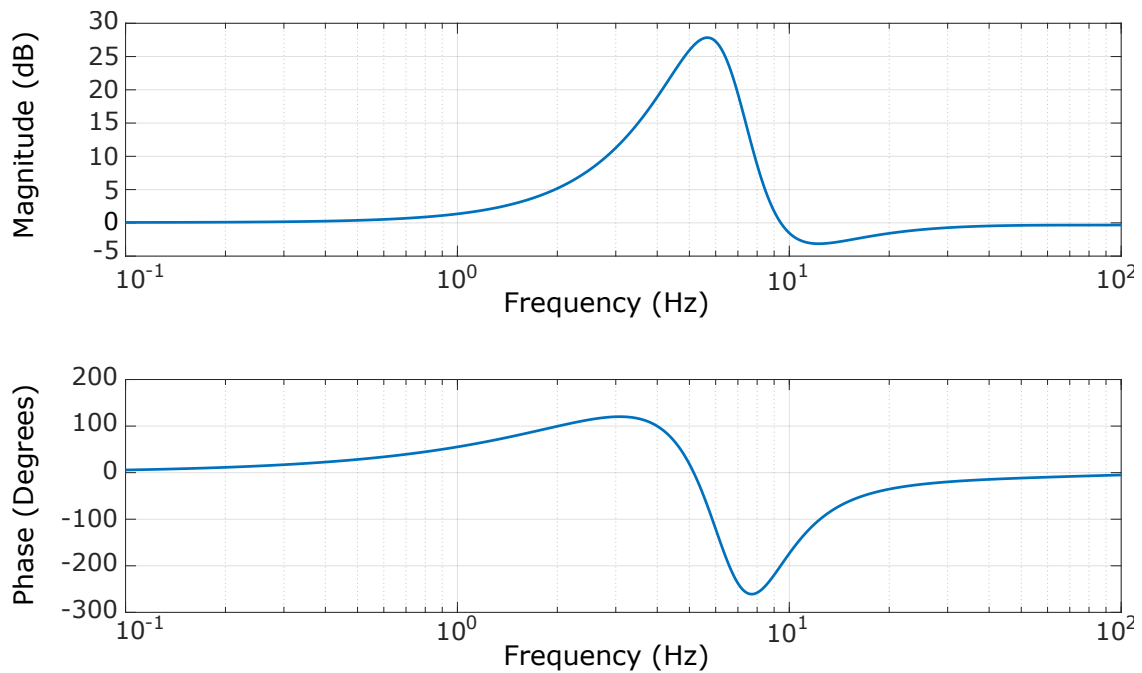
Figure 4.11: Bode plot of the longitudinal degree of freedom damping filter.

4.3.2 Results and Optimization

The longitudinal motion of the cavity mirrors and therefore the cavity length cause a variation of the laser frequency since this is locked to the frequency reference cavity. This frequency fluctuation is measured by the mode cleaner which is following the laser frequency.

Figure 4.14 shows the measured ASD of the mode cleaner feedback signal calibrated to equivalent displacement of the frequency reference cavity in case of the locked cavity without damping (green line) in comparison to a measurement with the initially implemented point-to-point damping at the three suspensions (blue line). Without damping, the noise performance is dominated by the longitudinal resonance frequencies at 0.64 Hz, 1.38 Hz and 2.54 Hz. The fundamental longitudinal resonance at 0.64 Hz has a displacement noise of approximately $2\,\mu\mathrm{m}/\sqrt{\mathrm{Hz}}$.

For these measurements, the cavity length motion was assumed to be equal to the optical table motion in y along the south arm. This is controlled by the SPI and calibrated in micrometers.

Figure 4.15 shows the measured ASD of the mode cleaner feedback signal calibrated to equivalent displacement of the frequency reference cavity in case of the locked cavity with the initial implemented point-to-point damping at the three suspensions (blue line) and the degree of freedom damping with the new implemented filters (red line). As a reference,
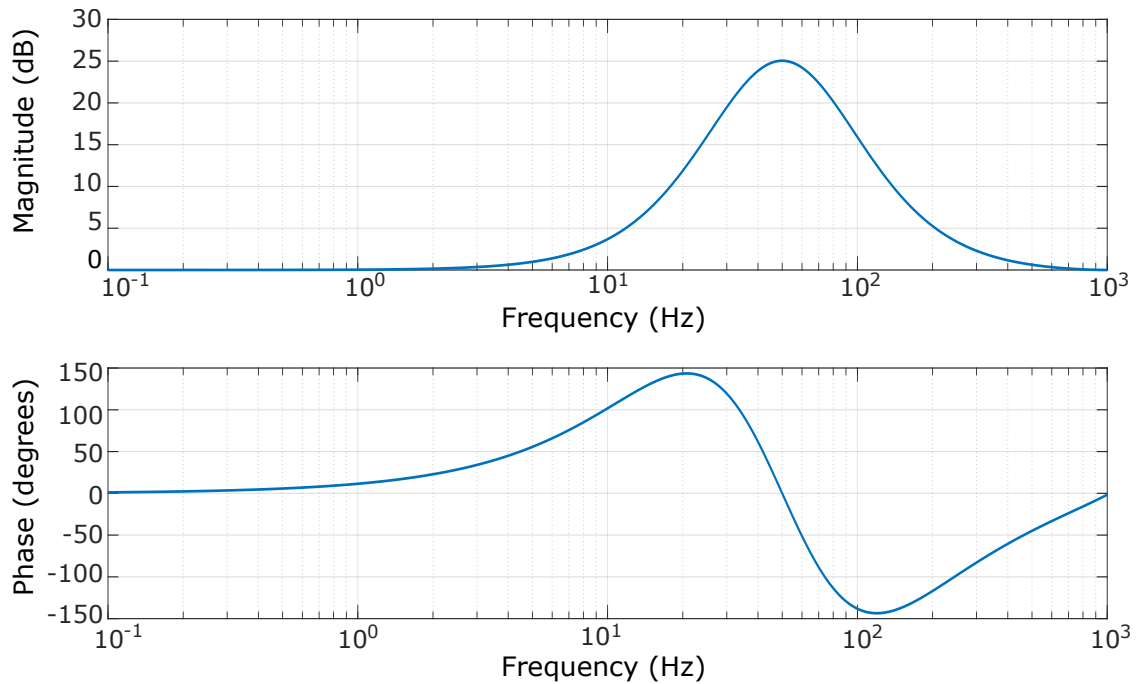
Figure 4.12: Bode plot of the degree of freedom damping filter for pitch, roll, side, vertical and yaw.

the noise performance of the mode cleaner stabilized to the free running laser is shown in the yellow line. At frequencies below 2 Hz the mode cleaner can be used as a sensor for these measurements. Above these frequencies the suspended reference cavity is quieter than the mode cleaner cavity.

With point-to-point damping the fundamental longitudinal resonance frequency could be suppressed down to 6×10^{-2} μm/$\sqrt{\text{Hz}}$. The new degree of freedom damping shows a suppression of this resonance peak down to approximately 2×10^{-2} μm/$\sqrt{\text{Hz}}$. This is further optimized with an implementation of resonant gains at the fundamental longitudinal resonance frequency of the suspensions. This is shown in figure 4.16. Different gain settings were tested before and optimized in order to get the best noise performance. The ASD of the mode cleaner feedback signal measured in the mode cleaner feedback control loop is shown for degree of freedom damping without resonant gains implemented (blue line) in comparison with resonant gains after an optimization of the individual gains (red line). This improved the performance of degree of freedom damping to 9×10^{-3} μm/$\sqrt{\text{Hz}}$. Further optimization of the damping performance was addressed by the implementation of global longitudinal cavity control at the frequency reference cavity suspensions and will be discussed in section 4.4.
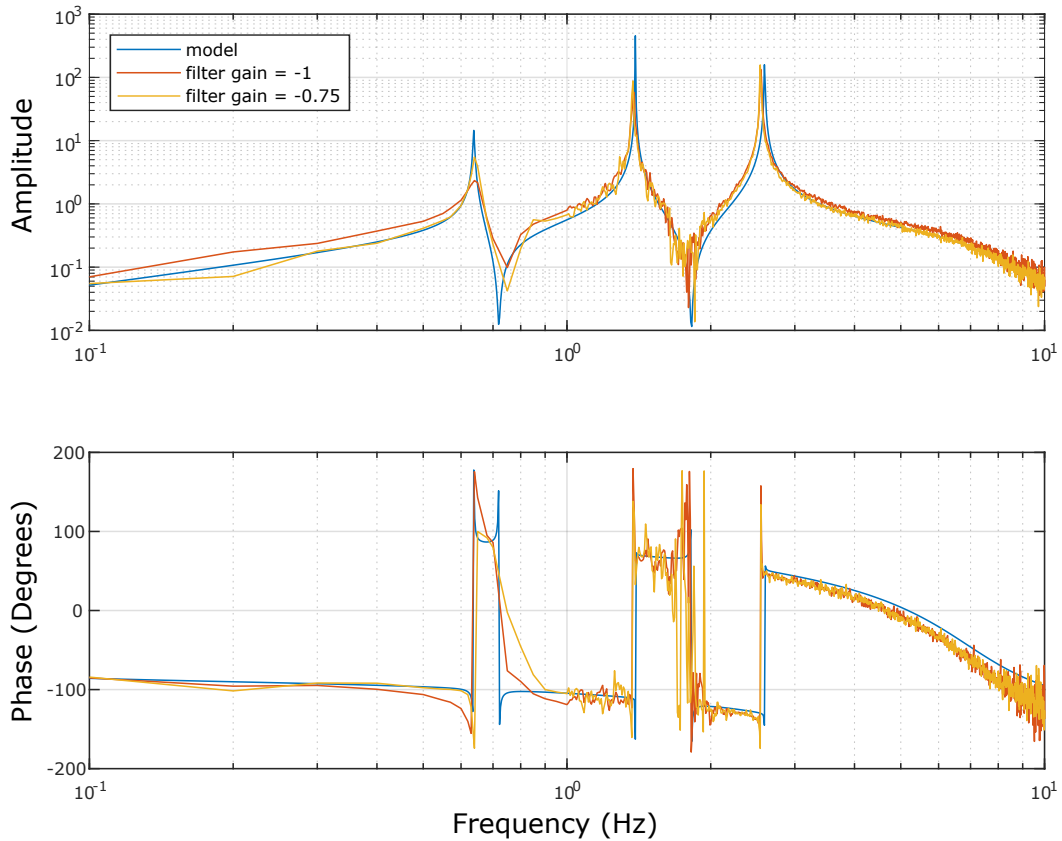
Figure 4.13: Open loop gain measurement of the south mirror suspension in longitudinal for two different gains in comparison to the state space model. Different gains were tested in order to find the optimal agreement to the model at the highest unity gain frequency of approximately 3 Hz. To save measurement time, the resolution at lower frequencies below 1 Hz is not optimized.

Efficiency of Damping - Ring-Down Measurements

The efficiency of damping was analyzed by the ring-down times of the suspensions after an impulse excitation at the top mass. The measurements were done for every frequency reference cavity suspension for different damping approaches. The excitation was applied to the BOSEMs at the top mass that control longitudinal motion and measured to the mode cleaner feedback signal. This gives information of the length of the frequency reference cavity. Assuming that the movement comes from the excited suspension, information about the individual longitudinal suspension motion is obtained. The data was band-pass filtered from 0.4 Hz with a second order high pass to 0.8 Hz with a second order low pass to only resolve the fundamental longitudinal resonance frequency.
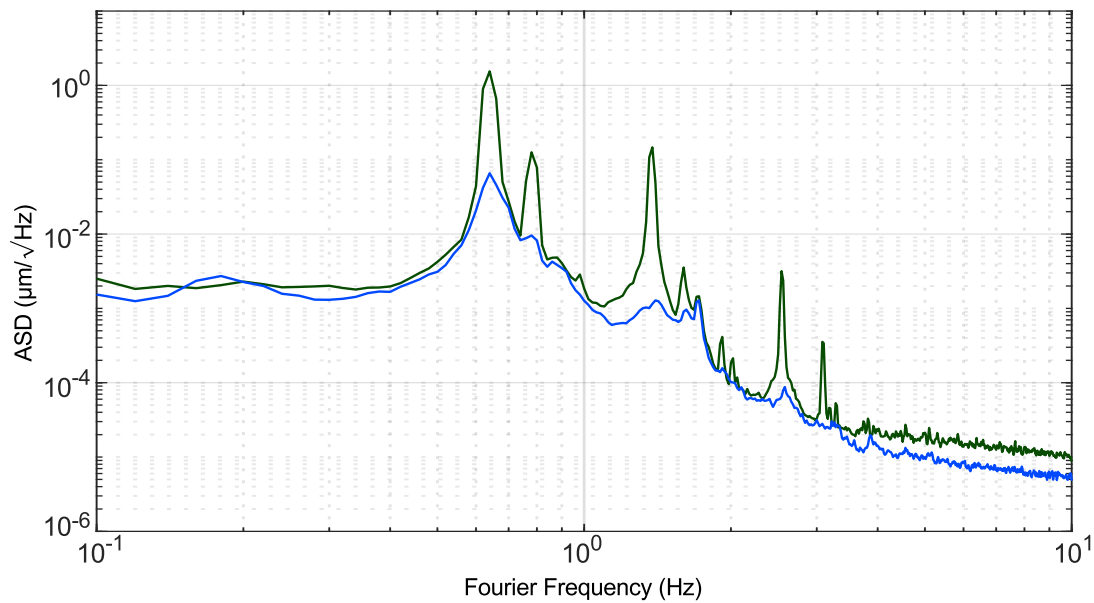
Figure 4.14: ASD of the mode cleaner piezo-electric transducer feedback signal measured in the mode cleaner control loop for undamped cavity suspensions (green line) and with point-to-point damping (blue line).

Figure 4.17 shows the ring-down times of the three frequency reference cavity suspensions after an excitation at the top mass in the longitudinal degree of freedom. The impulse response with the former point-to-point damping is shown in blue. In comparison the new implemented degree of freedom is shown in red. The suspensions were excited with the same amplitude for the measurements. Damping was applied for every measurement at all three suspensions. The degree of freedom damping includes the resonant gains at the fundamental longitudinal resonance frequency implemented for all suspensions.
The $1/e$-damping time for the curved mirror suspension with degree of freedom damping is 5.2 s. The $1/e$-damping time for point-to-point damping is significantly longer with 14.8 s. The measured $1/e$-damping time for the input mirror is 6.7 s for degree of freedom damping and 14 s for point-to-point damping. For the output mirror the $1/e$-damping time is 5.2 s for degree of freedom damping and 12.6 s for point-to-point damping.
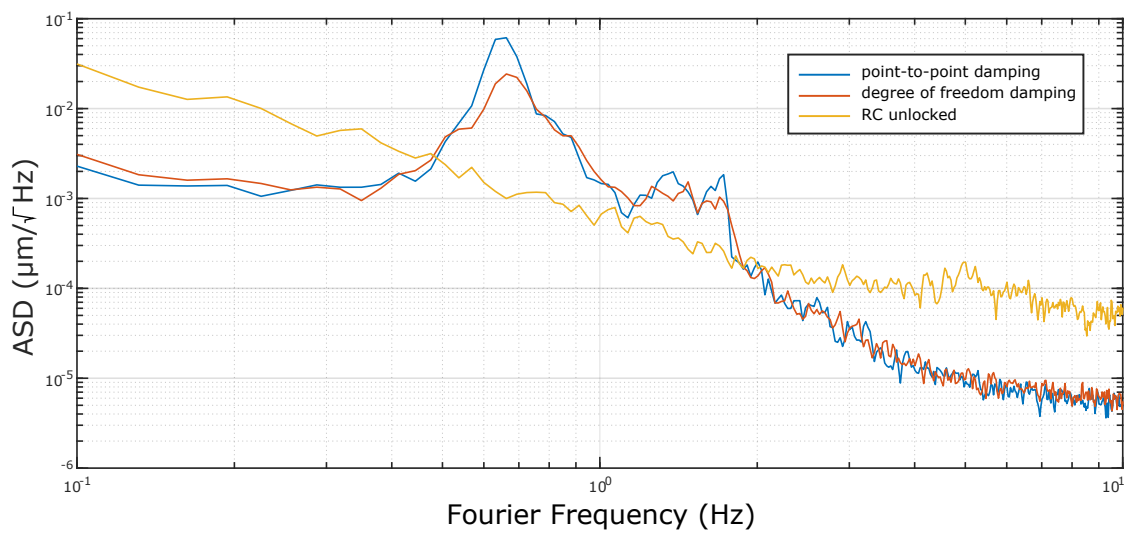
Figure 4.15: ASD of the mode cleaner feedback signal measured in the mode cleaner control loop with point-to-point damping at the frequency reference cavity suspensions (blue line) in comparison to degree of freedom damping with the new filters (red line). The noise performance of the mode cleaner locked to the free running laser is shown in the yellow. Degree of freedom damping reduces the fundamental resonance frequency at $0.64\,\mathrm{Hz}$ down to approximately $2 \times 10^{-2}\,\mathrm{\mu m}/\sqrt{\mathrm{Hz}}$.
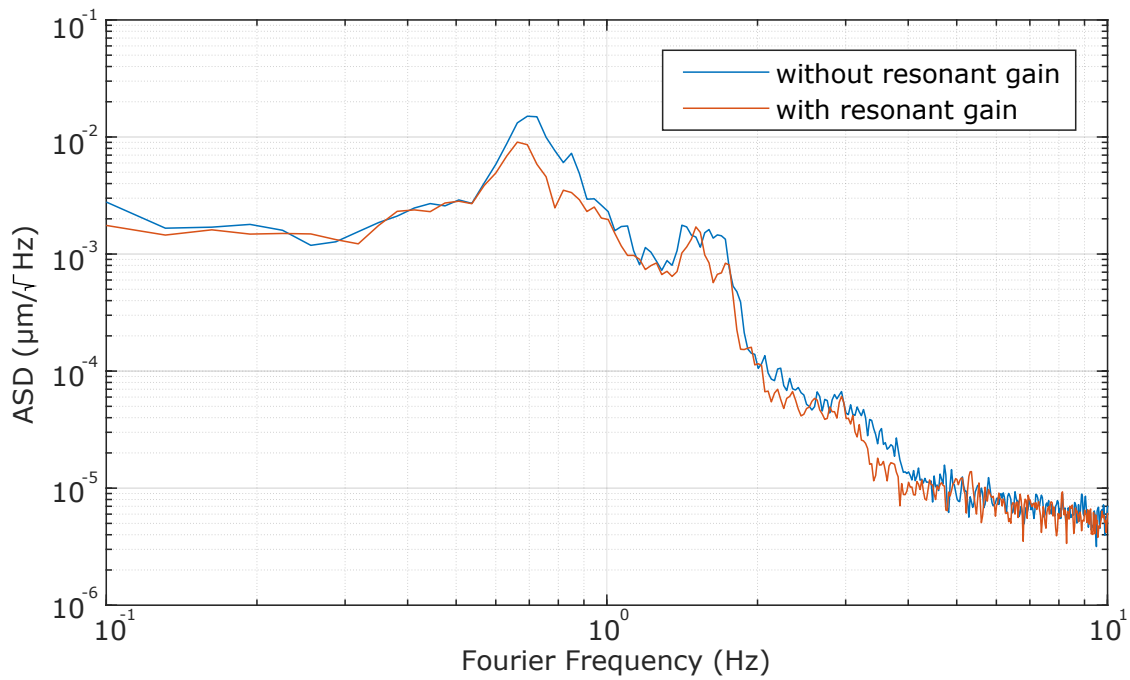
Figure 4.16: Resonant gain optimization for degree of freedom damping at the frequency reference cavity suspensions. The ASD of the mode cleaner feedback signal measured in the mode cleaner feedback loop is shown for degree of freedom damping at the suspensions with and without resonant gains implemented at the fundamental longitudinal resonance frequency. The blue line shows the measured ASD for degree of freedom damping only. The red line shows the situation after the implementation of a resonant gain at all three suspensions. The individual gains were optimized in order to find the best damping performance. They are implemented for all degrees of freedom at $0.64\,\mathrm{Hz}$ for the input mirror suspension and the curved mirror suspension and at $0.66\,\mathrm{Hz}$ for the output mirror suspension.
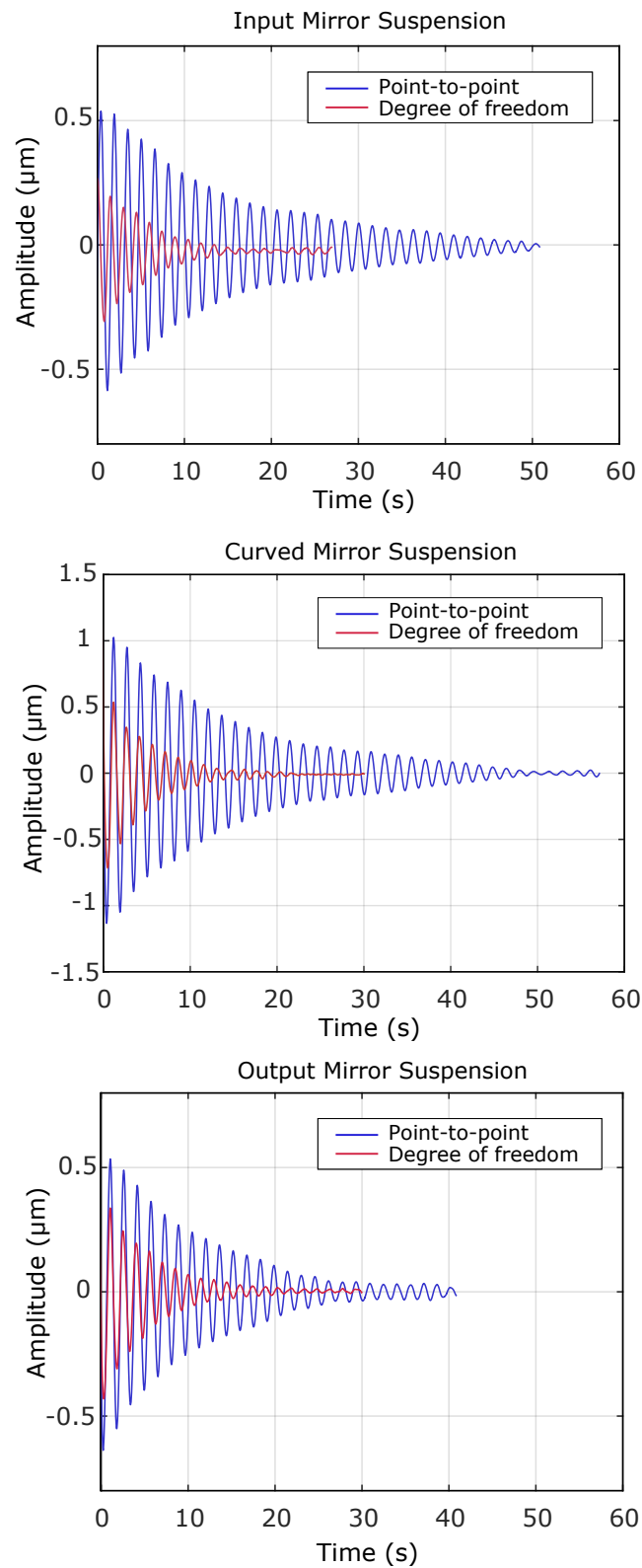
Figure 4.17: Measurement of suspension ring-down time after an excitation at the top mass in longitudinal for point-to-point damping (blue) in comparison to degree of freedom damping (red).

4.4 Global Longitudinal Cavity Control

The implementation of degree of freedom damping with the new damping filters was able to reduce the peak height in the power spectrum of the mode cleaner cavity feedback to the laser when locking it to the frequency reference cavity by one order of magnitude, to $10^{-2}\,\mu\mathrm{m}/\sqrt{\mathrm{Hz}}$. Raising the overall gain too much was driving the damping loop instable. A re-shaping of the feedback control loop for gaining stability was not realized since the requirements at higher frequencies in the SQL sensitivity band around 200 Hz had to be met at the same time.

An additional active control loop to further suppress the fundamental longitudinal resonance was implemented. The mode cleaner cavity feedback signal is fed back to the curved mirror of the frequency reference cavity to control its longitudinal motion. The laser frequency is stabilized to the frequency reference cavity length. At frequencies below 2 Hz the free running laser provides better frequency stability than the suspended cavity. The mode cleaner cavity provides a more stable frequency reference than the free running laser. It is used to stabilize the suspended frequency reference cavity and hence the laser.

The principle is shown in figure 4.4 and in section 4.1.2 when global longitudinal cavity control was introduced. The feedback signal of the mode cleaner due to the frequency variation is modified by the global longitudinal control damping filter and fed back to the curved mirror of the frequency reference cavity to control its longitudinal motion and therefore the cavity length.

An overview about the control loops of the mode cleaner cavity, the frequency reference cavity and the global longitudinal cavity length control are shown in figure 4.18. For realization of global longitudinal control the mode cleaner signal is fed back to the south suspension including the damping filter. The filter design was based on the corresponding longitudinal transfer function of the south suspension that was measured in a previous measurement. Global longitudinal cavity control using the mode cleaner may introduce more cavity motion in general, but this is motion of all cavity mirrors in common while the cavity length stays constant.

4.4.1 Results

Figure 4.19 shows the ASD of the mode cleaner piezo-electric transducer feedback signal measured in the mode cleaner feedback control loop to the laser while this is locked to the frequency reference cavity.

The measurement was taken for three cases; the former point-to-point damping of the frequency reference cavity suspensions, the new degree of freedom damping with resonant gains and for global longitudinal cavity control together with degree of freedom damping at all suspensions. Resonant gains were implemented for all suspensions and for all degrees of freedom; at 0.64 Hz for the input mirror and curved mirror and at 0.66 Hz for the output mirror suspension.
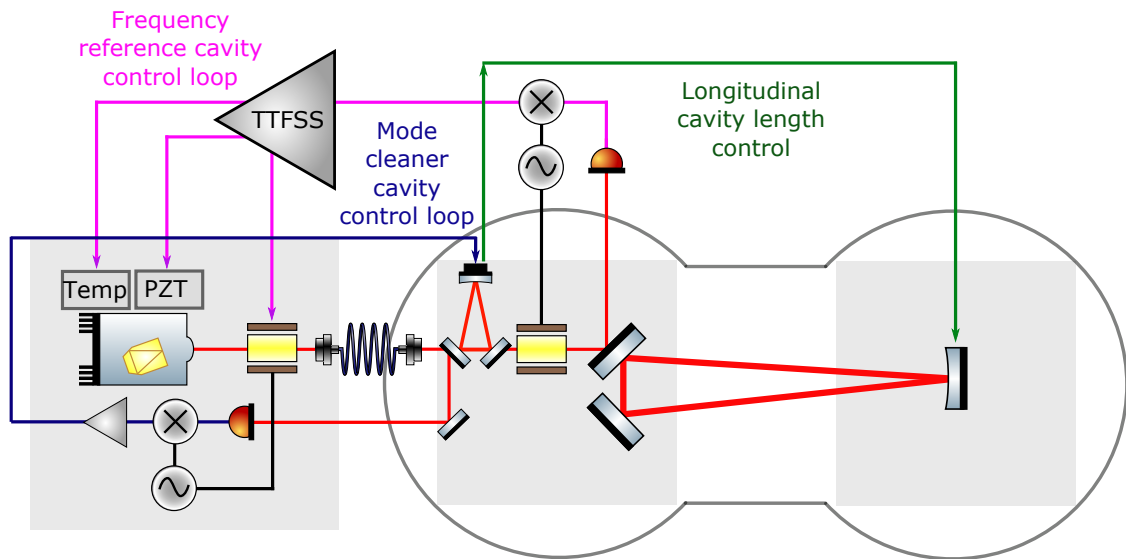
Figure 4.18: Overview of the control loops for the mode cleaner cavity (blue), the frequency reference cavity (magenta) and the longitudinal cavity length control (green).

While with point-to-point damping the first longitudinal resonance at $0.64\,\mathrm{Hz}$ appears with $7 \times 10^{-2}\,\mu\mathrm{m}/\sqrt{\mathrm{Hz}}$, the new degree of freedom damping reduces the resonance peak already to $2 \times 10^{-2}\,\mu\mathrm{m}/\sqrt{\mathrm{Hz}}$. With global longitudinal control of the frequency reference cavity this fundamental resonance peak is suppressed down to approximately $2 \times 10^{-3}\,\mu\mathrm{m}/\sqrt{\mathrm{Hz}}$. At frequencies below the first resonance, the damping performance is degraded with global longitudinal control. Additional investigation and optimization of the damping filter is required for longterm stable operation.

Since global longitudinal cavity control at the frequency reference cavity uses the mode cleaner signal in a feedback loop, which serves as an in-loop sensor now, another out-of-loop sensor was required for the measurements. The SAT which is locked to the laser serves as the out-of-loop sensor.

The aforementioned measurements were repeated with the locked SAT feedback signal being used as an out-of-loop sensor. The frequency reference cavity suspensions were damped with point-to-point damping, degree of freedom damping and with global longitudinal control.

The results are shown in figure 4.20. The first resonance frequency of the SAT suspensions is at $0.74\,\mathrm{Hz}$. The other resonance peaks at higher frequencies, which are not visible in the former measurement with the mode cleaner as a sensor, are also pendulum modes of the SAT suspensions. Only the second longitudinal resonance frequency of the frequency reference cavity at $1.38\,\mathrm{Hz}$ is visible in the power spectrum.

With point-to-point damping the 0.64 Hz resonance is strongly visible in the SAT feedback signal while degree of freedom damping already suppresses the peak by one order of magnitude. The global longitudinal control suppresses the fundamental resonance to such an extent that it no longer occurs in the SAT feedback signal.

Improving low frequency performance

The first measurements with global longitudinal cavity control at the frequency reference cavity suspensions showed that it suppressed well the fundamental longitudinal resonance at 0.64 Hz but increased noise at lower frequencies below 0.5 Hz. Further investigation and optimization of the filter would be required to improve the low frequency performance without decreasing performance at other frequencies or rendering the loop unstable. As a preliminary test to show that the increased frequency noise was due to noise being fed back and added to the mirror via feedback with the servo, a notch at lower frequencies was implemented. This allows a suppression of the suspension motion without losing too much phase margin which would turn the control loop unstable.

Figure 4.21 shows the ASD of the mode cleaner piezo-electric transducer feedback signal measured in the mode cleaner feedback control loop. The measurement was done for all suspensions damped in degree of freedom damping mode without global longitudinal control, with global longitudinal cavity control but no notch and with global control with an additional notch at low frequencies. The notch was implemented at 0.15 Hz with a quality factor (Q-factor) of 5 and a depth of 100 dB. At this frequency, the measured ASD of the mode cleaner piezo-electric transducer feedback signal for global longitudinal control was improved to the performance of degree of freedom damping. This shows, that in principle the performance of the global longitudinal control can be improved at lower frequencies but experimental implementation of the improvements require additional investigations.

The implementation of the global longitudinal control was a first proof of principle experiment and showed a significant improvement of the frequency reference cavity damping performance. The long term stability needs to be tested and further improved, especially at lower frequencies i.e. below the first fundamental resonance frequency of the suspensions. At frequencies below 0.5 Hz the noise is increased in comparison to degree of freedom damping. This first implementation of the global longitudinal control of the cavity does not run permanently, but can be switched on as an amplifier stage when more damping performance is required. For this, the status and the performance of the AEI-SAS and the SPI need to be in a well known and controlled state. Additionally, the current filter design is not optimized in terms of stability. The limited phase margin indicates the filter being close to unstable and is therefore not switched on permanently. A solution for permanent longitudinal cavity control could be the implementation of a control and monitoring system.

In a final configuration, the shape of the damping filter needs to be optimized such that no noise is introduced at higher frequencies and the requirements in the SQL sensitivity band
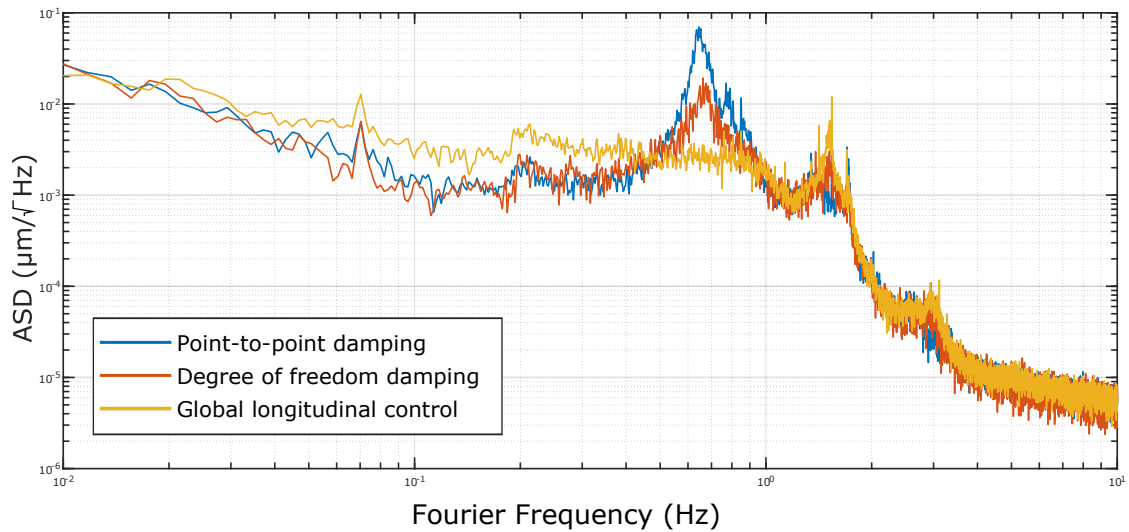
Figure 4.19: ASD of the mode cleaner piezo-electric transducer feedback signal measured in the mode cleaner feedback control loop to the laser while this is stabilized to the frequency reference cavity. The power spectra are taken for different damping methods of the frequency reference cavity suspensions. The blue line shows the former point-to-point damping. The fundamental longitudinal resonance at $0.64\,\text{Hz}$ is clearly dominating the spectrum. Degree of freedom damping with the new filters, shown in the red line, suppresses the resonance peak already to $2 \times 10^{-2}\,\mu\text{m}/\sqrt{\text{Hz}}$. Global longitudinal control improves the performance further and reduces the resonance peak down to approximately $2 \times 10^{-3}\,\mu\text{m}/\sqrt{\text{Hz}}$, shown in the yellow line.

are still met.
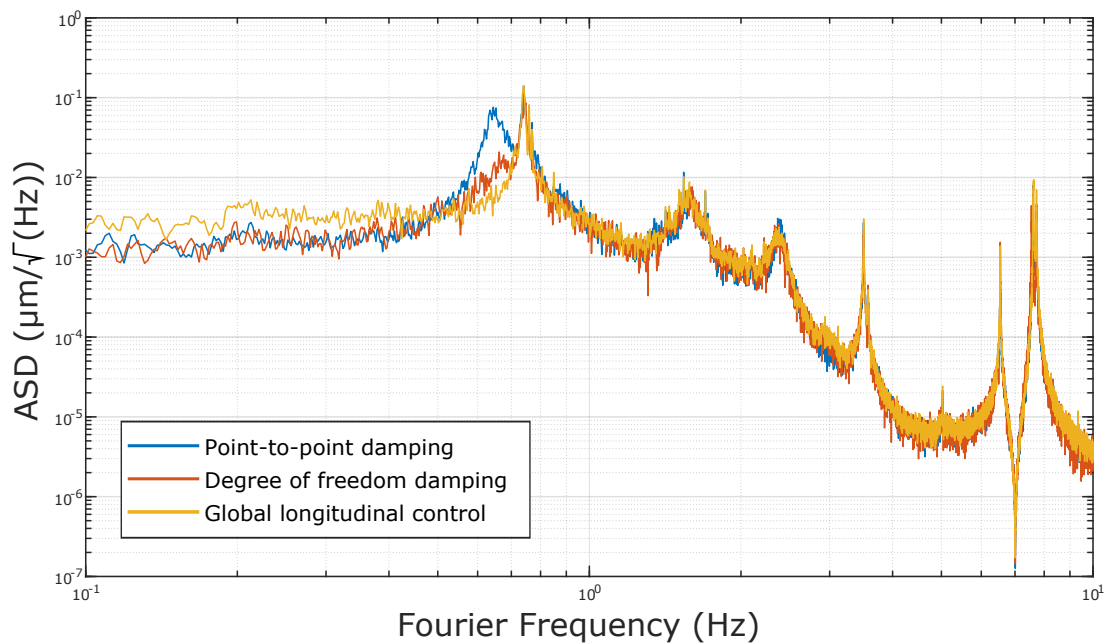
Figure 4.20: ASD of the mode cleaner piezo-electric transducer feedback signal measured in the SAT feedback loop to the laser while while this is stabilized to the frequency reference cavity. Since global longitudinal control of the frequency reference cavity uses the mode cleaner in the control loop, the SAT was used as an out-of-loop sensor. The resonance at 0.74 Hz originates from the SAT suspensions as well as the resonance peaks at higher frequencies. With point-to-point damping the fundamental longitudinal resonance frequency of the frequency reference cavity is dominating the SAT power spectrum (blue line). With degree of freedom damping, shown in the red line, the resonance is significantly reduced. With global longitudinal cavity control (yellow line) the frequency reference cavity resonance at 0.64 Hz is not visible in the SAT power spectrum.
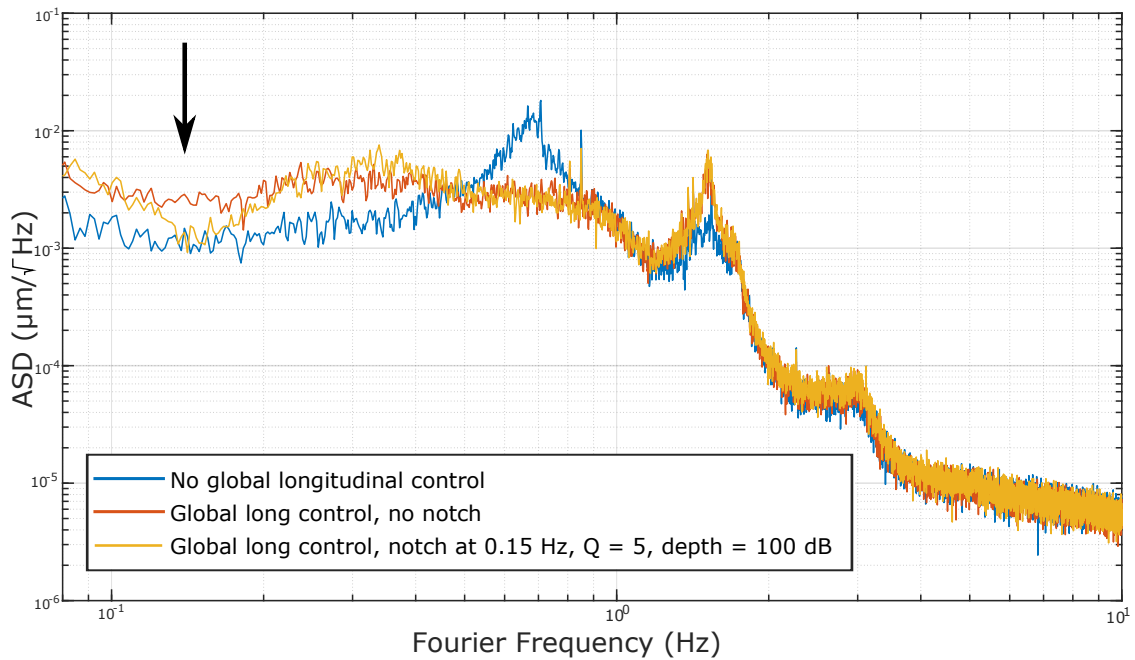
Figure 4.21: Implementation of a notch as a test to improve the low frequency performance of the frequency reference cavity global longitudinal cavity control. The ASD of the mode cleaner feedback signal was measured in the mode cleaner control loop for different damping states of the cavity suspensions. The ASD measured with only degree of freedom damping without global longitudinal cavity control is shown for comparison (blue line). Global longitudinal control (red line) shows, that the fundamental resonance peak at $0.64\,\mathrm{Hz}$ can be sufficiently suppressed down to a level of $2 \times 10^{-3}\,\mu\mathrm{m}/\sqrt{\mathrm{Hz}}$ but it also increases the noise at frequencies below $0.5\,\mathrm{Hz}$. With a notch implemented in the damping filter at low frequencies, in this case at $0.15\,\mathrm{Hz}$, the damping performance can be improved to the same level as the performance with degree of freedom damping, plotted as the yellow line.

CHAPTER 5

Summary and Outlook

The scope of this thesis was the laser frequency stabilization at the AEI 10 m Prototype. To achieve the required sensitivity for the sub-SQL interferometer, extreme stability of the laser source is needed. A triangular suspended cavity was assembled and installed in the vacuum system, distributed on two seismically isolated optical benches, resulting in an optical roundtrip length of 21.2 m. The purpose of this cavity is to provide a stable length reference to which the frequency of the 35 W main laser is stabilized. A feedback control loop is used to read out the frequency noise of the free running laser, compare it to the cavity length and provide the error signal. This is achieved with a PDH sensing scheme in reflection of the frequency reference cavity. An analog servo, the TTFSS from aLIGO, is used to process the error signal into feedback signals for the actuators. Three different actuators are used to cover a wide frequency range from DC to 100 MHz. The control loop has a unity gain frequency of 300 kHz. A slow temperature control loop is implemented for frequencies below 1 Hz, frequencies between 1 Hz and 10 kHz are controlled by a piezoelectric transducer and frequencies above 10 kHz are covered by an EOM.

The laser frequency noise of the free running NPRO is $100\,\mathrm{Hz}/\sqrt{\mathrm{Hz}}$ at 100 Hz. The requirements for frequency noise suppression of the free running laser are $10^{-4}\,\mathrm{Hz}/\sqrt{\mathrm{Hz}}$ at 20 Hz decreasing to below $10^{-6}\,\mathrm{Hz}/\sqrt{\mathrm{Hz}}$ at 1 kHz. This corresponds to a suppression of 140 dB at 100 Hz. The measured gain of the frequency stabilization control loop is 110 dB at 100 Hz. Achieving the final gain configuration of the stabilization loop is part of future improvements.

Angular drifts and misalignment of the frequency reference cavity was compensated by the implementation of an auto-alignment system. Angular sensing of the cavity mirrors is provided by differential wavefront sensing, in which the reflected cavity light is sensed by two wavefront sensors separated by a Gouy phase of approximately 90°. A motorized spot-centering system was implemented to keep the laser beams centered on the wavefront sensors and increases the sensing range by ensuring a centered beam on the WFS. The information about angular beam misalignments in pitch and yaw is processed and sent to the two suspended steering mirrors in front of the frequency reference cavity to automatically control the input beam into the cavity.

The cavity optics are suspended as triple pendulums to provide passive seismic isolation above their fundamental resonance frequencies. Low-frequency mirror motions are re-

quired to be reduced, as they can induce noise at higher frequencies. Seismic motion is amplified at pendulum resonances between 0.5 Hz and 10 Hz, while the isolation behavior of the suspensions is optimal in the SQL measurement frequency range around 200 Hz.

To improve the low-frequency performance at the resonance frequencies active damping is applied in a feedback control loop. Optical sensing and control of the mirror motion is applied by BOSEMs locally at the top mass of each suspension. The control loops have been optimized by designing and implementing digital damping filters. The motion is sensed in all degrees of freedom and fed back to the BOSEMs controlling these degrees of freedom. The filters required for these control loops were designed based on simulations of the suspensions carried out previously by using a state space model.

The implementation of the new degree of freedom damping filters suppressed the mirror motion at the fundamental longitudinal resonance frequency at 0.64 Hz from $2\,\mu\mathrm{m}/\sqrt{\mathrm{Hz}}$ for an undamped suspension to $2 \times 10^{-2}\,\mu\mathrm{m}/\sqrt{\mathrm{Hz}}$.

Further suppression of the fundamental longitudinal resonance was achieved by developing and implementing a new stabilization concept for active cavity length control. The laser is stabilized to the frequency reference cavity length, while the mode cleaner cavity length is stabilized to the laser. The free-running laser offers better frequency stability at frequencies below 2 Hz than the suspended cavity. The rigid mode cleaner cavity provides a more stable frequency reference than the free running laser and is used to stabilize the suspended frequency reference cavity and hence the laser. The mode cleaner feedback signal is fed back to the curved mirror of the frequency reference cavity to actively control the cavity length. This new concept of cavity length control further reduced the mirror motion at 0.64 Hz to $2 \times 10^{-3}\,\mu\mathrm{m}/\sqrt{\mathrm{Hz}}$.

Measurements with the SAT as out-of-loop sensor showed that the fundamental longitudinal resonance was sufficiently suppressed not to disturb the measurements of the SAT.

Outlook

The optimization of the frequency reference cavity stabilization loop is part of further improvements to achieve the 140 dB frequency noise suppression target at 100 Hz. This can be realized by increasing the optical input power to achieve a shot noise limited performance of the frequency reference cavity. The electronics in the control loop can be optimized to achieve a higher loop gain. This also includes the improvement of the locking photodiode and the TTFSS.

Conclusion

In conclusion, this thesis has shown that damping of the frequency reference cavity suspensions works reliably and is able to sufficiently reduce the fundamental resonance frequency for the operation of the sub-SQL interferometer. The auto-alignment system provides automated angular alignment of the cavity and enables lock maintenance due to

an aligned cavity mode. The frequency reference cavity commissioned in this thesis is able to run reliably and permanently.

Bibliography

[Aas15]   AASI, J. et al.: 'Advanced LIGO'. *Classical and Quantum Gravity* (Mar. 2015), vol. 32(7): p. 074001 (cit. on pp. 1, 16, 24, 25).

[Aba11]   ABADIE, J., B. P. ABBOTT, R. ABBOTT, T. D. ABBOTT, M. ABERNATHY, C. ADAMS, R. ADHIKARI, C. AFFELDT, B. ALLEN, G. S. ALLEN, et al.: 'A gravitational wave observatory operating beyond the quantum shot noise limit'. *Nature Physics* (2011), vol. 7: pp. 962–965 (cit. on p. 27).

[Abb16]   ABBOTT, B. P. et al.: 'Observation of Gravitational Waves from a Binary Black Hole Merger'. *Physical Review Letters* (Feb. 2016), vol. 116(6) (cit. on pp. e, g, 1).

[Abr12]   ABRAMOVICI, A. and J. CHAPSKY: *Feedback Control Systems A Fast Track Guide for Scientists and Engineers*. Berlin Heidelberg: Springer Science & Business Media, 2012 (cit. on p. 53).

[Ace14]   ACERNESE, F. et al.: 'Advanced Virgo: a second generation interferometric gravitational wave detector'. *Classical and Quantum Gravity* (Dec. 2014), vol. 32(2): p. 024001 (cit. on pp. 24, 26).

[Aff14a] AFFELDT, C., K. DANZMANN, K. L. DOOLEY, H. GROTE, M. HEWITSON, S. HILD, J. HOUGH, J. LEONG, H. LÜCK, M. PRIJATELJ, S. ROWAN, A. RÜDIGER, R. SCHILLING, R. SCHNABEL, E. SCHREIBER, B. SORAZU, K. A. STRAIN, H. VAHLBRUCH, B. WILLKE, W. WINKLER, and H. WITTEL: 'Advanced techniques in GEO 600'. *Classical and Quantum Gravity* (2014), vol. 31(22): p. 224002 (cit. on p. 27).

[Aff14b] AFFELDT, CHRISTOPH: 'Laser Power Increase in GEO 600, Commissioning aspects towards an operation of GEO 600 at high laser power'. PhD thesis. Leibniz Universität Hannover, 2014 (cit. on pp. 24, 26, 28).

[Ast11]   ASTON, STUART MARK: 'Optical Read–out Techniques for the Control of Test masses in Gravitational Wave Observatories'. PhD thesis. University of Birmingham, Jan. 2011 (cit. on pp. 40, 42, 49, 71, 84).

[Ber17]   BERGMANN, G., C. M. MOW-LOWRY, V. B. ADYA, A. BERTOLINI, M. M.
          HANKE, R. KIRCHHOFF, S. M. KÖHLENBECK, G. KÜHN, P. OPPERMANN, A.
          WANNER, T. WESTPHAL, J. WÖHLER, D. S. WU, H. LÜCK, K. A. STRAIN,
          and K. DANZMANN: 'Passive-performance, analysis, and upgrades of a 1-ton
          seismic attenuation system'. *Classical and Quantum Gravity* (Feb. 2017), vol.
          34(6): p. 065002 (cit. on pp. 1, 12).

[Ber18]   BERGMANN, GERALD: 'Improving the seismic isolation for the AEI 10 m
          prototype'. eng. PhD thesis. Leibniz Universität Hannover, 2018 (cit. on pp. 1,
          12).

[Bla01]   BLACK, ERIC D.: 'An introduction to Pound–Drever–Hall laser frequency
          stabilization'. *American Journal of Physics* (Jan. 2001), vol. 69(1): pp. 79–87
          (cit. on pp. 2, 19).

[Bon02]   BONDU, F., A. BRILLET, F. CLEVA, H. HEITMANN, M. LOUPIAS, C. N.
          MAN, H. TRINQUET, and the VIRGO COLLABORATION: 'The VIRGO injec-
          tion system'. *Classical and Quantum Gravity* (Mar. 2002), vol. 19(7): pp. 1829–
          1833 (cit. on p. 26).

[Bon96]   BONDU, F., P. FRITSCHEL, C. N. MAN, and A. BRILLET: 'Ultrahigh-spectral-
          purity laser for the VIRGO experiment'. *Optics Letters* (Apr. 1996), vol. 21(8):
          p. 582 (cit. on p. 26).

[Bro99]   BROZEK, OLIVER SASCHA: 'Frequenzstabilisierung eines Nd YAG Hochleis-
          tungs Laser Systems für den Gravitationswellendetektor GEO 600'. PhD thesis.
          Universität Hannover, 1999 (cit. on p. 27).

[Dah12]   DAHL, K., G. HEINZEL, B. WILLKE, K. A. STRAIN, S. GOSSLER, and K.
          DANZMANN: 'Suspension platform interferometer for the AEI 10 m prototype
          concept, design and optical layout'. *Classical and Quantum Gravity* (2012),
          vol. 29(9): p. 095024 (cit. on pp. 1, 13).

[Dah13]   DAHL, KATRIN: 'From design to operation a suspension platform interferom-
          eter for the AEI 10 m prototype'. PhD thesis. Leibniz Universität Hannover,
          2013 (cit. on pp. 1, 13).

[Dan12]   DANILISHIN, STEFAN L. and FARID YA. KHALILI: 'Quantum Measurement
          Theory in Gravitational Wave Detectors'. *Living Reviews in Relativity* (Apr.
          2012), vol. 15(1): p. 5 (cit. on p. 3).

[Eic03]   EICHENFIELD, MATT: *Modelling and Commissioning the Wavefront Sensing
          Auto-Alignment System of a Triangular Mode Cleaner Cavity*. LIGO Document
          Control Center. LIGO-T030234- 00- D. 2003 (cit. on p. 64).

[Ein16]   EINSTEIN, A.: 'Näherungsweise Integration der Feldgleichungen der Gravita-
          tion'. *Sitzungsberichte der Königlich Preußischen Akademie der Wissenschaften
          (Berlin), Seite 688-696.* (1916), vol. (cit. on pp. e, g).

[Ell05]   ELLIFFE, E. J., J. BOGENSTAHL, A. DESHPANDE, J. HOUGH, C. KILLOW, S. REID, D. ROBERTSON, S. ROWAN, H. WARD, and G. CAGNOLI: 'Hydroxide-catalysis bonding for stable optical systems for space'. *Classical and Quantum Gravity* (2005), vol. 22(10): S257 (cit. on p. 13).

[Fre07]   FREDE, MAIK, BASTIAN SCHULZ, RALF WILHELM, PATRICK KWEE, FRANK SEIFERT, BENNO WILLKE, and DIETMAR KRACHT: 'Fundamental mode, single-frequency laser amplifier for gravitational wave detectors'. *Opt. Express* (Jan. 2007), vol. 15(2): pp. 459–465 (cit. on p. 19).

[Fri12]   FRIEDLAND, BERNARD: *Control System Design An Introduction to State-Space Methods*. Dover Publications, 2012 (cit. on p. 82).

[Goß10]   GOSSLER, S., A. BERTOLINI, M. BORN, Y. CHEN, K. DAHL, D. GERING, C. GRÄF, G. HEINZEL, S. HILD, F. KAWAZOE, O. KRANZ, G. KÜHN, H. LÜCK, K. MOSSAVI, R. SCHNABEL, K. SOMIYA, K. A. STRAIN, J. R. TAYLOR, A. WANNER, T. WESTPHAL, B. WILLKE, and K. DANZMANN: 'The AEI 10 m prototype interferometer'. *Classical and Quantum Gravity* (Apr. 2010), vol. 27(8): pp. 084023+ (cit. on pp. 1, 4, 8).

[Grä13]   GRÄF, CHRISTIAN: 'Optical Design and Numerical Modeling of the AEI 10m Prototype sub-SQL Interferometer'. PhD thesis. Leibniz Universität Hannover, 2013 (cit. on pp. 7, 16).

[Gro03]   GROTE, HARTMUT: 'Making it Work: Second Generation Interferometry in GEO 600!' PhD thesis. Universität Hannover, 2003 (cit. on pp. 26–28).

[Hal]   HALL, EVAN: 'Laser Frequency and Intensity Stabilization for Advanced LIGO'. (), vol. (cit. on pp. 25, 27).

[Har10]   HARRY, GREGORY M. and the LIGO SCIENTIFIC COLLABORATION: 'Advanced LIGO: the next generation of gravitational wave detectors'. *Classical and Quantum Gravity* (2010), vol. 27(8): p. 084006 (cit. on p. 1).

[Jun16]   JUNKER, JONAS: 'Laser Power Stabilization for the AEI 10m Prototype'. MA thesis. Leibniz Universität Hannover, 2016 (cit. on pp. 1, 21).

[Jun17]   JUNKER, JONAS, PATRICK OPPERMANN, and BENNO WILLKE: 'Shot-noise-limited laser power stabilization for the AEI 10m Prototype interferometer'. *Opt. Lett.* (Feb. 2017), vol. 42(4): pp. 755–758 (cit. on pp. 1, 19–21).

[Kaw10]   KAWAZOE, FUMIKO, JOHN ROBERT TAYLOR, ALESSANDRO BERTOLINI, MICHAEL BORN, YANBEI CHEN, KATRIN DAHL, DANIEL GERING, STEFAN GOSSLER, CHRISTIAN GRÄF, GERHARD HEINZEL, STEFAN HILD, OLIVER KRANZ, GERRIT KÜHN, HARALD LÜCK, KASEM MOSSAVI, ROMAN SCHNABEL, KENTARO SOMIYA, KENNETH STRAIN, ALEXANDER WANNER, TOBIAS WESTPHAL, BENNO WILLKE, and KARSTEN DANZMANN: 'Designs

of the frequency reference cavity for the AEI 10 m Prototype interferometer'. *Journal of Physics: Conference Series* (May 2010), vol. 228: p. 012028 (cit. on pp. 2, 21, 23, 29, 31, 34, 35, 62).

[Koe18]   KOEHLENBECK, SINA: 'Towards the SQL Interferometer Length Stabilization at the AEI 10m-Prototype'. PhD thesis. Leibniz Universität Hannover, 2018 (cit. on pp. 1, 7, 13–15).

[Kog66]   KOGELNIK, H. and T. LI: 'Laser Beams and Resonators'. *Applied Optics* (Oct. 1966), vol. 5(10): p. 1550 (cit. on pp. 7, 30).

[Kwe12]   KWEE, P., C. BOGAN, K. DANZMANN, M. FREDE, H. KIM, P. KING, J. P OLD, O. PUNCKEN, R. L. SAVAGE, F. SEIFERT, P. WESSELS, L. WINKEL-MANN, and B. WILLKE: 'Stabilized high-power laser system for the gravitational wave detector advanced LIGO'. *Optics Express* (Apr. 2012), vol. 20(10): p. 10617 (cit. on p. 25).

[Muz12]   MUZAMMIL, A. ARAIN, C. MUELLER, and G. MUELLER: *Optical Layout and Parameters for the Advanced LIGO Cavities*. LIGO Document Control Center. T0900043. 2012 (cit. on p. 7).

[Opp17]   OPPERMANN, P.: 'Characterization and stabilization of a high power fiber amplifier laser'. PhD thesis. Gottfried Wilhelm Leibniz Universität Hannover, 2017 (cit. on pp. 1, 19, 21).

[Pla17]   PLAKITY, S.: *Aufbau und Charakterisierung einer durch Schrotrauschen limitierten Photodiode mit Ueberlastungsschutz*. Bachelor of sience thesis. Jan. 2017 (cit. on p. 55).

[Rob95]   ROBERTSON, D. I., E. MORRISON, J. HOUGH, S. KILLBOURN, B. J. MEERS, G. P. NEWTON, N. A. ROBERTSON, K. A. STRAIN, and H. WARD: 'The Glasgow 10 m prototype laser interferometric gravitational wave detector'. *Review of scientific instruments* (1995), vol. 66(9): pp. 4447–4452 (cit. on p. 1).

[Sau94]   SAULSON, P.-R.: *Fundamentals of Interferometric Gravitational Wave Detectors*. Singapore: World Scientific Publishing Co. Pte.Ltd., 1994 (cit. on p. 3).

[Sch18]   SCHREIBER, EMIL: 'Gravitational-wave detection beyond the quantum shot-noise limit: The integration of squeezed light in GEO600'. PhD thesis. Leibniz Universität Hannover, 2018 (cit. on p. 27).

[Sch16]   SCHÜTTE, DIRK: 'Modern Contol Approaches for Next Generation Interferometric Gravitational Wave Detectors'. PhD thesis. Leibniz Universität Hannover, 2016 (cit. on pp. 73, 77, 82).

[Sho88] SHOEMAKER, D., R. SCHILLING, L. SCHNUPP, W. WINKLER, K. MAIS-CHBERGER, and A. RÜDIGER: 'Noise behavior of the Garching 30 meter prototype gravitational wave detector'. *Phys. Rev. D* (2 July 1988), vol. 38: pp. 423–432 (cit. on p. 1).

[Sto09] STOCHINO, ALBERTO, BENJAMIN ABBOT, YOICHI ASO, MARK BARTON, ALESSANDRO BERTOLINI, VALERIO BOSCHI, DENNIS COYNE, RICCARDO DESALVO, CARLO GALLI, YUMEI HUANG, et al.: 'The Seismic Attenuation System (SAS) for the Advanced LIGO gravitational wave interferometric detectors'. *Nuclear Instruments and Methods in Physics Research Section A: Accelerators, Spectrometers, Detectors and Associated Equipment* (2009), vol. 598(3): pp. 737–753 (cit. on p. 11).

[Tay82] TAYLOR, J. H. and J. M. WEISBERG: 'A new test of general relativity Gravitational radiation and the binary pulsar 1913 16'. *The Astrophysical Journal* (Feb. 1982), vol. 253: p. 908 (cit. on p. 1).

[Tay09] TAYLOR, JOHN ROBERT: 'Interferometric Experiments Towards Advanced Gravitational Wave Detectors'. PhD thesis. University of Glasgow, 2009 (cit. on p. 36).

[Tor00] TORRIE, CALUM IAIN EACHAN: 'Development of suspensions for the GEO 600 gravitational wave detector'. PhD thesis. University of Glasgow, 2000 (cit. on p. 36).

[Wan18] WANG, HAOYU, MIGUEL DOVALE-ÁLVAREZ, CHRISTOPHER COLLINS, DANIEL DAVID BROWN, MENGYAO WANG, CONOR M. MOW-LOWRY, SEN HAN, and ANDREAS FREISE: 'Feasibility of near unstable cavities for future gravitational wave detectors'. *Physical Review D* (Jan. 2018), vol. 97(2) (cit. on p. 7).

[Wan12] WANNER, A., G. BERGMANN, A. BERTOLINI, T. FRICKE, H. LÜCK, C. M. MOW-LOWRY, K. A. STRAIN, S. GOSSLER, and K. DANZMANN: 'Seismic attenuation system for the AEI 10 meter Prototype'. *Classical and Quantum Gravity* (2012), vol. 29(24): p. 245007 (cit. on pp. 11, 12).

[Wan13] WANNER, ALEXANDER: 'Seismic Attenuation System for the AEI 10m Prototype'. PhD thesis. Leibniz Universität Hannover, 2013 (cit. on pp. 1, 12).

[War08] WARD, R. L., RANA ADHIKARI, B. ABBOTT, ROBERT ABBOTT, D. BARRON, ROLF BORK, T. FRICKE, V. FROLOV, J. HEEFNER, A. IVANOV, et al.: 'DC readout experiment at the Caltech 40m prototype interferometer'. *Classical and Quantum Gravity* (2008), vol. 25(11): p. 114030 (cit. on p. 1).

[Wes16] WESTPHAL, TOBIAS: 'A Coating Thermal Noise Interferometer for the AEI 10m Prototype facility'. PhD thesis. Gottfried Wilhelm Leibniz Universität Hannover, 2016 (cit. on pp. 16, 36, 39, 77).

[Win11]   WINKELMANN, L., O. PUNCKEN, R. KLUZIK, C. VELTKAMP, P. KWEE, J. POELD, C. BOGAN, B. WILLKE, M. FREDE, J. NEUMANN, P. WESSELS, and D. KRACHT: 'Injection-locked single-frequency laser with an output power of 220 W'. *Applied Physics B* (Feb. 2011), vol. 102(3): pp. 529–538 (cit. on p. 25).

[Wit15]   WITTEL, H., S. HILD, G. BERGMANN, K. DANZMANN, and K. A. STRAIN: 'New design of electrostatic mirror actuators for application in high-precision interferometry'. *Classical and Quantum Gravity* (2015), vol. 32(17): p. 175021 (cit. on pp. 7, 16).

[Zuc02]   ZUCKER, M.: *LIGO Advanced System Test Interferometer*. LIGO Document Control Center. Oct. 2002 (cit. on p. 1).

List of Figures

A Simulations

A.1 State Space Model

The state space model was used for modeling the frequency reference cavity suspensions. A simulink control loop model built around this state space model is shown in figure A.1. Transfer functions from various parts of the suspensions can be simulated with this model. The ports for simulating the longitudinal transfer functions of the suspensions are marked. The transfer function simulations done for this thesis were taken from ground motion to mirror motion (from ground long to long 3) or from top mass motion to mirror motion (long 1 to long 3).

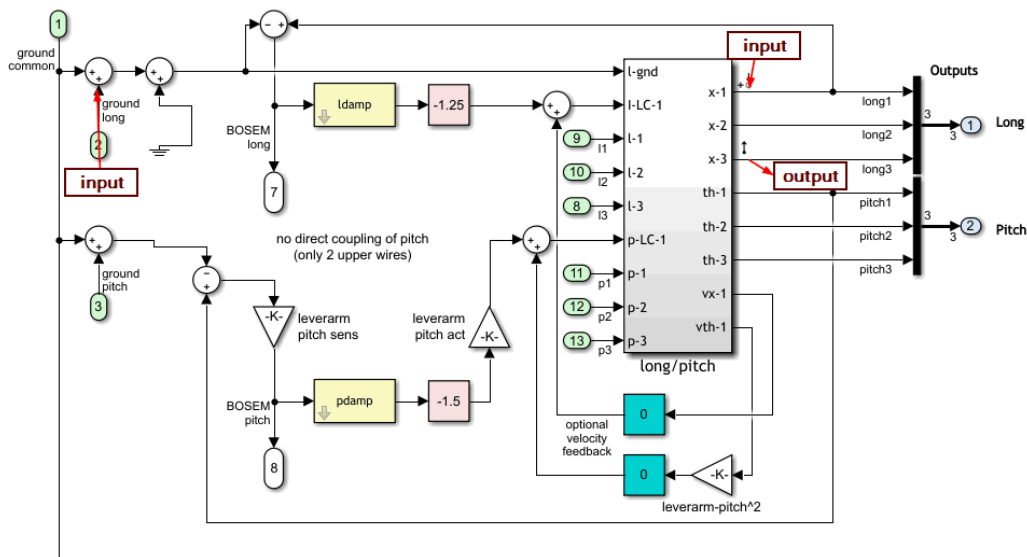Since longitudinal and pitch degrees of freedom are cross coupled they cannot be traced separately in the model.

**Figure A.1:** Excerpt from the simulink model for longitudinal and pitch.

B Electronics

B.1 PDH Locking Phototdiode

The PDH locking photodiode for the frequency reference cavity was adapted from an aLIGO photodiode. The schematics of version 1.4 are shown in B.1. These schematics are part of a documentation produced with the program Easily Applicable Graphical Layout Editor (EAGLE). Parts with undefined values are highlighted in orange. For the frequency reference cavity, a 3 mm InGaAs photodiode from Perkin Ellmer is used. All resistors in the circuit are MiniMelf.

The current limiter, consisting of the two transistors T_1 and T_2 and of the two resistors R_1 and R_2, is described in section 3.4.2.
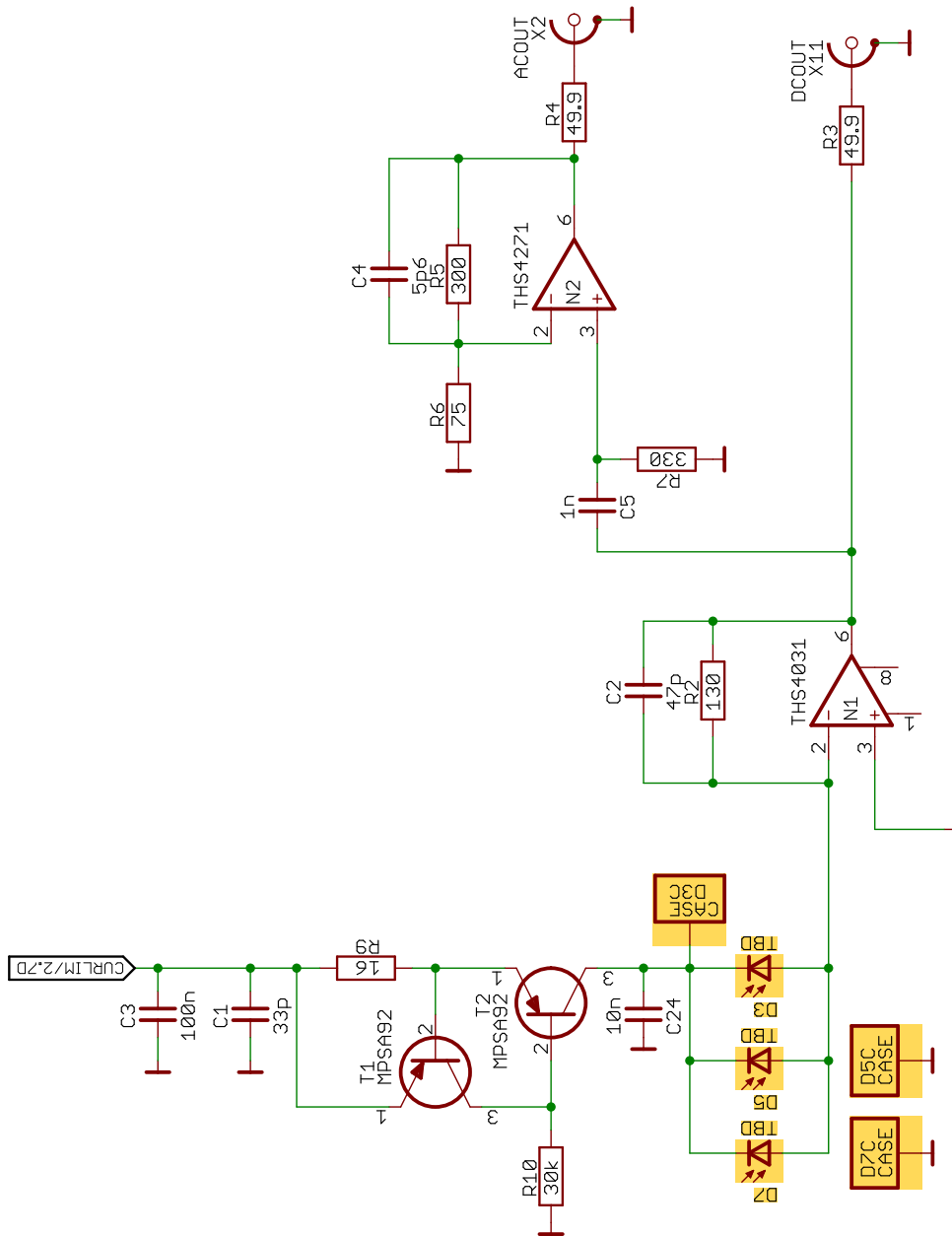
Figure B.1: Eagle schematics of the frequency reference cavity locking photodiode.

Publications

[1] J. Aasi et al.
Directed search for continuous gravitational waves from the galactic center.
Physical Review D, 88(10), nov 2013.

[2] J. Aasi et al.
Enhanced sensitivity of the LIGO gravitational wave detector by using squeezed
states of light.
Nature Photonics, 7(8):613–619, jul 2013.

[3] J. Aasi et al.
Search for long-lived gravitational-wave transients coincident with long gamma-ray
bursts.
Physical Review D, 88(12), dec 2013.

[4] M. G. Aartsen et al.
Multimessenger search for sources of gravitational waves and high-energy neutrinos:
Initial results for LIGO-virgo and IceCube.
Physical Review D, 90(10), nov 2014.

[5] J. Aasi, , et al.
Search for gravitational waves associated withγ-ray bursts detected by the interplane-
tary network.
Physical Review Letters, 113(1), jun 2014.

[6] J. Aasi et al.
Application of a hough search for continuous gravitational waves on data from the
fifth LIGO science run.
Classical and Quantum Gravity, 31(8):085014, apr 2014.

[7] J. Aasi et al.
Constraints on cosmic strings from the LIGO-virgo gravitational-wave detectors.
Physical Review Letters, 112(13), apr 2014.

[8] J. Aasi et al.
First all-sky search for continuous gravitational waves from unknown sources in
binary systems.
Physical Review D, 90(6), sep 2014.

[9] J. Aasi et al.
First searches for optical counterparts to gravitational-wave candidate events.

The Astrophysical Journal Supplement Series, 211(1):7, feb 2014.

[10] J. Aasi et al.
Gravitational waves from known pulsars: Results from the initial detector era.
The Astrophysical Journal, 785(2):119, apr 2014.

[11] J. Aasi et al.
Implementation of an F-statistic all-sky search for continuous gravitational waves in virgo VSR1 data.
Classical and Quantum Gravity, 31(16):165014, aug 2014.

[12] J. Aasi et al.
Improved upper limits on the stochastic gravitational-wave background from 2009–2010 LIGO and virgo data.
Physical Review Letters, 113(23), dec 2014.

[13] J. Aasi et al.
Methods and results of a search for gravitational waves associated with gamma-ray bursts using the GEO 600, LIGO, and virgo detectors.
Physical Review D, 89(12), jun 2014.

[14] J. Aasi et al.
The NINJA-2 project: detecting and characterizing gravitational waveforms modelled using numerical binary black hole simulations.
Classical and Quantum Gravity, 31(11):115004, may 2014.

[15] J. Aasi et al.
Search for gravitational radiation from intermediate mass black hole binaries in data from the second LIGO-virgo joint science run.
Physical Review D, 89(12), jun 2014.

[16] J. Aasi et al.
Search for gravitational radiation from intermediate mass black hole binaries in data from the second LIGO-virgo joint science run.
Physical Review D, 89(12), jun 2014.

[17] J. Aasi et al.
Search for gravitational wave ringdowns from perturbed intermediate mass black holes in LIGO-virgo data from 2005–2010.
Physical Review D, 89(10), may 2014.

[18] F. Acernese et al.
Concepts and research for future detectors.
General Relativity and Gravitation, 46(5), apr 2014.

[19] G. Hofmann, . . . , M. M. Hanke, . . . , and K. Yamamoto.
Indium joints for cryogenic gravitational wave detectors.
Classical and Quantum Gravity, 32(24):245013, dec 2015.

[20] J. Aasi et al.
Advanced LIGO.
Classical and Quantum Gravity, 32(7):074001, mar 2015.

[21] J. Aasi et al.
Characterization of the LIGO detectors during their sixth science run.
Classical and Quantum Gravity, 32(11):115012, may 2015.

[22] J. Aasi et al.
Characterization of the LIGO detectors during their sixth science run.
Classical and Quantum Gravity, 32(11):115012, may 2015.

[23] J. Aasi et al.
Directed search for gravitational waves from scorpius x-1 with initial LIGO data.
Physical Review D, 91(6), mar 2015.

[24] J. Aasi et al.
Narrow-band search of continuous gravitational-wave signals from crab and vela
pulsars in virgo VSR4 data.
Physical Review D, 91(2), jan 2015.

[25] J. Aasi et al.
Searches for continuous gravitational waves from nine young supernova remnants.
The Astrophysical Journal, 813(1):39, oct 2015.

[26] J. Aasi et al.
Searching for stochastic gravitational waves using data from the two colocated LIGO
hanford detectors.
Physical Review D, 91(2), jan 2015.

[27] J. Aasi et al.
Searching for stochastic gravitational waves using data from the two colocated LIGO
hanford detectors.
Physical Review D, 91(2), jan 2015.

[28] J. Aasi et al.
First low frequency all-sky search for continuous gravitational wave signals.
Physical Review D, 93(4), feb 2016.

[29] J. Aasi et al.
Search of the orion spur for continuous gravitational waves using a loosely coherent
algorithm on data from LIGO interferometers.
Physical Review D, 93(4), feb 2016.

[30] B. P. Abbott et al.
Astrophysical implications of the binary black hole merger gw150914.
The Astrophysical Journal, 818(2):L22, feb 2016.

[31] B. P. Abbott et al.
Characterization of transient noise in advanced LIGO relevant to gravitational wave
signal GW150914.
Classical and Quantum Gravity, 33(13):134001, jun 2016.

[32] B. P. Abbott et al.
Localization and broadband followup of the gravitational-wave transient gw150914.
The Astrophysical Journal, 826(1):L13, jul 2016.

[33] B. P. Abbott et al.
Prospects for observing and localizing gravitational-wave transients with advanced
LIGO and advanced virgo.
Living Reviews in Relativity, 19(1), feb 2016.

[34] B. P. Abbott et al.
Supplement: "localization and broadband follow-up of the gravitational-wave tran-
sient gw150914".
The Astrophysical Journal Supplement Series, 225(1):8, jul 2016.

[35] B. P. Abbott et al.
The rate of binary black hole mergers inferred from advanced ligo observations
surrounding gw150914.
The Astrophysical Journal, 833(1):L1, nov 2016.

[36] B. P. Abbott et al.
Upper limits on the rates of binary neutron star and neutron star black hole mergers
from advanced ligo's first observing run.
The Astrophysical Journal, 832(2):L21, nov 2016.

[37] B. P. Abbott et al.
All-sky search for long-duration gravitational wave transients with initial LIGO.
Physical Review D, 93(4), feb 2016.

[38] B. P. Abbott et al.
Binary black hole mergers in the first advanced LIGO observing run.
Physical Review X, 6(4), oct 2016.

[39] B. P. Abbott et al.
Comprehensive all-sky search for periodic gravitational waves in the sixth science
run LIGO data.
Physical Review D, 94(4), aug 2016.

[40] B. P. Abbott et al.
Directly comparing GW150914 with numerical solutions of einstein's equations for
binary black hole coalescence.
Physical Review D, 94(6), sep 2016.

[41] B. P. Abbott et al.
First targeted search for gravitational-wave bursts from core-collapse supernovae in
data of first-generation laser interferometer detectors.
Physical Review D, 94(10), nov 2016.

[42] B. P. Abbott et al.
GW150914: First results from the search for binary black hole coalescence with
advanced LIGO.
Physical Review D, 93(12), jun 2016.

[43] B. P. Abbott et al.
GW150914: Implications for the stochastic gravitational-wave background from
binary black holes.
Physical Review Letters, 116(13), mar 2016.

[44] B. P. Abbott et al.
GW150914: The advanced LIGO detectors in the era of first discoveries.
Physical Review Letters, 116(13), mar 2016.

[45] B. P. Abbott et al.
GW151226: Observation of gravitational waves from a 22-solar-mass binary black
hole coalescence.
Physical Review Letters, 116(24), jun 2016.

[46] B. P. Abbott et al.
GW151226: Observation of gravitational waves from a 22-solar-mass binary black
hole coalescence.
Physical Review Letters, 116(24), jun 2016.

[47] B. P. Abbott et al.
Improved analysis of GW150914 using a fully spin-precessing waveform model.
Physical Review X, 6(4), oct 2016.

[48] B. P. Abbott et al.
Observation of gravitational waves from a binary black hole merger.
Physical Review Letters, 116(6), feb 2016.

[49] B. P. Abbott et al.
Observing gravitational-wave transient GW150914 with minimal assumptions.
Physical Review D, 93(12), jun 2016.

[50] B. P. Abbott et al.
Properties of the binary black hole merger GW150914.
Physical Review Letters, 116(24), jun 2016.

[51] B. P. Abbott et al.
Results of the deepest all-sky survey for continuous gravitational waves on LIGO s6
data running on the einstein@home volunteer distributed computing project.

Physical Review D, 94(10), nov 2016.

[52] B. P. Abbott et al.
Search for transient gravitational waves in coincidence with short-duration radio
    transients during 2007–2013.
Physical Review D, 93(12), jun 2016.

[53] B. P. Abbott et al.
Tests of general relativity with GW150914.
Physical Review Letters, 116(22), may 2016.

[54] S. Adrián-Martínez, , et al.
High-energy neutrino follow-up search of gravitational wave event GW150914 with
    ANTARES and IceCube.
Physical Review D, 93(12), jun 2016.

[55] and B. P. Abbott et al.
The basic physics of the binary black hole merger GW150914.
Annalen der Physik, 529(1-2):1600209, oct 2016.

[56] G. Bergmann, C. M. Mow-Lowry, V. B. Adya, A. Bertolini, M. M. Hanke, R. Kirch-
    hoff, S. M. Köhlenbeck, G. Kühn, P. Oppermann, A. Wanner
Passive-performance, analysis, and upgrades of a 1-ton seismic attenuation system.
Classical and Quantum Gravity, 34(6):065002, feb 2017.

[57] R. Kirchhoff, . . . , M. M. Hanke, . . . , K. A. Strain.
Huddle test measurement of a near johnson noise limited geophone.
Review of Scientific Instruments, 88(11):115008, nov 2017.

[58] B. P. Abbott, , et al.
Effects of waveform model systematics on the interpretation of GW150914.
Classical and Quantum Gravity, 34(10):104002, apr 2017.

[59] B. P. Abbott, , et al.
First search for gravitational waves from known pulsars with advanced LIGO.
The Astrophysical Journal, 839(1):12, apr 2017.

[60] B. P. Abbott et al.
Erratum: "first search for gravitational waves from known pulsars with advanced
    LIGO" (2017, ApJ, 839, 12).
The Astrophysical Journal, 851(1):71, dec 2017.

[61] B. P. Abbott et al.
Estimating the contribution of dynamical ejecta in the kilonova associated with
    GW170817.
The Astrophysical Journal, 850(2):L39, dec 2017.

[62] B. P. Abbott et al.

Exploring the sensitivity of next generation gravitational wave detectors.
Classical and Quantum Gravity, 34(4):044001, jan 2017.

[63] B. P. Abbott et al.
A gravitational-wave standard siren measurement of the hubble constant.
Nature, oct 2017.

[64] B. P. Abbott et al.
Gravitational waves and gamma-rays from a binary neutron star merger: GW170817 and GRB 170817a.
The Astrophysical Journal, 848(2):L13, oct 2017.

[65] B. P. Abbott et al.
Gravitational waves and gamma-rays from a binary neutron star merger: GW170817 and GRB 170817a.
The Astrophysical Journal, 848(2):L13, oct 2017.

[66] B. P. Abbott et al.
GW170608: Observation of a 19 solar-mass binary black hole coalescence.
The Astrophysical Journal, 851(2):L35, dec 2017.

[67] B. P. Abbott et al.
Multi-messenger observations of a binary neutron star merger.
The Astrophysical Journal, 848(2):L12, oct 2017.

[68] B. P. Abbott et al.
On the progenitor of binary neutron star merger GW170817.
The Astrophysical Journal, 850(2):L40, dec 2017.

[69] B. P. Abbott et al.
Search for gravitational waves associated with gamma-ray bursts during the first advanced LIGO observing run and implications for the origin of GRB 150906b.
The Astrophysical Journal, 841(2):89, may 2017.

[70] B. P. Abbott et al.
Search for gravitational waves associated with gamma-ray bursts during the first advanced LIGO observing run and implications for the origin of GRB 150906b.
The Astrophysical Journal, 841(2):89, may 2017.

[71] B. P. Abbott et al.
Search for post-merger gravitational waves from the remnant of the binary neutron star merger GW170817.
The Astrophysical Journal, 851(1):L16, dec 2017.

[72] B. P. Abbott et al.
Upper limits on gravitational waves from scorpius x-1 from a model-based cross-correlation search in advanced LIGO data.
The Astrophysical Journal, 847(1):47, sep 2017.

[73] B. P. Abbott et al.
All-sky search for periodic gravitational waves in the o1 LIGO data.
Physical Review D, 96(6), sep 2017.

[74] B. P. Abbott et al.
All-sky search for short gravitational-wave bursts in the first advanced LIGO run.
Physical Review D, 95(4), feb 2017.

[75] B. P. Abbott et al.
All-sky search for short gravitational-wave bursts in the first advanced LIGO run.
Physical Review D, 95(4), feb 2017.

[76] B. P. Abbott et al.
Directional limits on persistent gravitational waves from advanced LIGO's first observing run.
Physical Review Letters, 118(12), mar 2017.

[77] B. P. Abbott et al.
First low-frequency einstein@home all-sky search for continuous gravitational waves in advanced LIGO data.
Physical Review D, 96(12), dec 2017.

[78] B. P. Abbott et al.
First low-frequency einstein@home all-sky search for continuous gravitational waves in advanced LIGO data.
Physical Review D, 96(12), dec 2017.

[79] B. P. Abbott et al.
First narrow-band search for continuous gravitational waves from known pulsars in advanced detector data.
Physical Review D, 96(12), dec 2017.

[80] B. P. Abbott et al.
First narrow-band search for continuous gravitational waves from known pulsars in advanced detector data.
Physical Review D, 96(12), dec 2017.

[81] B. P. Abbott et al.
GW170104: Observation of a 50-solar-mass binary black hole coalescence at redshift 0.2.
Physical Review Letters, 118(22), jun 2017.

[82] B. P. Abbott et al.
GW170814: A three-detector observation of gravitational waves from a binary black hole coalescence.
Physical Review Letters, 119(14), oct 2017.

[83] B. P. Abbott et al.
GW170817: Observation of gravitational waves from a binary neutron star inspiral.
Physical Review Letters, 119(16), oct 2017.

[84] B. P. Abbott et al.
Search for continuous gravitational waves from neutron stars in globular cluster NGC 6544.
Physical Review D, 95(8), apr 2017.

[85] B. P. Abbott et al.
Search for gravitational waves from scorpius x-1 in the first advanced LIGO observing run with a hidden markov model.
Physical Review D, 95(12), jun 2017.

[86] B. P. Abbott et al.
Search for intermediate mass black hole binaries in the first observing run of advanced LIGO.
Physical Review D, 96(2), jul 2017.

[87] B. P. Abbott et al.
Upper limits on the stochastic gravitational-wave background from advanced LIGO's first observing run.
Physical Review Letters, 118(12), mar 2017.

[88] B. P. Abbott et al.
The basic physics of the binary black hole merger gw150914.
Annalen der Physik, 529(1-2), 2017.

[89] A. Albert et al.
Search for high-energy neutrinos from binary neutron star merger GW170817 with ANTARES, IceCube, and the pierre auger observatory.
The Astrophysical Journal, 850(2):L35, nov 2017.

[90] A. Albert et al.
Search for high-energy neutrinos from gravitational wave event GW151226 and candidate LVT151012 with ANTARES and IceCube.
Physical Review D, 96(2), jul 2017.

[91] A. Albert et al.
Search for high-energy neutrinos from gravitational wave event GW151226 and candidate LVT151012 with ANTARES and IceCube.
Physical Review D, 96(2), jul 2017.

[92] B. P. Abbott et al.
All-sky search for long-duration gravitational wave transients in the first advanced LIGO observing run.
Classical and Quantum Gravity, 35(6):065009, feb 2018.

[93] B. P. Abbott et al.
First search for nontensorial gravitational waves from known pulsars.
Physical Review Letters, 120(3), jan 2018.

[94] B. P. Abbott et al.
Localization and broadband follow-up of the gravitational-wave transient GW150914.
pages –, 2018.

[95] B. P. Abbott et al.
Search for Tensor, Vector, and Scalar Polarizations in the Stochastic Gravitational-
Wave Background.
Physical Review Letters, pages –, may 2018.

[96] B. P. Abbott et al.
GW170817: Implications for the Stochastic Gravitational-Wave Background from
Compact Binary Coalescences.
Physical Review Letters, pages –, feb 2018.

[97] B. P. Abbott et al.
Constraints on cosmic strings using data from the first Advanced LIGO observing
run.
Physical Review, pages –, may 2018.

[98] B. P. Abbott et al.
Full band all-sky search for periodic gravitational waves in the O1 LIGO data.
Physical Review, pages –, may 2018.

Curriculum Vitae

Personalien

Name   Manuela Melanie Hanke

Geburtsdatum/-ort   08.07.1985, Neustadt am Rübenberge, Deutschland

Berufserfahrung

02/2012 - heute   Promotion am Max-Planck-Institut für Gravitationsphysik
                      (Albert-Einstein-Institut),
                      Leibniz Universität Hannover

02/2011 - 03/2011   Wissenschaftliche Hilfskraft am Institut für Quantenoptik,
                      Leibniz Universität Hannover

06/2007 - 07/2007   Wissenschaftliche Hilfskraft am Institut für Meteorologie und Klima-
                      tologie,
                      Leibniz Universität Hannover

Auslandsaufenthalte und Praktika

11/2013 - 12/2013   Austausch im Rahmen des Elites-Programm,
                      University of Tokyo, Japan

09/2010 - 12/2010   Wissenschaftliche Hilfskraft, Universität Aarhus, Dänemark

09/2009 - 03/2010   Auslandssemester im Rahmen des Erasmus-Programs,
                      Universidad de Granada, Spanien

06/2006 - 07/2006   Praktikum am Institut für Atmosphärenphysik,
                      Kühlungsborn, Deutschland

Studium

06/2010 - 08/2011   Diplomarbeit am Institut für Quantenoptik,
                      Leibniz Universität Hannover

                      Thema der Diplomarbeit: 'Spinpräparation ultra-kalter atomarer En-
                      sembles auf einem mesoskopisichen Atomchip'.

10/2007 - heute   Leibniz Universität Hannover, Studium der Physik

10/2005 - 10/2007   Leibniz Universität Hannover, Studium der Meteorologie

Schulische Ausbildung

08/1999 - 05/2005   Johannes-Kepler-Gymnasium in Garbsen

Acknowledgments